A NUMERICAL APPROACH FOR THE SEISMIC ANALYSIS OF REINFORCED CONCRETE STRUCTURES ENVIRONMENTALLY DAMAGED AND CABLE-STRENGTHENED

A.A. Liolios [1], K.E. Chalioris [1] and K.A. Liolios [2]

[1] Democritus University of Thrace, Dept. Civil Engineering,
Division of Structural Engineering, GR-67100 Xanthi, Greece
(e-mail: aliolios@civil.duth.gr)
[2] University of Thrace, Dep. Environmental Engineering,
Lab. Ecological Mechanics and Technology, Xanthi, Greece
(e-mail: kliolios@env.duth.gr)

**Dedicated to the Memory of Prof. Panagiotis D. Panagiotopoulos, (1.1.1950-12.8.1998),
Late Professor of Aristotle-University of Thessaloniki, Greece.**

Abstract. The paper deals with a numerical analusis for the seismic response of reinforced concrete structures containing cable elements. The cable behaviour is considered as nonconvex and nonmonotone one and is described by generalized subdifferential relations including loosening, elastoplastic - fracturing etc. effects. The problem is treated incrementally by double discretization: in space by finite elements and piece-wise linearization of cable - behaviour, and in time by the Newmark method. Thus, in each time - step an incremental linear complementarity problem is solved with a reduced number of problem unknowns. Finally, an example from civil engineering praxis is presented and some results are discussed.

Keywords: Solid Mechanics, Dynamic Unilateral Problems, Cable-braced Structures, optimization algorithmes.

1. Introduction

Braces play an important role for the strengthening, repair and earthquake resistant design and construction, see e.g. [1],[2]. This holds especially for reinforced concrete structures, exposed to environmental actions and requiring a strengthening procedure to continue to be serviceable. So, the seismic analysis of braced-structures, such as framing systems, suspended roofs and bridges, offshore platforms and braced towers, is an active investigation field [3],[4],[5].
A special class of braced structures are those containing cable elements. The peculiarity is that these elements can transmit tensile stresses only. The so-caused nonnegativity inequality for cable stresses is the principal condition in the relevant mathematical formulation of the problem. This is nonlinear, not only because of the presence of stress

inequalities, but also because the considered cable stress-strain law is nonlinear, non-convex and non-monotone.
Thus, the formulated theory is a large displacement inequality theory, as usual in cable-structures, see e.g. Panagiotopoulos [3], [6] . A compact mathematical treatment of the static problem of cable-structures has been also presented by Panagiotopoulos [3], [7], on the basis of the variational or hemivariational inequality approach. As well known, the hemivariational inequality concept has been introduced into Mechanics and Applied Mathematics by P.D. Panagiotopoulos for first time in 1983, see [8], and constitutes now the basis of the so-called Non-Smooth Mechanics.
Further, as concerns numerical aspects, a remarkable approach to the above inequality problem has been obtained by piece-wise linearization of the cable constitutive laws and by using mathematical programming [3], [4], [5], [12].
The aim of this paper is to present a numerical analysis to the seismic problem of cable braced reinforced concrete structures. For this purpose we use a double discretization. First the problem is discretized in space by the finite element method and by piece-wise linearization of the constitutive laws of cable-elements. Then, due to large cable deformations, the problem is given an incremental formulation. Further, a time discretization is applied by using the Newmark method. In each time-step an incremental non-convex linear complementarity problem, with reduced number of unknowns, is formulated and solved. Finally, the developed numerical procedure is applied to a practical Civil Engineering example.

2. Problem formulation

The structural system is discretized in space by using finite elements of the "natural" type, see e.g. [3],[6],[14]. Pin-jointed bar elements are used for the cables. The behaviour of these elements includes loosening, elastoplastic or/and elastoplastic-softening-fracturing and unloading - reloading effects. All these characteristics can be expressed mathematically by the relation:

$$s_i\ (d_i)\ \in\ \hat{\partial}\, S_i(d_i)\,. \tag{1}$$

where si and di are the (tensile force) and the deformation (elongation), respectively, of the i-th cable element, $\hat{\partial}$ is the generalized gradient and Si is the superpotential function, see Panagiotopoulos [7], [8]. By definition, relation (1) is equivalent to the following hemivariational inequality expressing the Virtual Work Principle:

$$S_i^{\uparrow}\ (d_i, e_i - d_i)\ \geq\ s_i(d_i)\ \cdot\ (e_i - d_i)\,. \tag{2}$$

where $S_i^{\uparrow}$ denotes the subderivative of S_i and e_i, d_i are kinematically admissible (virtual) deformations.
From the mathematical point of view, using (l) and (2), we can formulate the problem as a hemivariational inequality one by following [7] and investigate it. Instead of this, and because here we are interested for the computational treatment of the problem, we proceed directly by piece wise linearizing the constitutive relations (l). So, in a way similar to that in elastoplasticity –see e.g. Maier [5],[6] - and in unilateral elastodynamics –see e.g. Liolios

[9]-, we have the following constitutive relations (in matrix notation, underlined symbols) for the cable elements:

$$\underline{\psi} = \underline{B}^T \underline{\sigma} - \underline{A}\underline{\upsilon} - \underline{r}, \quad (\underline{r} \geq \underline{0}) . \tag{3}$$

$$\underline{\psi} \leq \underline{0}, \qquad \underline{\upsilon} \geq \underline{0}, \qquad \underline{\psi}^T \underline{\upsilon} = \underline{0} . \tag{4a,b,c}$$

Here $\underline{\sigma}$ is the stress vector of the whole structural system; $\underline{B}$ is a transformation matrix; $\underline{A}$ is the current symmetric interaction matrix; and $\underline{\psi}$, $(-\underline{\upsilon})$, $\underline{r}$ are the yield, slackness and ultimate capacity (resistance), respectively, vectors of cable elements.
The remaining constitutive relations for the unassembled structural system are:

$$\underline{e} = \underline{\varepsilon} + \underline{B}\underline{\upsilon} + \underline{\theta} . \tag{5}$$

$$\underline{\sigma} = \underline{E}\,\underline{\varepsilon} \quad \text{or} \quad \underline{\varepsilon} = \underline{E}^{-1}\,\underline{\sigma} . \tag{6}$$

where $\underline{e}$, $\underline{\varepsilon}$, $\underline{\theta}$ are the total, pure elastic and imposed (e.g. thermal or dislocations) strain vectors, respectively, and $\underline{E}$ is the current elasticity matrix, symmetric and positive definite.
Next, dynamic equilibrium and compatibility for the assembled structural system are expressed, respectively, by the relations

$$\underline{G}\,\underline{\sigma} + \underline{K}_G\,\underline{u} = \underline{p} - \underline{C}\dot{\underline{u}} - \underline{M}\ddot{\underline{u}} . \tag{7}$$

$$\underline{e} = \underline{G}^T\,\underline{u} . \tag{8}$$

Here $\underline{G}$ is the equilibrium matrix and $\underline{G}^T$, its transposed, is the compatibility matrix; $\underline{u}$ and $\underline{p}$ are the displacement and the load vectors, respectively; $\underline{C}$ and $\underline{M}$ are the damping and mass matrices, respectively, both symmetric and in general positive (semi)- definite. The geometric stiffness matrix $\underline{K}_G$ depends linearly on preexisting constant load [6]. Through the term $\underline{K}_G\underline{u}$ alone the geometry changes affect the equilibriumn (second order geometric effects). As usua1, dots over symbols denote derivatives with respect to time. On the other hand, for the case of seismic excitation, it is

$$\underline{p} = -\underline{M}\,\ddot{\underline{x}}_g . \tag{9}$$

where $\underline{x}_g(t)$ is the ground seismic displacement.
Finally, the initial conditions are

$$\underline{u}(t=0) = \underline{u}_o , \qquad \dot{\underline{u}}(t=0) = \dot{\underline{u}}_o , \quad \underline{\upsilon}(t=0) = \underline{\upsilon}_o . \tag{10a,b,c}$$

where $\underline{u}_o$, $\dot{\underline{u}}_o$ and $\underline{\upsilon}_o$ are known quantities.
Thus the problem consists in finding the response set $\{\underline{\sigma}(t), \underline{u}(t), \underline{\varepsilon}(t); \underline{\psi}(t), \underline{\upsilon}(t)\}$ which satisfies (3)-(10) for the given excitation set $\{\underline{p}(t)$, -or $\underline{x}_g(t)$-, $\underline{\theta}(t), \underline{u}_o, \dot{\underline{u}}_o, \underline{\upsilon}_o\}$.

3. The Incremental Linear Complementarity Approach

Due to nonmonotone and nonconvex cable behaviour (large deformations, loosening, elastoplastic-softening-fracturing effects, unloading-reloading etc.), $\underline{E}$ and $\underline{A}$ depend on $\underline{u}$ and $\underline{\upsilon}$, respectively. Therefore, an incremental formulation for the problem is more suitable. For this purpose, let $\underline{E}_t$, $\underline{A}_t$, $\underline{\psi}(t)$, $\underline{\upsilon}(t)$ etc. denote known quantities at the time t and let Δt be the time increment. Then the linear complementarity conditions (4) at the next time-moment $(t + \Delta t)$ are written as follows:

$$\underline{\psi}_t + \Delta\underline{\psi} \le \underline{0}\,, \qquad \underline{\upsilon}_t + \Delta\underline{\upsilon} \ge \underline{0}\,, \qquad (\underline{\psi}_t + \Delta\underline{\psi})^T \cdot (\underline{\upsilon}_t + \Delta\underline{\upsilon}) = 0\,. \quad (11a,b,c)$$

Next, the remaining problem conditions (3), (5)-(8) take the incremental form

$$\Delta\underline{\psi} = \underline{B}^T\Delta\underline{\sigma} - \underline{A}_t\Delta\underline{\upsilon}\,. \tag{12}$$

$$\Delta\underline{e} = \Delta\underline{\varepsilon} + \underline{B}\Delta\underline{\upsilon} - \Delta\underline{\theta}\,. \tag{13}$$

$$\Delta\underline{\sigma} = \underline{E}_t\,\Delta\underline{\varepsilon} \quad \text{or} \quad \Delta\underline{\varepsilon} = \underline{E}_t^{-1}\,\Delta\underline{\sigma}\,. \tag{14}$$

$$\Delta\underline{\sigma} + \underline{K}_G\,\Delta\underline{u} = \Delta\underline{p} - \underline{C}\,\Delta\dot{\underline{u}} - \underline{M}\,\Delta\ddot{\underline{u}}\,. \tag{15}$$

$$\Delta\underline{e} = \underline{G}^T\,\Delta\underline{u}\,. \tag{16}$$

Further, we use a time discretization scheme for the step-by-step solution of problem (11)-(l6). As known - see e.g. [10], for implicit time integration methods, relations of the following form hold:

$$\Delta\ddot{\underline{u}} = c_1\Delta\underline{u} + \underline{a}\,. \tag{17a}$$

$$\Delta\dot{\underline{u}} = c_2\Delta\underline{u} + \underline{b}\,. \tag{17b}$$

where c_1 and c_2 are positive constants in terms of Δt, and $\underline{a}$, $\underline{b}$ known quantities from previous time-steps. So, for the constant-average acceleration method, which is chosen here from the Newmark time-integration schemes, we have

$$c_1 = \frac{4}{\Delta t^2}, \qquad c_2 = \frac{2}{\Delta t}\,. \tag{17c,d}$$

In order to reduce the unknowns number, we substitute (l7) into (l5) and eliminate $\Delta\underline{\sigma}$, $\Delta\underline{\varepsilon}$, $\Delta\underline{e}$, $\Delta\underline{u}$ from (l2)-(l6). So we eventually arrive at

$$\Delta\underline{\psi} = \underline{\Lambda}\,\Delta\underline{\upsilon} + \underline{\lambda}\,. \tag{18}$$

where

$$\underline{\Lambda} = \underline{H}^T\,\underline{K}^{-1}\,\underline{H} - \underline{A} - \underline{B}^T\,\underline{E}\,\underline{B}\,. \tag{19a}$$

$$\underline{H} = \underline{G}\,\underline{E}\,\underline{B}\,. \tag{19b}$$

$$\underline{K} = \underline{G}\,\underline{E}\,\underline{G}^T + \underline{K}_G + c_2\,\underline{C} + c_1\,\underline{M}\,. \tag{19c}$$

$$\underline{\lambda} = \underline{H}^T\,\underline{K}^{-1}\,(\Delta\underline{f} + \underline{C}\,\underline{b} + \underline{M}\,\underline{a}) - \underline{B}^T\,\underline{E}\,\Delta\underline{\theta}\,. \tag{19d}$$

$$\Delta \underline{f} = \Delta \underline{p} + \underline{G}\ \underline{E}\ \Delta \underline{\theta}\,. \tag{19e}$$

Now, (18) with (11) constitute a Linear Complementarity Problem (LCP). In comparison to problem of (1)-(10), the LCP has a reduced number of unknowns. The LCP is solved in terms of the increments $\Delta \underline{\psi}$ and $\Delta \underline{\upsilon}$ by available computer codes of mathematical programming, see [5], [6], [7], [13]. Finally, by using Euler relations $\underline{u} = \underline{u}_t + \Delta \underline{u}$, $\underline{\upsilon} = \underline{\upsilon}_t + \Delta \underline{\upsilon}$ etc., we complet the solution at time $(t + \Delta t)$.

4. Numerical Example

The 6-storey framing system of reinforced concrete class C16/20 in Fig. 1, with L = 6 m and h = 4 m, was initially designed and constructed without cable-braces. The beams are of rectangular section 30/75 (width/height, in cm) for the floors i=1,2,3,4, section 25/60 for the floors i=5,6, and have a total vertical distributed load 50 kN/m (each beam). The columns have section dimensions, in cm: 35/50 for the i =1,2 floors, 30/35 for the i = 3,4 floors, and 25/30 for the i = 5,6 floors.
Due to environmental actions, corrosion and cracking has been taken place. This had caused a reduction for the section inertia moments, which is estimated [11] to be 10% for the columns and 50% for the beams. So it was necessary for the system to be strengthened. Because of architectural reasons, the cable-braces system shown in Fig. 1 has been applied, and not the usual X-braces [1]. The cable elements, of steel class S400, have a unilateral behaviour depicted in Fig. 2, with yield strain $\varepsilon_y = 0.2$ %, fracture strain $\varepsilon_f = 2$ % , yield stress $\sigma_y = 34.78$ kN/cm^2, and elasticity modulus $E_c = 200$ GPa. The branch OA is a 2-nd degree parabola with an horizontal tangent at point A.
The system is subjected to the horizontal ground seismic excitation:

$$x_g(t) = x_o\ e^{-2t}\ \sin(4\pi t)\,. \tag{20}$$

where $x_o = 0.025$ m. The graphic representation of $x_g(t)$ is shown in Fig. 3. The corresponding maximum seismic ground acceleration is 0.32 g, where g = 9.81 m/sec^2 is the gravity acceleration.
Further, for comparison reasons, we introduce the comparison coefficients

$$c = \frac{Q_c}{Q_f}\,. \tag{21}$$

where Q is the absolutely maximum value which takes a response quantity during the seismic excitation. Index (c) is for the cable-braced system and index (f) for the free (i.e. without cables) system.
Some representative results, obtained by applying the numerical method developed in previous sections, are shown in Table 1. Two cases of cross-sectional area of cables are considered: a) $F_c = 3.8$ cm^2, b) $F_c = 7.4$ cm^2. These results concern on the one hand the comparison coefficients c_s for the floor shear forces and c_d for the floor horizontal displacements, and on the other hand the stress s_i [kN/cm^2] and the percentage [%] permanent plastic deformation d_i for the i-th cable element (i = 1,...,6).

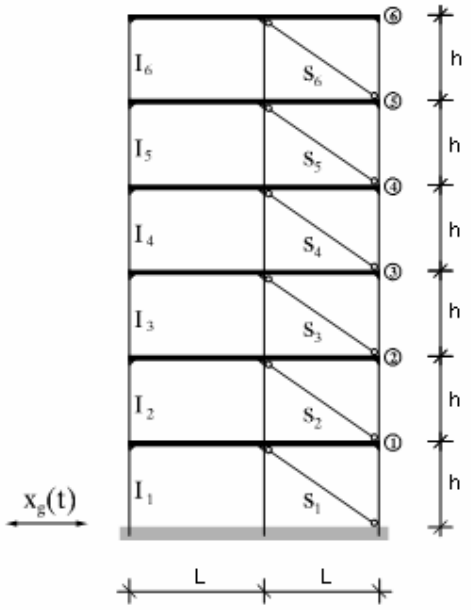

Figure 1: Numerical example: The cable-braced 6-storey structural system

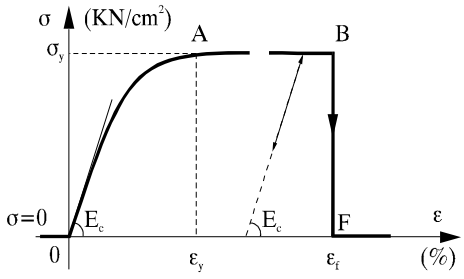

Figure 2: Cable-elements constitutive law

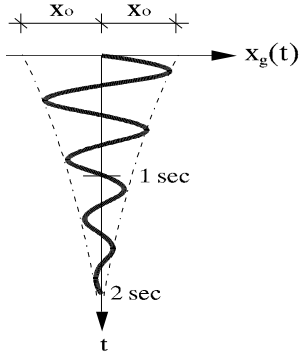

Figure 3: Seismic horizontal ground displacement

Table 1. Some results for the numerical example.

Floor		Comparison coefficients		Cable-Element	
		c_s (Shear Force)	c_d (Displ. Horiz.)	max s_i [kN/cm^2]	d_i [%]
(0)		(1)	(2)	(3)	(4)
1	a	0.921	1.001	17.84	0.128
	b	0.884	1.007	17.38	0.107
2	a	0.984	0.963	12.37	0.078
	b	0.981	0.945	12.24	0.068
3	a	0.971	1.004	19.63	0.147
	b	0.948	1.011	18.01	0.118
4	a	0.971	0.968	15.63	0.108
	b	0.982	1.103	15.07	0.091
5	a	1.123	1.171	18.17	0.137
	b	1.237	1.378	17.88	0.118
6	a	0.848	1.357	34.78	0.374
	b	0.837	1.617	34.78	0.238

As the table values of columns (1) and (2) show, the most influenced floors due to cable behaviour are the two higher ones. So, in the 5th floor the shear floor force increases about 24 % and the displacement about 38 % for case b) with $F_c = 7.4$ cm^2. In the 6th floor it is appeared a decrease about 15 % for the shear force and an increase about 62 % for the displacement. These results can be explained by energy considerations on the basis of the values on columns (3) and (4). Indeed, the cable in the 6th floor has been plastified. Therefore the seismic energy absorbed by it until plastification has returned partially to the frame system.

Such effects can be of impact type when cable-elements are fractured, and so the change of response values for the frame can be ocurred in a sudden and pounding way. Moreover, the 6th floor is influenced by the unilateral behaviour of the 6th cable alone. On the contrary, each of the lower floor beams is affected by the combined action of two cables at the same time, and so it is subjected to actions similar to those caused by X-braces. The latter have merely a bilateral character instead of a purely unilateral one. As regards the response of the lower floors, we remark from the table values that as long as the cable remain in the elastic or the early elastoplastic range of their behaviour, i.e. without fracturing, the braced structure appears a reduced response in comparison to that one of the free structure. This fact concerns especially the shear forces in the floors 1÷4, where the corresponding coefficients are about 0.90.

5. Concluding remarks

An incremental approach has been herein presented, by which the unilateral dynamic problem of the seismic analysis of cable-braced reinforced concrete structures can be treated numerically. This approach takes into account the unilateral behaviour of cable elements and leads to a linear complementarity problem, in each time increment, with a reduced number of problem unknowns.
The numerical realization is obtained by available computer codes of the finite element method, of step-by-step time integration schemes and of mathematical programming (optimization) algorithmes. Moreover, as it has been verified in an example, the herein developed approach can treat in a realistic way the seismic problem of cable-braced reinforced concrete structures in civil engineering praxis.Paper could be divided into sections and subsections.

References

[1] Chopra, A.K.: *Dynamics of Structures: Theory and Applications to Earthquake Engineering,* Pearson Prentice Hall, New York, (2007).
[2] Newmark, N.M. & E. Rosenblueth.: *Fundamentals of Earthquake Engineering.* PrenticeHall,Inc, Englewood Cliffs, N.J., (1971).
[3] Panagiotopoulos, P.D.: *Stress-Unilateral analysis of discretized cable and membrane structure in the presence of large displacements.* Ingenieur-Archiv, vol. 44, 291-300, (1975).
[4] Maier, G. & R. Contro.: *Energy approach to inelastic cable-structure analysis.* J. Enging Mech. Div., Proc. ASCE, Vol. 101, EM5, 531-547, (1975).
[5] Contro, R. & Maier, G. & A. Zavelani.: *Inelastic analysis of suspension structures by nonlinear programming.* Computer Meth. Appl. Mech. Enging, 5, l27-l43, (1975).
[6] Maier, G.: *Incremental plastic analysis in the presence of large displacements and physical instabilizing effects.* Int. J. Solids Struct. 7, 345–372 (1971).
[7] Panagiotopoulos, P.D.: *Hemivariational Inequalities. Applications in Mechanics and Engineering.* Springer-Verlag, Berlin, New York, (1993).
[8] Panagiotopoulos, P.D.: *Non-convex Energy Functions. Hemivariational Inequalities and Substationarity principles.* Acta Mechanica, 48, 111-130, (1983).
[9] Liolios, A.A.: *A Linear Complementarity Approach for the Non-convex Seismic Frictional Interaction between Adjacent Structures under Instabilizing Effects.* Journal of Global Optimization, vol. 17, no. 1-4, pp. 259-266, (2000).
[10] Weaver, W.Jr. & P.R. Johnston.: *Structural dynamics by finite elements*. Prentice Hall, Inc, Englewood Cliffs, N.J. (1987).
[11] Pauley T. and Priestley, M.J.N.: *Seismic design of reinforced concrete and masonry buildings*. Wiley, New York, (1992).
[12] Nitsiotas, G. (1971). *Die Berechnung statisch unbestimmter Tragwerke mit einseitigen Bindungen,* Ingenieur-Archiv, vol. 41, S. 46-60.
[13] Maier, G., 1973. *Mathematical programming methods in structural analysis*. In:Brebbia, C. & H. Tottenham (eds.), *Variational methods in engineering, Proc. Int. Conf. Southampton University Press, Southampton,* Vol. **2**, 8/1-8/32.
[14] Zienkiewicz, O.C. & R.L. Taylor, 1989. *The finite element method*, 4th edition. Mc GrawHill, New York-London .

STRUCTURAL INTEGRITY AND LIFE WITH STEREOMETRIC MACHINE VISION

Jasmina Lozanović Šajić[1]
[1] Faculty of Mechanical Engineering, Innovation Center
The University of Belgrade, Kraljice Marije 16, 11120 Belgrade 35
e-mail: jlozanovic@mas.bg.ac.rs

Abstract. This paper presents a mobile system that is used to prevent failure of structures. Beginning of the research involved a review of technical measurement system with two cameras – stereometric measurement and machine vision. Fracture mechanics is theoretical number of possible solutions of problems of cracks development approach for assessing structural integrity. There are numerous examples where the rating integrity is used very successfully, but there are still opportunities for new methods of achieving greater efficiency and further cost reduction engineering construction and service.

1. Introduction

Machine Vision systems are systems for video processing in industrial conditions where the most common use of these system for product quality control, automatic control of robotic systems, determining the number of people in place frequented, to monitor object in systems for monitoring traffic in biomedical engineering, while in this paper an stereometric system used within an expert system for structural integrity assessment. The term Machine Vision among other things, we mean digitization, analysis and various ways of handling the image (video) which is covered by concept of processing image.

Figure 1. Video cameras "Aramis" with the tested sample at the centre [1]

There are two functionally different methods used for automated control area, this puts an emphasis on surface recording, it will result in this paper used recording surface cracks using stereometric methods:

1. Error detection of uniform structure surface (scratches, marks, holes, etc.)
2. Error detection in the copies preserved in relation to a reference model

Namely, recording with two video cameras were evaluated as suitable contactless method, to obtain information about behavior of the structures during operations. The surface components can spray a contrasting color (black or white background), which are discretized by computer program such as a fingerprint in a unique discretized record of surface. When the construction is loaded, a displacement of points, are saved. This method helps to better understand material and component behavior and is ideally suited to monitor experiments with high temporal and local resolution. This is a non-contact and material independent measuring system providing, for static or dynamically loaded test objects, accurate: 3D surface coordinates, displacements and velocities,
Surface strain values (major and minor strain, thickness reduction), Strain rates
This is the ideal solution for: Determination of material properties (R- and N-values, FLC, Young's Modulus, etc...), Component analysis (crash tests, vibration analysis, durability studies, etc...), Verification of Finite Element Analysis. It is ideally suited to measure, with high temporal and local resolution as well as with a high accuracy, three-dimensional deformation and strain in real components and material specimens. For static or dynamically loaded specimens and components, ARAMIS allows for non-contact and material independent determination of 3D coordinates and 3D displacements, 3D speeds and accelerations, Plane strain tensor and plane strain rate, Material characteristics.

By this method is possible to obtain a complete picture of deformation of structural components by the real time with the change of the spatial components of deformations(x, y, z). Coordinates of selected points of the network are changing due shifting these points, caused by increasing load. , monitoring of coordinates is possible by using a complex mathematical apparatus, which contains expressions to determine the strain components, and expressions that are used for assessing structural integrity.

The aim was stereometric measurement applications application in the analysis if structures under the influence of external loads. Fracture mechanics is theoretical number of possible solutions of problems of crack development approach for assessing structural integrity.

There are numerous examples where integrity assessment is used very successfully, but there are still possibilities of new method to achieve greater efficiency and further cost reduction engineering, construction and service construction. A special problem is the structure composed of several different materials. Basis for stereometric measuring are two examples of transient crack and an example of surface cracks in tubes for fracture mechanics testing.

2. Setting up the experiment and development of numerical models

In the thesis [2] made the following test tubes:

- experimental (in laboratory for mechanical testing)
- stereometric measurements (monitor the deformation in real time during mechanical load)
- numeric (using licensed software for calculation of FEM), and
- analytical (FAD and CDF diagrams)

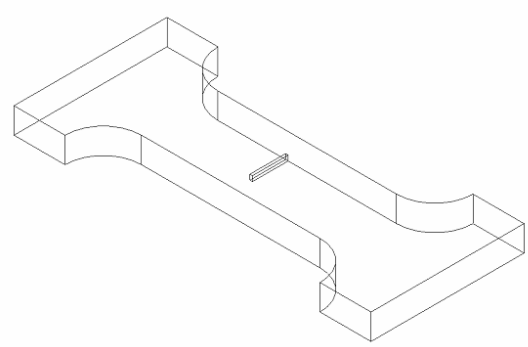

Figure 2. Model for numerical analysis.

In Figure 3, the data of distribution of equivalent von Mises's stress obtained for model with crack and fine mesh finite elements. The results obtained are preliminary, because the tensile properties of materials that make up circuit modeled using a simplidied bilinear strength curves.

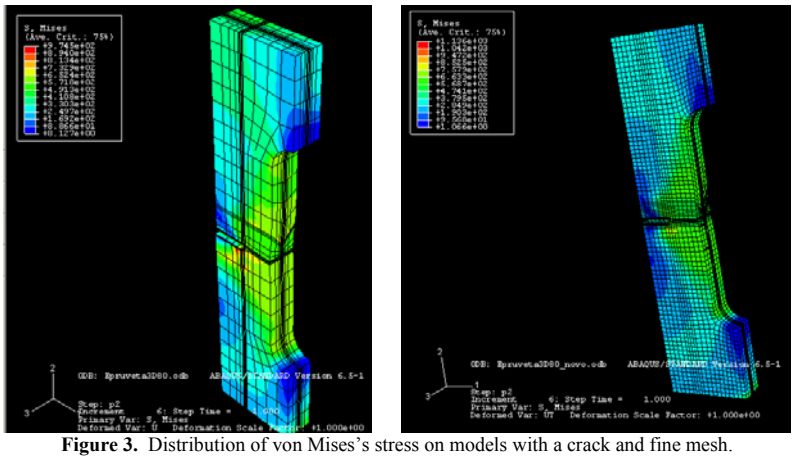

Figure 3. Distribution of von Mises's stress on models with a crack and fine mesh.

3. Results obtained by stereometric measurement

Stereometric measurement was performed on two specimens, because strength testing machine and get better results stereometric results steremetric stereometric measurement, the specimens have gone to further processing and finishing before the test.

The test were concluded welded joints of low-carbon steel increased strength X60, which is designed for longitudinally welded pipes exposed to high pressure vessels. Chemical compositions and mechanical properties of X60 steel are given in Table 1 and Table 2, consequently.

Figure 3. Tensioning specimen in testing machine with controlled growth force and stereometric monitoring crack growth.

Table 1. Chemical Compositions, X60

mass. %						
C	Mn	P	S	Co	V	Nb
0.12	0.33	0.020	0.010	0.35	0.045	0.056

Table 2. Mechanical Properties, X60

$R_{p0.2}$ [MPa]	R_m [MPa]	A [%]	Z [%]	KV [J]
448	596	22.7	55.6	76

Plate specimen with initial crack in the test specimen material resistance to fracture and define standards. Initial crack the test specimen with K welded joint were conducted electro-erosion and dynamically changing load. The study was concluded on electro-mechanical testing machine, and was used stereometric method.

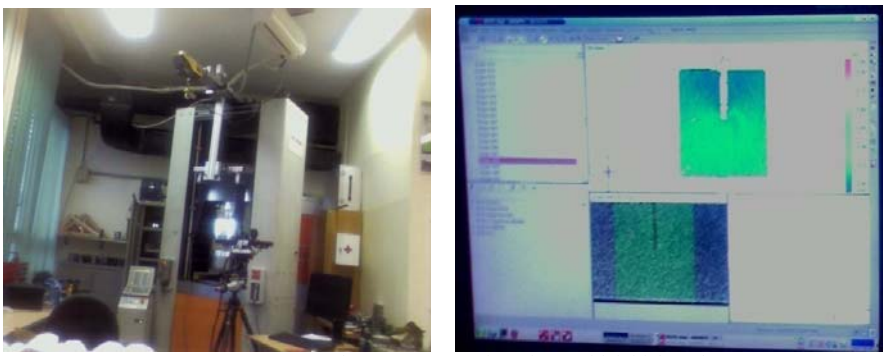

Figure 4. Stereometric measurement of specimen with initial crack.

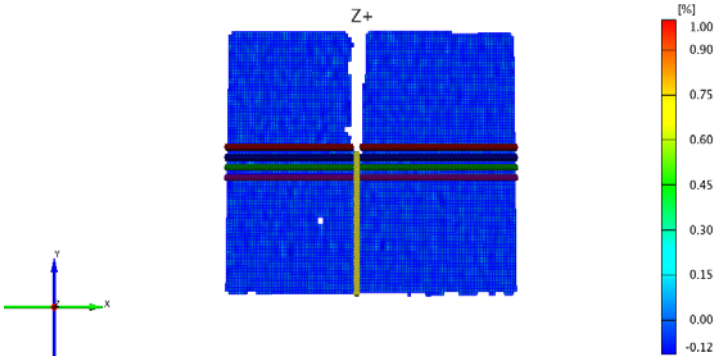

Figure 5. CMOD, obtained by software package, Aramis.

By increasing the force on the testing machine, continues stereometric measurement, and after completion of measurement is a complete picture of the state of stress and strain on tube along all three axes coordinate system, as measured on real construction provides an assessment of its integrity.

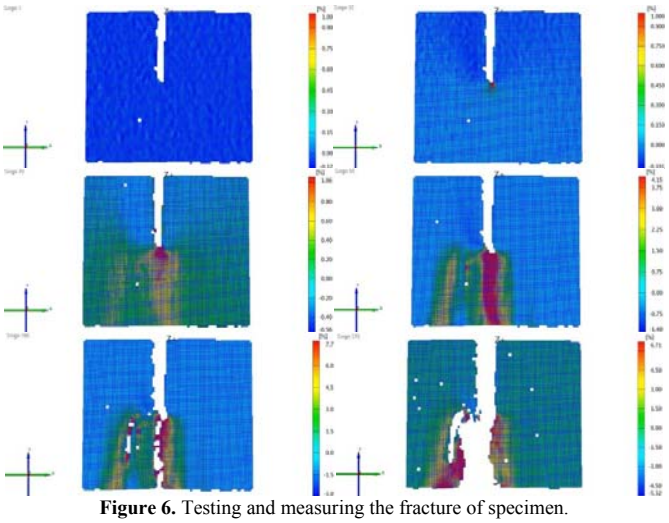

Figure 6. Testing and measuring the fracture of specimen.

Based on measurements performed stereometric, give the appropriate. Diagrams for analysis to assess the structural integrity. What is certainly be seen in Figure 6, is careful analysis of the crack can be seen in situations of internal cracks, the numerical methods not possible to accurately predict. Based on the results stereometric measurements, it is clear that there has been fracture specimen – Plastic collapse. These results were confirmed analytic on the FAD and CDF diagrams, shown in Figure 7 and Figure 8, where shows that the fracture of specimens in the zone of plastic collapse.

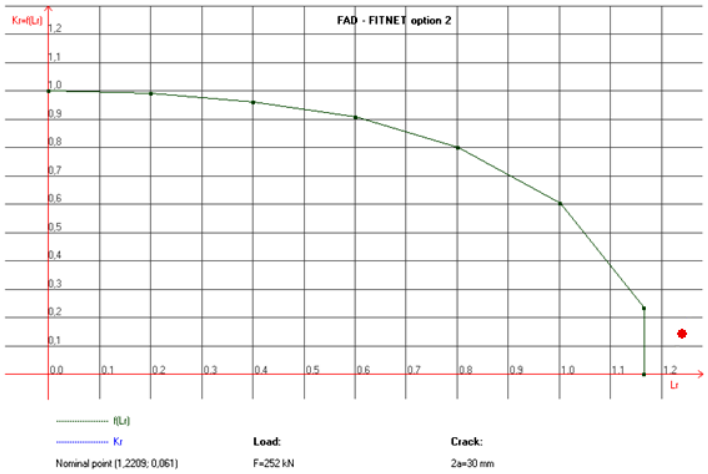

Figure 7. FAD diagram for specimen

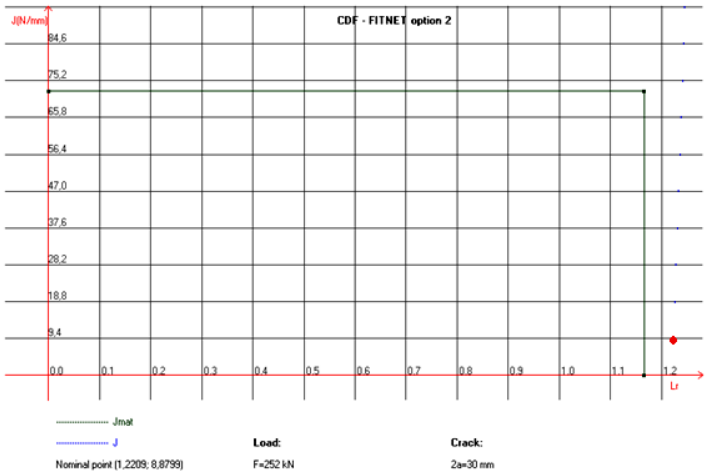

Figure 8. CDF diagram for specimen

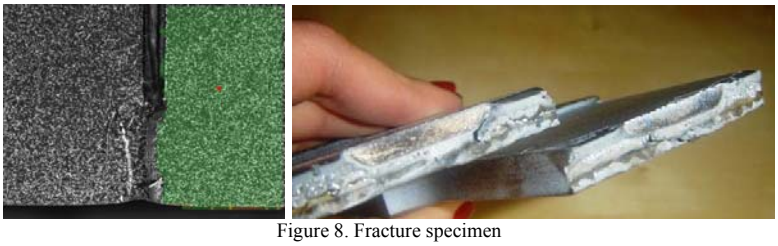

Figure 8. Fracture specimen

4. Conclusion

The research of this study showed good agreement between experimental, analytical and numerical analysis of deformation behavior of structural components with different configurations and different ways of cracking loads. Paramerers of fracture mechanics and limit load were calculated analytically and numerically, and experimentally verified aquipment measuring displacement and strain at the surface were studied components. Comparisons between analytical and numerical results on surface and corresponding experimental results have shown that it is possible to trace the behavior structural components of the cracked and assume the existence, location size and development of internal cracks.

The agreement between analytical, numerical and experimental results is good for surface cracks. Less agreement of numerical and experimental results are in internal cracks because they cannot be assumed true, the reason lies in the structure of material, as in the case welded jointsm, which are usually not taken into account in numerical modeling base material, but is taken into account in welded joints when differences in strength exceed some percentage (eg SINTAP- Structural Integrity Assessment Procedures for European Industry-is more than 10%).

Results showed that data obtained with stereometric method correspond well with numerical and analytical results which gives us justification for introducing such expert system.

References

[1] AramisGOMmbH, http://www.gom.com

[2] Јасмина Лозановић, *Аутоматизација стереометријског мерења приликом одређивања напонског стања око врха прслине и процена интегритета конструкције,* докторска дисертација, одрањена 02.06.2009., на Машинском факултету Универзитета у Београду.

[3] N. Gubeljak, J. Lozanovic, A. Sedmak, *Crack tip strain and CTOD in situ measurement,* First Serbian (26th YU) Congress on Theoretical and Applied Mechanics, Kopaonik, Serbia, April, 2007. p.p. 1103-1108.

[4] Jasmina Lozanović, Aleksandar Sedmak, Nenad Gubeljak, Measurement of Strain Using Stereometry, TEHNIČKI VJESNIK - TECHNICAL GAZETTE, Tehnički vjesnik, Vol.16. No.4 Prosinac 2009, p.p. 93-99

RESIDUAL LIFE ESTIMATION OF DAMAGED STRUCTURAL COMPONENTS USING LOW-CYCLE FATIGUE PROPERTIES

[1]Maksimovic S., [2]Vasovic I., [3]Maksimović M., [1]Đurić M.

[1] Military Technical Institute- Department of Aeronautics
Ratka Resanovica 1, Belgrade, Serbia
e-mail: s.maksimovic@open.telekom.rs
[2] Institut Goša, Milana Rakica 35, Belgrade, Serbia
e-mail: vasovic.ivana@yahoo.com
[3] Water Supply, Belgrade, Serbia
e-mail: maksimovic.mirko@gmail.com

Abstract. The goal of this paper is the establishment of computation method for the evaluation of the residual life of structural elements in the presence of initial damage which appears in the form of cracks. Therefore in this paper computation method for the evaluation of the residual life of structural elements with initial damage subjected to cyclic loading of constant amplitude load spectrum are presented. Computational methods for the evaluation of the residual life of structural elements with initial damage basically rely on crack propagation analysis. In this investigation for crack propagation analysis Strain Energy Density (SED) method will be used. This method uses the low-cycle fatigue (LCF) properties of the material, which are also being used for the lifetime evaluation until the occurrence of initial damage. Therefore experimentally obtained dynamic properties of the material such as Paris` constants are not required when this approch is concerned. The complete computation procedure for the crack propagation analysis using low-cycle fatigue material properties is illustrated with the damaged structural elements. To determine analytic expressions for stress intensity factors (SIF) singular finite elements are used. Results of numerical simulation for crack propagation based on strain density method have been compared with own experimental results.

Key words: Fatigue, residual life, damaged structural elements, aircraft attachment lugs, strain energy density method, low-cycle fatigue properties, finite elements

1. Introduction

Methods for design against fatigue failure are under constant improvement. In order to optimize constructions the designer is often forced to use the properties of the materials as efficiently as possible. One way to improve the fatigue life predictions may be to use relations between crack growth rate and the stress intensity factor range. These are fairly well established for constant amplitude loading, at least for common specimen geometries. Loading histories in engineering structures do however often exhibit varying amplitudes.
For such cases the prediction capacity is markedly lower. Ideally, the crack advance under varying amplitude should be possible to predict using experimental data from constant amplitude testing. Numerous investigations address this problem but so far without reaching any total success.
Design based on damage tolerance criteria often deals with notched components giving rise to localized stress concentrations which, in brittle materials, may generate a crack leading to catastrophic failure or to a shortening of the assessed structural life. For a successful

implementation of the damage tolerance philosophy to the design and in-service operation of structures subjected to fatigue loading it is crucial to have reliable crack growth prediction tools. Damage tolerance application to the aircraft structural components is limited to critical parts. A part, that if it fails, alone may cause the loss of an aircraft is classified as a critical part. This definition means, that aircraft wing-fuselage attachments must be comply with the damage tolerance requirements [1,2]. The main goal is a safe life design, i.e. a slow crack growth structure not requiring any insection during its full life. The Damage Tolerance approach assumes the components have a preexisting flaw from which a crack will grow under dynamic loads. This assumption makes it possible to account for in-service or manufacturing defects in determining the dynamic life. The Damage Tolerance Methodology uses fracture mechanics to predict the fatigue crack growth in a structure. In the design analysis of a slow crack growth structure it is most important to make correct estimates for the early portion of the crack growth process, because it is there the life is. In most cases this implies that maximum accuracy is needed for small corner cracks.

The ability to successfully maintain aircraft airworthiness and structural integrity is critically dependent on the application of appropriate fatigue crack growth (FCG) prediction tools. The prediction tools are required to accurately predict FCG in aircraft structures and components under flight spectrum loading, and thus reliably provide total economic lives or inspection intervals as part of a stringent aircraft structural integrity management plan.

Fatigue crack growth in aircraft structures and components under flight spectrum loading is traditionally predicted based on FCG rates obtained from constant-amplitude (CA) crack growth testing using the cycle-by-cycle approaches [14,15].

Attachment lugs are particularly critical components in crack initiation and growth because of their inherently high stress concentration levels near the lug hole. For these reasons, it is important to develop analytical/numerical as well as experimental procedures for assessing and designing damage tolerant attachment lugs to ensure the operational safety of aircraft. Over the years, several extensive studies [3-5] have been made on lug fatigue performance, involving both experimental and numerical means.

In the work of fatigue crack growth and fracture behavior of attachment lugs [6,7], an accurate calculation of the stress intensity factor is essential. Over the years several methods have evolved to compute the stress intensity factors for structural components containing cracks. These methods include analytical as well as experimental approach. The experimental backtracking approach was used to derive empirically the stress intensity factors for structural components using the growth rate data of through-the-thickness cracks for simple geometry subjected to constant-amplitude loading.

The finite element method is used to precise determine SIF`s using singular finite elements. Accurate stress-intensity factor (SIF) solutions are required to conduct thorough damage tolerance analyses of structures containing cracks. Exact closed form SIF solutions for cracks in three-dimensional solids are often lacking for complex configurations; therefore, approximate solutions must be used. Over the past two decades, considerable effort has been placed on developing computationally efficient methods which provide highly accurate SIF solutions for cracks in three-dimensional bodies.

The purpose of this investigation was to test the accuracy of the crack growth models. All necessary parameters, such as material property data, stress intensity solutions, and the load spectrum, were defined. To determine residual life of damaged structural components here

are used two crack growth methods: conventional Forman`s crack growth method and crack growth model based on the strain energy density method. The last metod uses the low cycle fatigue properties in the crack growth model.

2. Crack growth model based on Strain Energy Density Method

In this work fatigue crack growth method based on energy concept is considered and then it is necessary to determine the energy absorbed till failure. This energy can be calculated by using cyclic stress-strain curve. Function between stress and strain, as recommended by Ramberg-Osgood provides good description of elastic-plastic behavior of material, and may be expressed as:

$$\Delta\varepsilon = \frac{\Delta\sigma}{E} + 2\left(\frac{\Delta\sigma}{2k'}\right)^{\frac{1}{n'}}. \tag{2.1}$$

where E is the modulus of elasticity, $\Delta\varepsilon/2$ is strain amplitude and $\Delta\sigma/2$ is stress amplitude. Equation (2.1) enables the calculation of the stress-strain distribution by knowing low cyclic fatigue properties. As a result the energy absorbed till failure become [10,11]:

$$W_c = \frac{4}{1+n'}\sigma_f'\varepsilon_f' \tag{2.2}$$

where σ_f' is cyclic yield strength and ε_f' - fatigue ductility coefficient. Given the fact that strain energy density method is considered, the energy absorbed till failure must be determined after the energy concept is based on the following fact: The energy absorbed per unit growth of crack is equal to the plastic energy dissipated within the process zone per cycle. This energy concept is expressed by:

$$W_c\,\delta a = \omega_p, \tag{2.3}$$

where W_c is energy absorbed till failure, ω_p- the plastic energy and a - the crack length. In equation (2.3) it is necessary just to determine the plastic energy dissipated in the process zone ω_p. By integration of equation for the cyclic plastic strain energy density in the units of Joule per cycle per unit volume [10] from zero to the length of the process zone ahead of crack tip d^* it is possible to determine the plastic energy dissipated in the process zone ω_p. After integration relation of the plastic energy dissipated in the process zone becomes:

$$\omega_p = \left(\frac{1-n'}{1+n'}\right)\frac{\Delta K_I^2\,\psi}{E\,I_{n'}} \tag{2.4}$$

where ΔK_I is the range of stress intensity factor, ψ - constant depending on the strain hardening exponent n', $I_{n'}$ - the non-dimensional parameter depending on n'.
Fatigue crack growth rate can be obtained by substituting Eq. (2.2) and Eq. (2.4) in Eq. (2.3):

$$\frac{da}{dN} = \frac{(1-n')\psi}{4E\,I_{n'}\sigma_f'\,\varepsilon_f'}\left(\Delta K_I - \Delta K_{th}\right)^2, \tag{2.5}$$

where ΔK_{th} is the range of threshold stress intensity factor and is function of stress ratio i.e.

$$\Delta K_{th} = \Delta K_{th0}(1-R)^{\gamma}, \tag{2.6}$$

ΔK_{th0} is the range of threshold stress intensity factor for the stress ratio R = 0 and γ is coefficient (usually, $\gamma = 0.71$). Finally number of cycles till failure can be determined by integration of relation for fatigue crack growth rate:

$$N = B\int_{a_0}^{a_c} \frac{da}{\left(\Delta K_I - \Delta K_{th}\right)^2}, \qquad B = \frac{4\,E\,I_{n'}\,\sigma_f'\,\varepsilon_f'}{\left(1-n'\right)\psi} \tag{2.7}$$

and

$$\Delta K_I = Y\,S\,\sqrt{\pi\,a}, \tag{2.8}$$

Equation (2.7) enables us to determine crack growth life of different structural component. Very important fact is that equation (2.7) is easy for application since low cyclic material properties (n', σ_f', ε_f) available in literature are used as parameters. The only important point is stress intensity factor which, depending on the geometry complexity and the type of loading, could be determined by using analytical and/or numerical approaches.

3. Crack growth analysis using conventional approach

For crack growth analysis and fatigue life estimations have been used various conventional crack growth models. Many of these models achieve correct solutions of crack growth analyses for cracked structural elements under cyclic loads of constant amplitude. Hovever, for construction under cyclic loads of variable amplitude in form of load spectrum such as in aircraft cases it is necessary tu include the effects of shape of load spectra and its effects of estimation life of structural elements [9].

Forman, Newman and others [8] developed the equation, which is an equation often used to describe crack growth. This equation describes the crack growth curve in terms of the crack length a , the number of cycles N , the stress ratio R , the stress intensity factor range ΔK, and material constants, C, n, p, q through best fits of the da/dN - ΔK data.

$$\frac{da}{dN} = C\left[\left(\frac{1-f}{1-R}\right)\Delta K\right]^n \frac{\left(1-\dfrac{\Delta K_{th}}{\Delta K}\right)^p}{\left(1-\dfrac{K_{\max}}{K_c}\right)^q} \tag{3.1}$$

where: a - crack length, N-number of cycles, C, n, p, q – are experimentally derived material parameters , K is the stress intensity factor (SIF), K_{th} is the threshold stress intensity factor, R is the stress ratio, K_c - is the critical stress intensity factor. The Newman closure function isone of these terms and is define as f :

$$f = \frac{K_{op}}{K_{\max}} = \begin{cases} \max\left(R\ ,\ A_0 + A_1\ R + A_2\ R^2 + A_3\ R^3\right)\ ;\ R \ge 0 \\ A_0 + A_1\ R\ ;\quad -2 \le R < 0 \end{cases} \tag{3.2}$$

and the coefficients are given by:

$$A_0 = (0.825 - 34\alpha + 0.05\alpha^2)\left[\cos(\frac{\pi}{2}\frac{S_{\max}}{\sigma_0}\right]^{\frac{1}{\alpha}}$$

$$A_1 = (0.415 - 0.071\alpha)S_{msx}/\sigma_0$$

$$A_2 = 1 - A_0 - A_1 - A_3$$

$$A_3 = 2A_0 + A_1 - 1$$

where: α - is the plane stress/strain constraint factor, (σ_{max}/σ_0) is the ratio of maximum stress to the flow stress. The threshold stress intensity factor range is calculated by the following empirical equation:

$$\Delta K_{th} = \Delta K_{th0}\left(\frac{a}{a+1}\right)^{\frac{1}{2}} / \left(\frac{1-f}{(1-A_0)(1-R)}\right)^{(1+C_{th}R)} \tag{3.3}$$

Relation (3.1) represents one general crack growth models based on conventional approach. This relation can be transformed to conventional Forman`s crack growth model[5]. In region III rapid and unstable crack growth occurs, so Forman at al. Proposed equation for region III as well as for region II [9]

$$\frac{da}{dN} = \frac{C(\Delta K)^n}{(1-R)K_C - \Delta K} \tag{3.4}$$

where K_C is the fracture toughness. Forman`s equation has been developed to model of unstable crack growth domain (III).

4. Stress intensity factor solution of cracked lugs

4.1 Damaged attachment lug with initial crack through the thickness

In this section are given relations for stress intensity factor with crack through the thickness In general geometry of notched structural components and loading is too complex for the stress intensity factor (SIF) to be solved analytically. The SIF calculation is further complicated because it is a function of the position along the crack front, crack size and shape, type loading and geometry of the structure. In this work analytic and FEM were used to perform linear fracture mechanics analysis of the pin-lug assembly. Analytic results are obtained using relations derived in this paper. Good agreement between finite element and analytic results is obtained. It is very important because we can to use analytic derived expresions in crack growth analyses. Lugs are essential components of an aircraft for which proof of damage tolerance has to be undertaken. Since the literature does not contain the stress intensity solution for lugs which are required for proof of damage tolerance, the problem posed in the following investigation are: selection of a suitable method of determining othe SIF, determination of SIF as a function of crack length for various form of lug and setting up a complete formula for calculation of the SIF for lug, allowing essential parameters. The stress intensity factors are the key parameters to estimate the characteristic

of the cracked structure. Based on the stress intensity factors, fatigue crack growth and structural life predictions have been investigated. The lug dimensions are defined in Fig. 1.

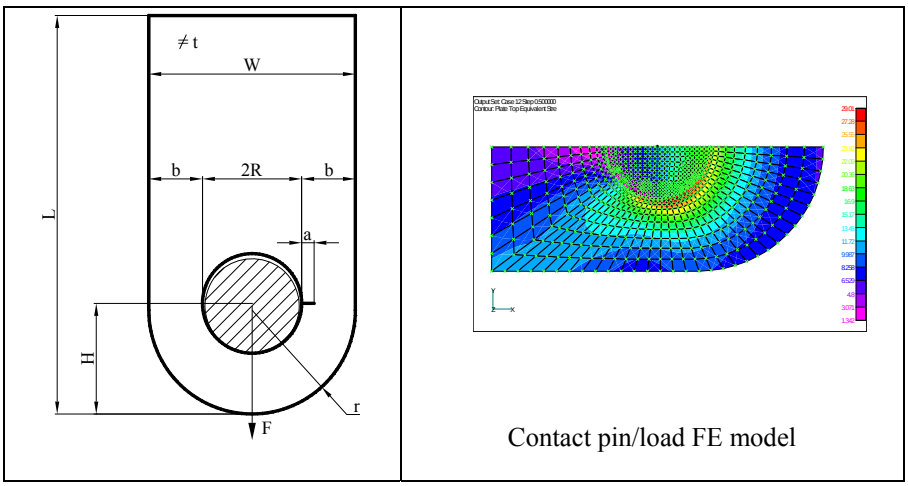

FIGURE 4.1.1: Geometry and loading of lugs with crack through the thickness

To obtain stress intensity factor for the lugs it is possible to start with general expression for the SIF in the next form

$$K = Y_{SUM}\,\sigma\sqrt{\pi a} \tag{4.1.1}$$

where: Y – correction function, a- the crack length. This function is essential in determining of the the stress intensity factor. Primary, this function depends on stress concentration factor, k_t and geometric ratio a/b. The correction function is defined using experimental and numerical investigations. This function can be defined in the next form [13]:

$$Y_{SUM} = \frac{1.12\cdot k_t \cdot A}{A+\frac{a}{b}}\cdot k \cdot Q \tag{4.2}$$

$$k = e^{r\sqrt{a/b}} \tag{4.3}$$

$$b = \frac{w-2\cdot R}{2} \tag{4.4}$$

$$r = -3.22 + 10.39\cdot\left[\frac{2\cdot R}{w}\right] - 7.67\cdot\left[\frac{2\cdot R}{w}\right]^2 \tag{4.5}$$

$$Q = \frac{U\cdot\frac{a}{b}+10^{-3}}{\frac{a}{b}+10^{-3}} \tag{4.6}$$

$$U = 0.72 + 0.52\cdot\left[\frac{2\cdot R}{H}\right] - 0.23\cdot\left[\frac{2\cdot R}{H}\right]^2 \tag{4.7}$$

$$A = 0.026 \cdot e^{1.895 \cdot \left(1+\frac{a}{b}\right)} \tag{4.8}$$

The stress concentration factor k_t is very important in calculation of correction function, eq. 4.2. In this investigation. A contact finite element stress analysis was used to analyze the load transfer between the pin and lug.

4.2 Damaged attachment Lug with semi-elliptic surface crack

Here is considered the stress intensity factors for cracked lug with the semi-elliptic surface crack as shown in Fig. 4.2.1.

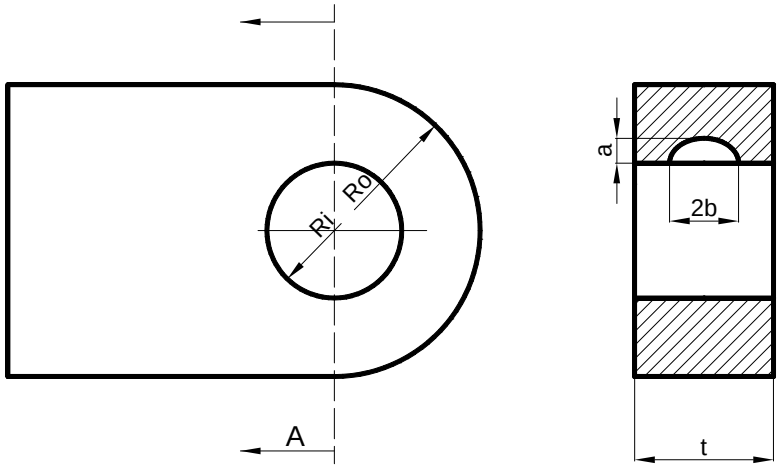

FIGURE 4.2.1 Lug with semi-elliptic surface crack

As start point for determination of stress intensity factor of attachment lug with semi-elliptic surface crack will be used Lukaš`s model [16,17]. Lukaš is considered problem of determination of SIF to plate with surface crack within zone of stress concentration. This approached is extended to the attachment lugs with semi-elliptic surface crack. By using this approach here are defined analytic expressions for determination of SIF`s at the points **A** and **B** to lug with semi-elliptic surface crack as shown in Fig. 4.2.1, in the next form:

$$K_A = F_A \sigma k_t \sqrt{\pi a} \tag{4.3.1}$$

$$F_A = F_{A,0} \sqrt{\frac{D_A}{a}} \tag{4.3.2}$$

$$F_{A,0} = \frac{1.13 + 0.09\left(\frac{a}{b}\right)}{E_2\left(\frac{a}{b}\right)}, \qquad 0 \le \frac{a}{b} \le 1 \tag{4.3.3}$$

$$D_A = a + d\left[1 - e^{\left(-\frac{a}{a'}\right)}\right] \tag{4.3.4}$$

$$a' = \frac{d}{k_t^2 - 1} \tag{4.3.5}$$

$$K_B = F_B k_t \sigma \sqrt{\pi a} \tag{4.3.6}$$

$$F_B = F_{B,0}\sqrt{\frac{D_B}{a}} \tag{4.3.7}$$

$$D_B = a + 4d\left[1 - e^{\left(-\frac{a}{4a'}\right)}\right] \tag{4.3.8}$$

$$F_{B,0} = \frac{1.243 + 0.099\left(\frac{a}{b}\right)}{E_2\left(\frac{a}{b}\right)}\sqrt{\frac{a}{b}} \tag{4.3.9}$$

Горњи аналитички изрази за ФИН код ушке са елиптичном прскотином се могу користити како за прорачун чврстоће ушки са аспекта "статичке" механике лома тако и за процену преосталог века коришћењем различитих закона ширења прскотине.

5. Numerical validation

To illustrate computation procedures in damage tolerance analysis and residual life estimations of damged structural components here are numerical examples included.

5.1 Life estimation of damaged structural elements

Subject of this analyses are cracked aircraft lugs under cyclic load of conctant amplitude end spectra. For that purpose conventional Forman crack growth model and crack growth model based on strain energy density method are used. Material of lugs is Aluminum alloy 7075 T7351 with the next material properties:

σ_m=432 N/mm^2 $\Leftrightarrow$ Tensile strength of material
σ_{02}=334 N/mm^2
K_{IC}=2225 [N/mm$^{3/2}$]

Dynamic material properties (Forman`s constants): C_F=3* 10^{-7}, n_F=2.39.
Cyclic material properties: σ_f'=613 МПа, ε_f'=0.35 , n'=0.121.

The stress intensity factors (SIF`s) of cracked lugs are determined for nominal stress levels: $\sigma_g = \sigma_{max}$=98.1 N/mm^2 and σ_{min}=9.81 N/mm^2. These stresses are determined in net cross-section of lug. The corresponding forces of lugs are defined as, $F_{max}= \sigma_g$ (w-2R) t = 63716 N and F_{min}= 6371.16 N, that are loaded of lugs. For stress analyses contact pin/lug finite element model is used. For cracked lugs defined in Table 5.1, with initial cracks a_0, SIF`s are determined using finite elements, Table 5.2. To obtain high-quality results of SIF`s cracked lugs are modeled by singular finite elements around crack tip.

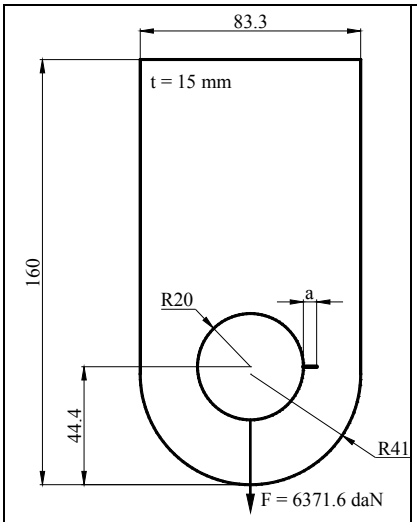

Fig 5.1: Geometry of cracked lug 2

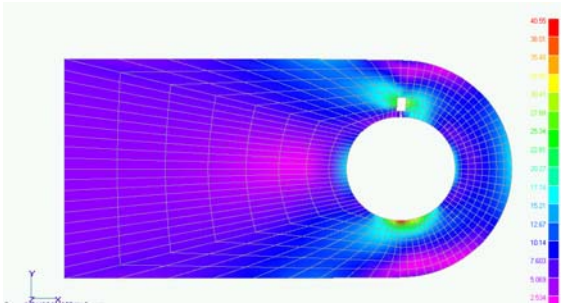

Fig. 5.2. Finite Element Model of cracked lug with stress distribution

Table 5.1: Geometric parameters of lugs [13]

Lug No.	Dimensions [mm]				
	2R	W	H	L	t
2	40	83.3	44.4	160	15
6	40	83.3	57.1	160	15
7	40	83.3	33.3	160	15

The stress intensity factors of cracked lugs are calculated under stress level: $\sigma_g = \sigma_{max}$=98.1 N/mm^2, or corresponding axial force, $F_{max}= \sigma_g$ (w-2R) t = 63716 N. In present finite element analysis of cracked lug is modeled with special singular quarter-point six-node finite elements around crack tip, Fig. 5.2. The load the model, a concentrated force, F_{max}, was applied at the center of the pin and reacted at the other and of the lug. Spring elements were used to connect the pin and lug at each pairs of nodes having identical nodal coordinates all around the periphery. The area of contact was determined iteratively by assigning a very high stiffness to spring elements which were in compression and very low stiffness (essentially zero) to spring elements which were in tension. The stress intensity factors of lugs, analytic and finite elements, for through-the-thickness cracks are shown in Table 5.2. Analytic results are obtained using relations from previous sections, eq. (4.1.1).

Table 5.2: Comparisons analytic with FEM results of SIF

Lug No.	$a\ [mm]$	$K_{I\max}^{MKE}$	$K_{I\max}^{ANAL.}$
2	5.00	68.784	65.621
6	5.33	68.124	70.246
7	4.16	94.72	93.64

From above Table 5.2 is evident good agreement between analytic and finite element results for determination of stress intensity factors. Accuracy of SIF`s is very important in precise crack growth analyses and life estimation of cracked lugs. That means that proposed analytic model for determination of SIF`s is adequate in crack growth analyses.In design process is very important to know how any geometric parameters of lug have the effects on fracture mechanics parameters. In Fig. 5.4 are shown dependence SIF, K_{max}, and height of head of lug H. In this analysis geometric properties of lugs are given in Table 5.1. From Fig. 5.4 is evident increasing of SIF`s with increasing crack length and reducing with increasing height of lug`s head.

In Fig. 5.3 are shown computation and experimental results of cracked lug No. 2 as defined in Fig. 5.1 and Table 5.1. In this computation analysis Forman crack growth model is used. Good agreement between computation and experimental results is obtained. It is evident that computation Forman`s crack growth model is to a small extent conservative for longer crack, Fig. 5.3.

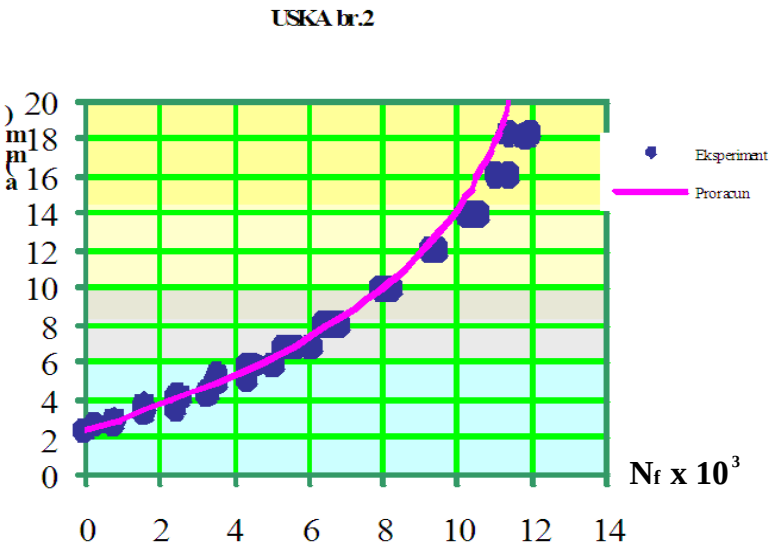

Fig. 5.3 Comparisons computational with experimental crack growth results for lug No. 2 (H=44.4 mm); k_t=2.8

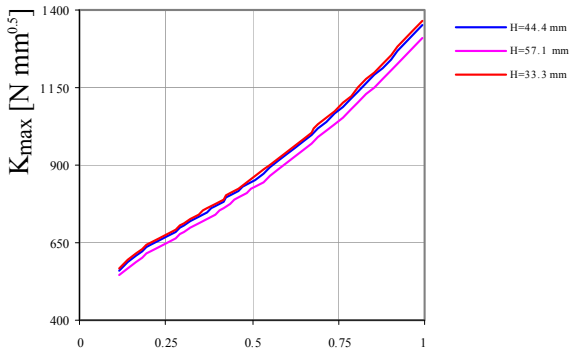

Fig. 5.4. The effects of head of length (H) in function of crack length to SIF of *Lug. No: 7 (H=33.3), 2 (H=44.4), 6 (H=57.1)*

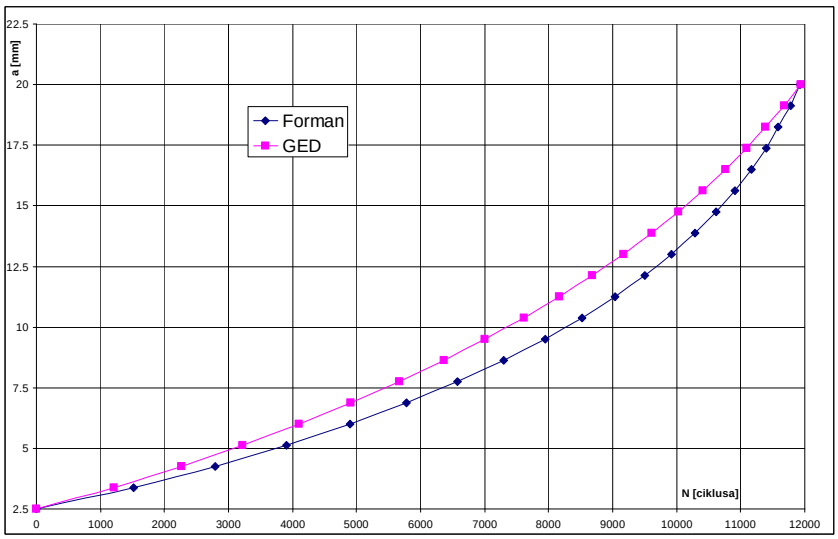

Fig. 5.5 Comparisons crack growth results of cracked lug using two crack growth models: (1) Forman`s and (2) Strain Energy Density (GED)

In Fig. 5.5 are shown results of crack growth results for cracked lug using two methods: (1) conventional Forman`s method and (2) strain energy density method[7] (GED).

5.2 The effects of shape lug`s surface crack on fatigue life

Analytic expressions for determination of SIF for lug with semi-elliptic surface crack, are given in section 4.2 and can be used for residual life estimation.
In Fig. 5.2.1 are shown results of crack growth of cracked lugs No. 2 which geometric properties are given in Figures 4.1.1 and 4.2.1.

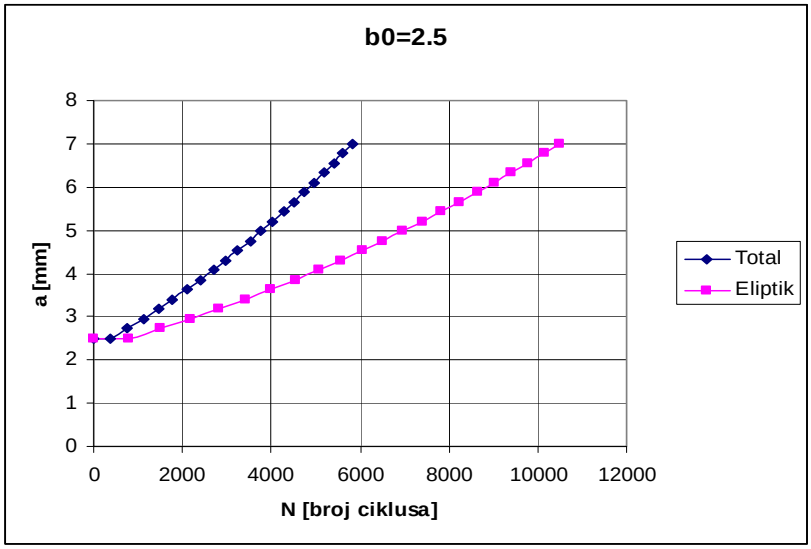

Fig. 5.2.1. Comparisons crack growth results of attachment lug with crack through the thickness and semi-elliptic surface crack

In Figure 5.2.1 is shown the effect of lug`s shape of surface crack on residual fatigue life. As expected reduced life has lug with crack through the thickness ("total") then lug with semi-elliptic surface crack ("eliptik").

5. Conclusions

This investigation is focused on developing efficient and reliable computation methods for fatigue life estimation of damaged structural components. An special attention has been focused on determination of fracture mechanics parameters of structural components such as stress intensity factors of aircraft cracked lugs. The effects of shape of lug`s surface crack on residual fatigue life is investigation too.
Predictions and experimental investigations for fatigue life of an attachment lug under load spectrum were performed. From this investigation followings are concluded:
A model for the fatigue crack growth is included which incorporates the low cycle fatigue properties of the material.
Comparisons of the predicted crack growth rate using strain energy method method with experimental data and conventional Forman`s model points out the fact that this model could be effective used for residual life estimations
The stress intensity factor of cracked lug is well defined by analytical method since there is really minor difference when compared results obtained by singular finite elements.
The effects of of shape of attachment lug`s surface crack on residual fatigue life is evident.

Acknowledgments

The authors would like to thank the Ministry of Science and Technological Development of Serbia for financial support under the project numbers TR 35045 and OI 174001.

References

[1] "Airplane Damage Tolerance Requirements", MIL-A-83444, Air Force Aeronautical Systems Division, July 1974.
[2] Brussat, T.R., Kathiresan, K and Rud, J.L., Damage tolerance assessment lugs, Engineering Fracture Mechanics, 23, 1067-1084, 1986
[3] Maksimović, S., Fatigue Life Analysis of Aircraft Structural Components, Scientific Technical Review, 2005.
[4] Maksimović K., Nikolić-Stanojević V., Maksimović S., MODELING OF THE SURFACE CRACKS AND FATIGUE LIFE ESTIMATION, ECF 16, 16th European Conference of Fracture, ECF 16, Alexandroupolis, Grčka, 2006.
[5] Maksimović, S., Boljanović, S, Maksimović, K., Fatigue life prediction of Structural Components under variable amplitude loads, FATIGUE 2002, 8th International Fatigue Congress (IFC8), Stocholm, 2-6. June, 2002.
[6] Antoni, N and Gaisne F., Analytical modeling for static stress analysis of pin-loaded lugs with bush fitting, Applied Mathematical Modeling, 35, 2011, 1-21.
[7] Liu, Y.Y and Lin F.S., A mathematical equation relating low cycle fatigue data to fatigue crack propagation rates. Int. J. Fatigue, Vol. 6 (1984), pp.31-36
[8] Forman, R. G., and Mettu, S. R., "Behavior of Surface and Corner Cracks Subjected to Tensile and Bending Loads in Ti-6Al-4V Alloy," *Fracture Mechanics: Twenty-second Symposium, Vol. 1, ASTM STP 1131*, H. A. Ernst, A. Saxena, and D. L., McDowell, eds., American Society for Testing and Materials, Philadelphia, 1992, pp. 519-546.
[9] Forman, R.G., V.E. Kearney and R. M. Engle, Numerical analysis of crack propagation in cyclic loaded structures, J. Bas. Engng. Trans. ASME 89, 459, 1967.
[10]] Liu S.B and Tan C.L., Boundary element contact mechanics analysis of pin-loaded lugs with single cracks, Engineering Fracture Mechanics, Vol. 48,No.5, 717-725, 1994.
[11] Maksimović, S., Boljanović, S., Fatigue Life Prediction of Structural Components Based on Local Strain and an Energy Crack Growth Models, WSEAS TRANSACTIONS on APPLIED and THEORETICAL MECHANICS, Issue 2, Volume 1, 2006, pp 196-205..
[12] Maksimović, K., Maksimović, S., Analytic approach for determination of fracture mechanics parameters and crack growth analysis of 3-D surface cracked structural elements, Technical Diagnostic, Vol. III, No. 1, 2004.
[13] Maksimović K., Damage tolerance analysis of aircraft constructions under dynamic loading, Master Thesis, Faculty of Mechanical Engineering, 2003.
[14] Ball D, Norwood D, TerMaath S. Joint strike fighter airframe durability and damage tolerance certification. In: Proceedings of the 47th AIAA/ASME/ASCE/AHS/ASC structures, structural dynamics, and materials conference, Newport, Rhode Island, USA; May 2006.
[15] Schijve J. Fatigue of structures and materials in the 20th century and the state of art. Int J Fatigue 2003;25:679–702.
[16] Lukaš, P., Stress intensity factor for small notch-emanated cracks, Engineering Fracture Mechanics, 26 (3), 471-3, 1987.
[17] Wormsen, A., Fjeldstad, A., Harkegard, G., The application of assimptotic solutions to a semi-elliptical crack at the root of a notch, Engineering Fracture Mechanics, Vol. 73, 1889-1912, 2006.

NUMERICAL MODELLING OF MASONRY WALLS SUBJECTED TO LATERAL IN-PLANE LOAD

R. Mandić[1], R. Salatić[2], Z. Perović[3]
[1] Faculty of Civil Engineering
The University of Belgrade, Bulevar kralja Aleksandra 73, 11000 Belgrade
e-mail: rale@grf.bg.ac.rs
[2] Faculty of Civil Engineering
The University of Belgrade, Bulevar kralja Aleksandra 73, 11000 Belgrade
e-mail: salatic@grf.bg.ac.rs
[3] Faculty of Civil Engineering
The University of Belgrade, Bulevar kralja Aleksandra 73, 11000 Belgrade
e-mail: zperovic@grf.bg.ac.rs

Abstract. Masonry walls are traditionally used as main vertical structural elements in low rise buildings. The masonry walls are also used as infill in high rise frames, but in this case their presence usually is neglected in the structural design although they significantly modify the structural response especially in the case of seismic loading. Seismic resistance of masonry wall depends on wall geometry, vertical loads and on characteristic of brick-mortar interface connection. The nonlinear response of the connection between unit and mortar represents the most important feature of masonry behaviour which has to be considered in the modelling of masonry. In this paper some results of a numerical finite element study on the monotonic response of masonry panels subjected to lateral loading are given. A comparison between numerical results and experimental data points out the ability of the proposed model to trace the overall shear performances of masonry walls.

1. Introduction

Beside the stone, masonry is the oldest building material and it still widely present in building construction. In many existing buildings masonry walls are main vertical bearing elements. In Serbia and surrounding countries the masonry in low rise buildings is extensively used with vertical and horizontal belt beams. In high rise reinforced concrete frames the masonry infill are treated as a secondary (non-structural) element. However, they significantly influence the response of framed structures, particularly in the case of earthquake loading, by increasing the initial stiffness and changing the dynamic properties of the whole system by forming the mechanism with large dissipation energy in the case of reversed dynamic response.

The full understanding of behavior of masonry walls under lateral load is important from the point of view of seismic assessment and retrofitting of existing buildings or the construction of new ones.

For the walls subjected to in-plane lateral loading the cracking of mortar joints starts for very low levels of lateral loading. This generate non-linear response from the very

beginning of loading far prior to reaching ultimate load levels. The ultimate load level depends on geometric and material wall parameters, particularly the properties of joints, and the vertical loading. The failure process is accompanied with relatively small global deformation, although large discontinuities between units or due to cracking of units may occur.

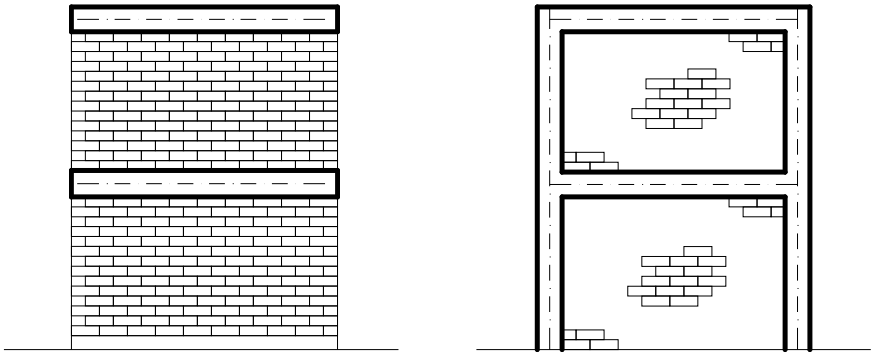

Figure 1. Masonry wall as main bearing element (left), reinforced concrete frame with masonry infill (right)

Traditionally, laboratory (e.g. [1], [2], [3]) or *in-situ* [4] tests of masonry walls subjected to lateral loads or tests are used for better understanding of the failure mechanism and evaluating shear resistance. A good review of various experimental techniques is given in [5]. In [1] a discussion of applicability of various strength equations with respect to failure mechanisms is presented, while in [7] various standards for the design of shear capacity of masonry walls are compared.

2. Modelling of masonry

In the last few decades computational methods based on non-linear finite element analysis and complex are emerging as a powerful tool in the analysis of masonry structures. Generally, depending on the level of complexity and accuracy, the three concepts can be used in numerical modeling of masonry. These three concepts can be classified as micro-modelling, macro-modelling and global modelling.

Micro-modeling - both masonry units and mortar joints are modeled with individual elements. The primary aim of such micro-modelling approach is to study the influence of various factors of masonry (bricks and mortar properties, arrangement and dimensions of units, response at interface), a complete understanding of failure mechanism of masonry elements and the minimizing the requirement for experiments on physical models. For this type of modelling the properties of individual parts (units and mortar) are obtained from laboratory tests. Although such approach allows the analysis of the complex non-linear response, the great computational effort and numerical difficulties restrict the application of

this approach to individual structural parts (e.g. walls). Note that in the finite element micro-modelling strategy two concepts can be realized. First, both units and mortar joints are considered as continuum. The interface is established on the contact between mortar elements and unit elements. In the second one, the properties of mortar and properties of mortar-unit connection are lumped into thin elements between them [8]. For the interface element zero thickness elements with modeling traction-separation (both opening and shear) response can be also used [10].

Macro modelling is based on the smearing the properties of joints and units into averaged equivalent anisotropic continuum [9]. The different levels of complexity are possible in the process of macro-modelling. ([11], [12], [14]). Beside micro-modeling, the macro-modeling approach is also suitable for the analysis of individual structural elements and may be used for the establishing global force-displacement relationship.

Global modeling represents the next step in simplification of the analysis of masonry walls. The main concept in this approach is establishing relationships between forces and deformations for elements which can be used for direct modeling of large portions of structures, e.g. piers and shear walls. The force displacement relationship are obtained from experimental tests or micro/macro-modelling procedures. For the modelling of the dynamic response these models have to capture stiffness and strength degradation due to reversed loading. The model with substituting diagonal strut [15], [16] for the modeling of masonry infill panels in reinforced concrete frame represents represent a good example of global approach. It is inspired by limit analysis and assumed stress field in two dimensional panel surrounded by reinforced columns and beams.

3. Constitutive models

For the correct modeling of masonry walls subjected the understanding of failure mechanism is of utmost importance. A lot of experimental and theoretical work has been carried out so far for the predication of the shear capacity of walls subjected to shear loading.

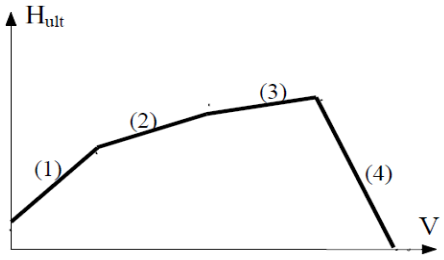

Figure 2. Failure surface of masonry wall - Mann and Müller [7]

According to Mann and Müller – see [7], the following failure modes can be observed in vertically pre-compression shear walls subjected to monotonically increased shear load.

(1) Failure due to opening of horizontal joints due to bending
(2) Tensile and shearing failure of joints due to decohesion and friction
(3) Tensile failure of units plus tensile and shearing failure of joints
(4) Compression failure of units

The mode (1) takes place in the case of very low vertical loads. The failure mode (4) is characteristic in the case of high vertical compression stresses. The second and third mode are usually accompanied by stepping failure mode in joints or/and in units. The diagonal cracks pass through vertical and horizontal joints, or in the case of higher vertical loads through units.

In our research we have been so far focused on the analysis of masonry walls having failure modes (1) and (2). The understanding and correct modeling of interface between mortar and units represents key moment in correct numerical modelling of masonry. Non linear response of joints is the result of fracture process (decohesion) which takes place along joints either in mortar or in the mortar-unit interface. We shall consider this as unique process of failure in joints. It results in some peak strength followed by a softening, both in tension and in shear. In tension when the cohesive strength is lost, the tensile strength drops to zero (mode I). In the case of shearing under compressive normal pressure, the decohesion (mode II) is followed by the presence of residual strength due to friction.

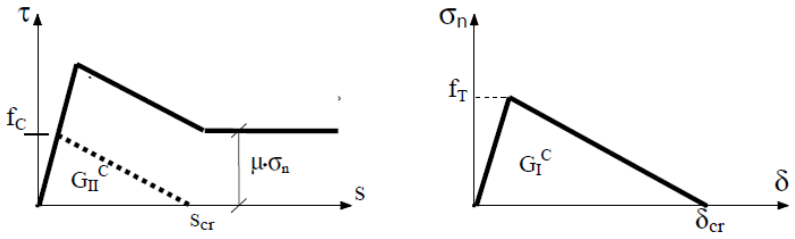

Figure 3. Shear – slip response – mode II (left), Opening mode I (right)

For joints in pure tension (mode I) Rankin type yield criterion can be used to describe failure surface which exhibit softening:

$$F = \langle \sigma_n \rangle - f_t(\lambda_n) = 0 \tag{1}$$

The $\langle \sigma_n \rangle$ denotes the contribution of tensile stresses only, while scalar parameter λ_n controls softening. If triangular type of cohesive law is adopted (see Fig. 3) we have

$f_t(\lambda_n) = (1-\lambda_n) f_t$ and the following energy release: for $\delta \le \delta_0$ we have $G_I = 0$, after the crack initiation $\delta_0 \le \delta \le \delta_{cr}$ the released energy due to normal stresses σ_n is:

$$G_I = \frac{\delta - \delta_0}{\delta_{cr} - \delta_0} G_I^C \qquad \delta_{cr} = \frac{2G_I^C}{f_t} \tag{2}$$

For $\delta \ge \delta_{cr}$ (complete fracture) $G_I = G_I^C$ where G_I^C denotes the fracture energy corresponding to mode I.

The similar expression can be written for mode II. However, the presence of confining stresses and friction in joints has to be considered. In the case pure of shear and monotonic increase of slip, the presence of cohesion and friction have to be modelled. The experimental results (Van de Pluijm [20]) support the implementation of modified Mohr-Coulomb law [19] – see figure 2. Note also, that the same experimental research [20] correlate G_{II}^C to confining stress. However, this issue has not been considered in our work.

The initial, intermediate and final yielding surfaces in pure sliding mode can be written in the following form:

$$F = |\tau_s| + \mu[\sigma_n] + (1-\lambda_s) f_c = 0 \tag{3}$$

where $[\sigma_n]$ denotes contribution only from compression stresses, while f_c is the cohesion strength in shear. The parameter λ_s controls decohesion in mode II. The state $\lambda_s = 0$ denotes no damage. In the case of linear softening in the range $s_{cr} \ge s \ge s_0$ we have $\lambda_s = (s - s_0)/(s_{cr} - s_0)$ and corresponding energy release:

$$G_{II} = \frac{s - s_0}{s_{cr} - s_0} G_{II}^C \qquad s_{cr} = \frac{2G_{II}^C}{f_C} \tag{4}$$

where G_{II}^C is the fracture energy for mode II. When critical shear separation is reached $s \ge s_{cr}$ and $\lambda_s = 1$, a complete fracture in shear occurs followed by the residual resistance due to friction in the case of confining normal stress.

In reality, the response of tensioned joints is governed by the mixed mode, i.e. opening - slip mode. In this case the damage initiation is governed by a single criterion:

$$\left(\frac{\tau_s}{f_c}\right)^2 + \left(\frac{\langle \sigma_n \rangle}{f_t}\right)^2 = 1 \tag{5}$$

The damage initiation is followed by process of softening which yields to final failure. The final failure may be described by mixed mode criterion:

$$\frac{G_I}{G_I^C} + \frac{G_{II}}{G_{II}^C} = 1 \tag{6}$$

where G_I and G_{II} are energies released per unit area done by tensile and shearing stress due corresponding conjugate displacements.

For limitation of compressive stresses in joints, the compression yield surface have to be adopted. The issue is not considered in our present work and is not discussed here. Elastic response of joints, prior to cracking initiation, i.e. pure elastic response is governed by the law: $\sigma_n = k_{nn}\varepsilon_{nn}$ and $\tau_s = k_{ss}\,\varepsilon_{sn}$. The response of masonry walls is not too sensitive to elastic properties of joints, as cracking occurs for relatively low level of loading, so even crude estimate can be used. The masonry units are assumed do be linearly elastic, so the non-linear response of walls is lumped in joints.

4. Numerical simulations

The laboratory tests of masonry walls (scale 1:1) tested at Technical University of Cataluna, Barcelona, [18] are used to validate the numerical model using finite element package Abaqus (version 6.9). In numerical simulation a simplified version of the presented material model based on average sliding resistance along horizontal joints is used. Such an approach enable simulations of low or moderate vertical pre-compressioned walls, i.e. failure modes (1) and (2).

The wall dimensions are: height 100cm, length 120cm, thickness 14cm. The following parameters are adopted for mortar joints having thickness 1cm: shear and tensile strength $f_c = 270kPa$, $f_t = 300kPa$, fracture energies corresponding to modes I and II $G_I^c = 20N/m$ $G_{II}^c = 30N/m$ friction angle $\varphi=35^0$, dilatancy angle $\psi=0$, $E_m=1GPa$ $G_m=0{,}4E_m$. In this paper we present the results of numerical simulation of walls are subjected to initial vertical compression V=150kN and V=250kN, i.e. 5,4% and 9% of vertical compressive strength which was assessed to be 16,4MPa [18]. The units with dimensions 250 x 140 x 50mm with normalized compressive strength $f_b = 50MPa$ are assumed to be linearly elastic.

The finite model is presented in the figure 4. For each masonry unit the 16 x 3 mesh with eight node brick elements in the plane of the wall is used. Vertical and horizontal joints are modeled with cohesive elements with which have axial stiffness in n direction (perpendicular to the joints) and shear stiffness in the plane of the joints. On the top of the masonry wall a beam with a large bending stiffness is placed in order to simulate the conditions from the experiments: transfer of horizontal and vertical forces uniformly into the wall and rigid rotation of the top wall edge.

In the first stage loading process the vertical load is gradually applied. In the second stage, after the pre-compression is finalized, the horizontal in plane load is applied at the top of the wall by the displacement controlled procedure.

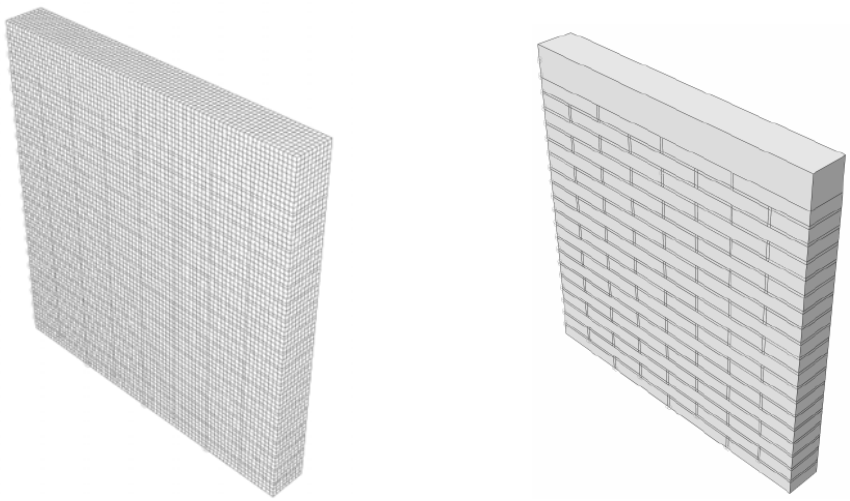

Figure 4. Finite element model

In table 1 numerical, experimental [18] and Eurocode 6 [21] shear strength resistances (horizontal force H_{ult} and shear stress τ_{ult}) are compared. The actual shear resistance is overestimated by numerical results and particularly by EC6 proposals. The numerically obtained force displacement curves are given on figure 5. The post peak response was not traced in our numerical simulations. In oppose to numerically obtained results, the force displacement curves from [18] show sharp increase of displacement for values larger then approximately H=30*kN*.

Shear strength of walls	V=150kN	V=250kN
	H_{ult} (kN)	H_{ult}(kN)
	τ_{ult} (MPa)	τ_{ult} (MPa)
Finite element	87	130
	0,52	0,77
Exp. ref [18]	80	110
	0,48	0,65
EC6[21]	105	145
	0,62	0,86

Table 1. Shear strength of walls - comparison of different methods

The figures 7 and 8 present compressive stress at the base of the wall. The stress concentrations at the right bottom corner indicate developing of a compressive diagonal strut and stress releasing at the left bottom zone. The high peaks of compression stresses indicate possible crushing of masonry.

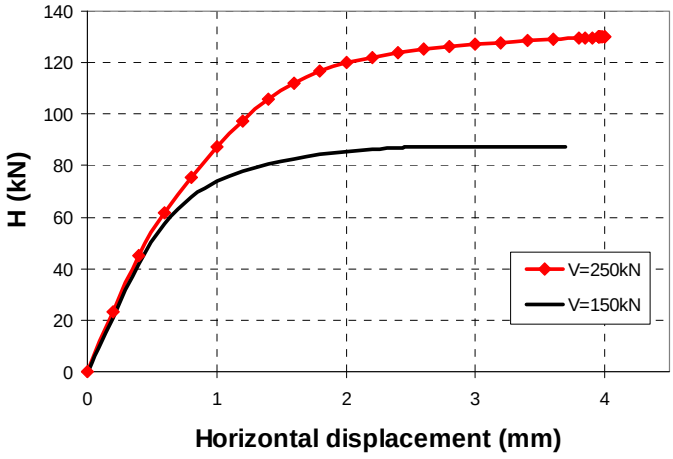

Figure 5. Horizontal force - displacement curves for two cases (vertical loads V=150kN and V=250kN)

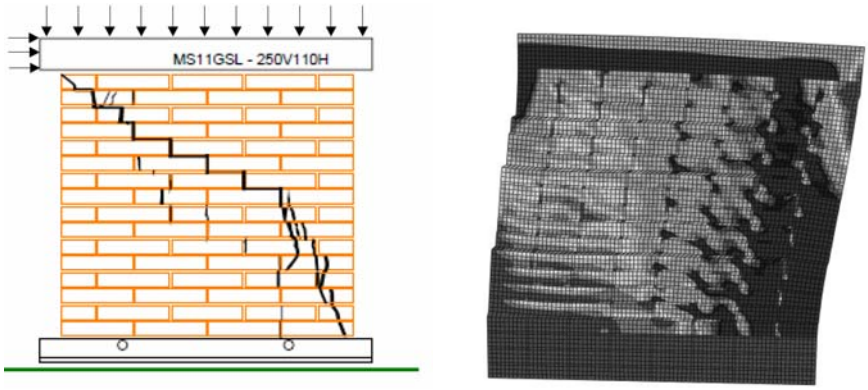

Figure 6. Experimentally [18] and numerically obtained failure pattern (deformation scale 30:1)

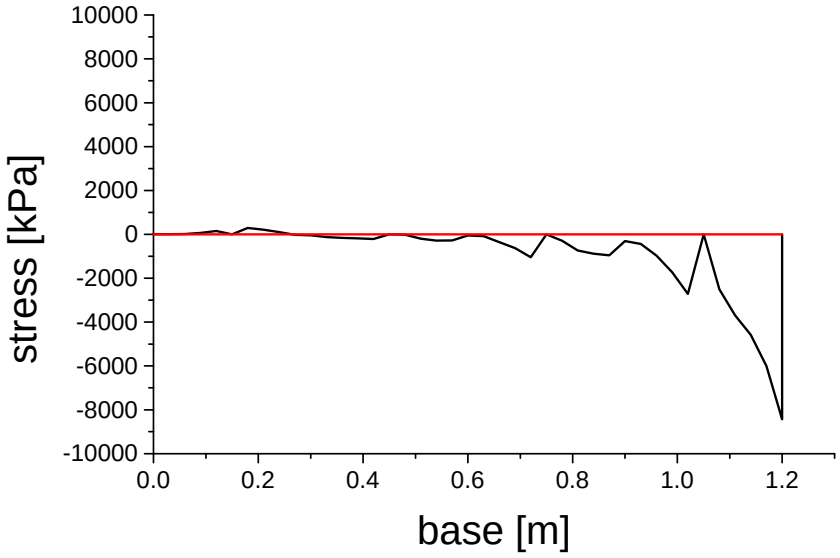

Figure 7. Contact normal stress (obtained by FE analysis) at bottom surface at failure. Case V=150kN

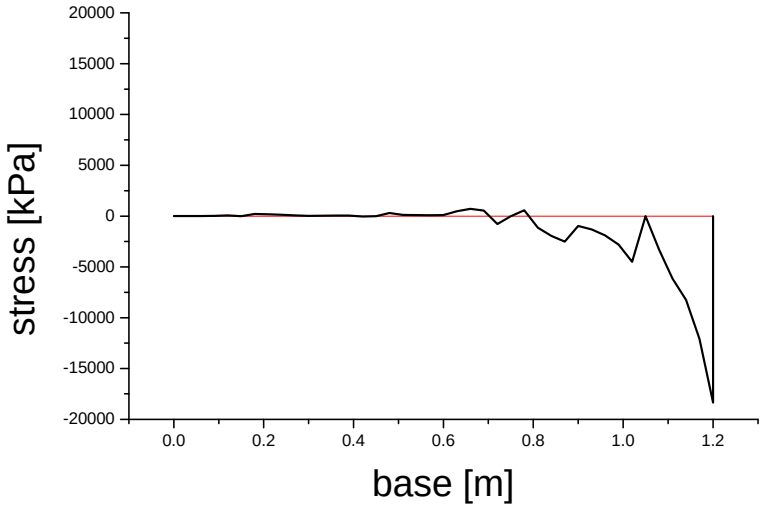

Figure 8. Contact normal stress (obtained by FE analysis) at bottom surface at failure. Case V=250kN

In table 2 there is an assessment of global moduli of a masonry wall based on response obtained by finite element model. E_w modulus is obtained from the numerical simulation of initial loading process with V=250kN. The global shear modulus is extracted from the response with horizontal load H=40kN≈H=0,35H_{ult} assuming that the total horizontal displacement is the result of bending and shear deformation.

Global moduli of masonry wall	Finite element	Exp. ref. [18]
E_w (GPa)	4,8	4,1
G_w(GPA)	1,77	1,67

Table 2.Young's and shear moduli of the masonry wall extracted from finite element analysis and experiment

5. Conclusions

A micro-modelling of masonry walls subjected to static shear in-plane loading is presented. The model has been validated by comparing the results with available experiments. After a number of numerical tests we may say that in our research overall response of masonry wall can be well predicted from the point of view of failure loads. During the loading process, a compressive diagonal strut was formed from the top-left to the bottom right corner. The cracking and shearing-off was spread in a relatively larger zone and was not localized in a „step mode mechanism". The further work, including developing user defined material models in Abaqus finite element code, is necessary in order to obtain robust and reliable various failure modes of masonry walls.

Acknowledgement. The study presented in this paper is the part of the research financed by the Ministry of science and technology, Republic of Serbia.

References

[1] Tomaževič M, Gams M and. Lu S. (2009), Modelling of shear failure mechanism of masonry walls, *Proceedings of the 11th Canadian Masonry Symposium*, Toronto, Canada.
[2] Tomaževič M., Weiss P (1994). Seismic behaviour of plain and reinforced masonry buildings, *Journal of Structural Engineering*, ASCE, 120 (2), 323-338
[3] Benedetti D., Pezzoli P. and Carydis P, (1998), Shaking table tests on 24 simple masonry buildings, *Earthquake Engin. Struct. Dyn.* Vol. 27.
[4] Muravljov M, Zakić D (2009), *Izveštaj o ispitivanju parametara čvrstoće zidova od opeke u sklopu objekta Kliničkog centra – Instituta za patlogiju u Beogradu*, Izveštaj 97/2009, Institut za materijale i konstrukcije, Gradjevinski fakultet u Beogradu.
[5] Shear test on masonry panels, Literature survey and proposal for experiments (2004), TNO report 2004/CI/R0171, TNO Building and construction research

[6] Schermer D. (2004), *Experimental and Numerical Investigations on the Behaviour Of Unreinforced Masonry Buildings Under Seismic Loadings*, Proceedings of the 13th International Brick and Block Masonry Conference, Amsterdam.
[7] Graubner C. A, T. Kranzle T (2005), *Shear Design of Unreinforced Masonry Panels - Basic Assumptions And Comparison Of Different Standards* . 10th Canadian Masonry Symposium, Banff, Alberta, Canada
[8] Lourenco, P.B., Rots, J.G,(1997). Multisurface Interface Model for Analysis of Masonry Structures, *Journal of Engineering Mechanics*, ASCE, Vol.123, No. 7, 660-668.
[9] Lourenço, P.B. J.G. Rots, J. Blaauwendraad, Continuum model for masonry: Parameter estimation and validation, *Journal of Structural Engineering* ASCE, 124(6), 1998, pp. 642-652.
[10] Daryan A S et al (2009) *A Study of the Effect of Infilled Brick Walls on Behavior of Eccentrically Braced Frames Using Explicit Finite Elements Method*, American J. of Engineering and Applied Sciences 2 (1): 96-104,.
[11] Lotfi, H. R. and Shing, P. B. (1991). An appraisal of smeared crack models for masonry shear wall analysis. *Computers and Structures* Vol.41(3): pp.413-425.
[12] Madan A, Reinhorn a. M, Mander J. B., and Valles R.E (1996), Modeling of Masonry Infill Panels for Structural Analysis, *Journal of Structural Engineering, ASCE*, pp. 1295–1302.
[13] Marcari G, Fabbrocino G, Manfredi G, Prota A, (2007) *Experimental And Numerical Evaluation of Tuff Masonry Panels Shear Seismic Capacity*, Proceedings of the 10th North American Masonry Conference, St. Louis, Missouri, USA.
[14] Gambarotta, L. and Lagomarsino S. (1997) Damage models for the seismic response of brick masonry shear walls. Part II: The continuum model and its applications, *Earthquake Eng. Struct. Dyn*., 26: 441-462.
[15] Smyrou E et al (2006) *An implementation And Verification Of A Masonry Panel Model For Nonlinear Pseudo-Dynamic Analysis Of Infilled RC Frames*, First European Conference On Earthquake Engineering And Seismology Geneva, Switzerland, Paper Number: 355
[16] Salatić R, Mandić R, Perović Z (2010) *Modeliranje zidane ispune u seizmičkom proračunu*, Savetovanje Zemljotresno inženjerstvo i inženjerska seizmologija, Divčibare 2010, pp. 107-112.
[17] Magenes G, (2006), *Masonry Building Design in Seismic Areas: Recent Experiences and Prospects from a European Standpoint*, First European Conference on Earthquake Engineering and Seismology (a joint event of the Geneva, Switzerland, paper number: keynote address k9
[18] Charry Ablanque J. A. (2010) *Experimental Study Of Masonry Wall Behaviour Under Lateral Stress*, Tesis Doctoral Departamento de ingenieria de la construcción, Universidad Politécnica de Cataluña, Spain
[19] Stupkiewicz S. Mróz Z, (2001) Modelling Of Friction And Dilatancy Effects at Brittle Interfaces For Monotonic And Cyclic Loading, *Journal Of Theoretical and Applied Mechanics,* **3**, 39, pp. 707-739.
[20] Van Der Pluijm, R. (1992). *Material properties of masonry and its components under tensile and shea*r, Proc. 6th Canadian Masonry Symp., Canada, 675 – 686.
[21] Eurocode 6, Design of masonry structures - Part 1-1: Common rules for reinforced and unreinforced masonry structures, CEN: Brussels.
[22] Abaqus, ver. 6.9 (2008), Users manual, Dassault Systèmes Simulia Corp., Providence, RI, USA.

NUMERICAL AND EXPERIMENTAL DIAGNOSTIC OF DYNAMIC BEHAVIOR OF THE ROTOR-EXCAVATOR CONSTRUCTION

T. Maneski[1], P. Jovančić[2], D. Ignjatović[2], V. Milošević-Mitić[1], N. Trišović[1]

[1] Faculty of Mechanical Engineering
The University of Belgrade, Kraljice Marije 16, 11120 Belgrade 35
e-mail: tmaneski@mas.bg.ac.rs
[2] Faculty of Mining and Geology
The University of Belgrade, Đušina 7, 11120 Belgrade 35

Abstract. Dynamic behaviour of a rotor-excavator construction is of crucial importance for proper and reliable operation. Numerical and experimental procedure shown that these structures failed due to incorrect operational parameters related to the vibration of complete supporting structures. Therefore, the base for rehabilitation and reconstruction is a dynamic diagnostics of the structure. This analysis involves a computer calculation by the finite elements method with the mandatory experimental measurements. This enables determination of the actual behaviour of structure, reliable prediction of its response in operation, determination of the cause for poor behaviour or failure, assessment of service life time of reliable operation and the scope of revitalization. Operational problems developed mostly from improper geometry design. Presented methodology is inevitable during the engineering analysis of excavator structure. This approach is justified due to low costs with a very high level of results.

1. Introduction

Rotor-excavators are very complex sistems with a great number of functionaly important elements. Working life of the rotor excavator depends of the stable of the steel structure. For a drive system we have very clear criteriums about replacement or rehabilitation which is not case for the steel structure. So, experimental tests and visual analysis have to give validation of the numerical model based on the finite element method FEM. FEM and experimental messurements are the main tools in the proces of the construction accompaniment [1].

The basis for structural performance diagnostics is the computer modelling and structural analysis calculation software with the application of finite element numerical method throughout static, dynamic and thermal calculation of consisting structural elements.

Program KOMIPS [2] allows modelling and the calculation of complex structures and problems, determination of real displacements and stresses and real structural behaviour including the consisting elements, it gives a reliable forecast of structural behaviour in service and depicts the parameters for decision making (operating regime, repairs, reconstructions, revitalizations, optimizations, confirmations of selected solution variants), poor performance sample identification or structural deterioration, service life estimation and time of reliable operation efficiency. Every improvement of structural performance that can be reached by this approach allows service life extension and increase of reliability.

The developed system KOMIPS includes specific calculus for closer defining structural state and behaviour. The equivalent stress, according to the Huber–Hencky–Misses theory,

is calculated for all types of finite elements and global nodes. The distribution of load, membrane and bend stresses, deformation energy, kinetic and potential energy allows very efficient analysis [3] of the state and structural behaviour diagnostics for the designed or produced structure.

Experimental tests in this case are intended for:
– determining the external and internal loads acting on the structure in service, and
– measuring the deflection, stress, acceleration at particular locations on the structure.

These tasks define the relevant input loads for the calculation and verify the results. Applying the above mentioned calculation minimizes the extent of tests. Both static and dynamic tests are presumed. Stress measurements suggest the application of the extensometer method (strain gauges). Acceleration is measured directly, by applying sensors. Measurements of the deformation rate are often used in vibration diagnostics. By measuring the acceleration on certain locations of the structure and by performing dynamic calculations of the structure it is possible to define the cause for poor structural behaviour. Problem solving of the cause is further accomplished by numerical analysis.

2. Experimental messuring on rotor excavator SchRs630

Tests which were done on the rotor excavator SchRs630 (on the waste dump Tamnava Zapadno polje, Kolubara) had the purpose to define state and the bahavior of the steel construction during the selective work.

Figure 1. Vertical cross-section of the coil-block and excavator SchRs630

All parameters were obtained during work, for rigid highs of cuts: 0.5-0.7 m, 1-1.2 m, 2-2.2 m and for 5-7 m. The whole high of the coil-block was 10.5 m.

The characteristis place for the measuring was on the lug of the slice of the will-excavator.

Figure 2 presents appropriate measuring place.

Figure 2. Measuring place

Stress was measured using three strain gauges. On the same time, accelerations were obtaining. Instalation of the strain gauges was done on the static-loaded construction.

Measurings were done in next order:

1. Stress and acceleration for cut-high of h = 5.3 m and for advent of 40 cm and 20 cm (for left and right direction),
2. Stress and acceleration for cut-high of h = 2 m and for advent of 70 cm and 35 cm (for left and right direction),
3. Stress and acceleration for cut-high of h = 1 m and for advent of 60 cm and 30 cm (for left and right direction),
4. Stress and acceleration for cut-high of h = 0.7 m and for advent of 80 cm and 40 cm (for left and right direction).

Obtained diagrems for stress accession and for acceleration in time and frequent domain are presented on figure 3 for the first case of loading.

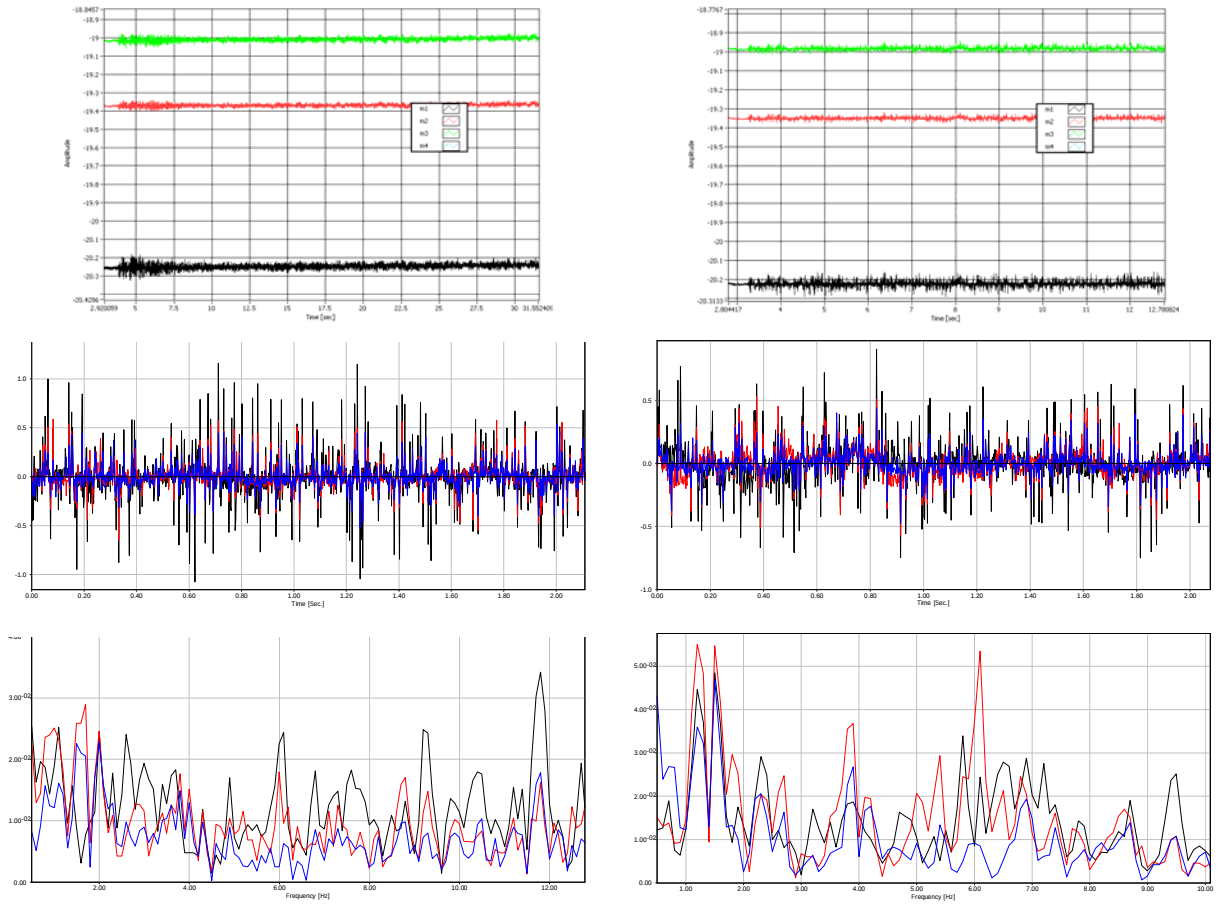

Left Right

Figure 3. Stress, accelerations in time and frequent domain in the first case

During left cuting, stress accession was between 50-55 N/mm^2 at the begining of the process and then decreased to 15-25 N/mm^2. Acceleration in time domain was to 1G, which was satisfied. But, low frequences to 10 Hz was obtained on the steel structure.

During right cuting, stress accession was as in the previous case 50-55 N/mm^2 at the begining of the process and later 10-40 N/mm^2. Acceleration in time domain was to 0.8G, which was satisfied. Diging frequecy of 2.7 Hz wasn't dominant.

Figure 4 shows obtained diagrams for the second group of measurings.

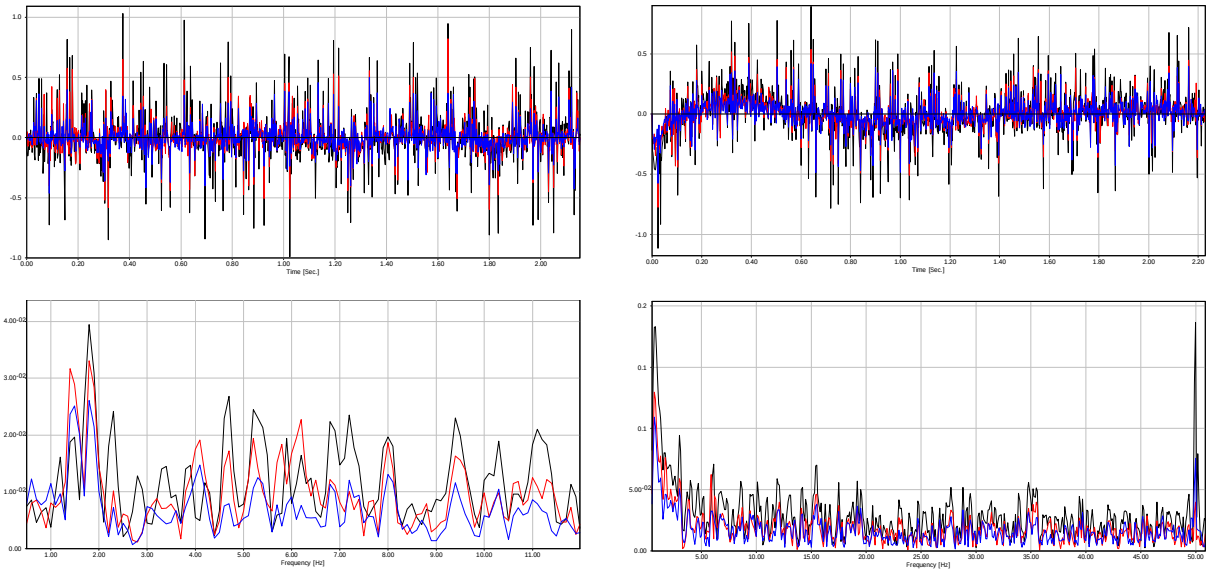

Left, 70 cm Left, 35 cm

Figure 4. Accelerations in time and frequent domain in the seccond case

Left cuting of 70 cm gives stress accession of maximal 60-70 N/mm^2 at the begining and about 20-40 N/mm^2 later. Stress was high but in limited value. Acceleration was to 1G, which was satisfied. The amplitude of the characteristic frequences was to 0.04 m/s^2.

Left cuting of 35 cm gives stress accession of maximal 45-50 N/mm^2 at the begining and about 15-30 N/mm^2 later. Acceleration was to 1G, which was satisfied. The amplitude of the characteristic frequences was to 0.15 m/s^2.

Figure 5 shows obtained diagrams for the third group of measurings.

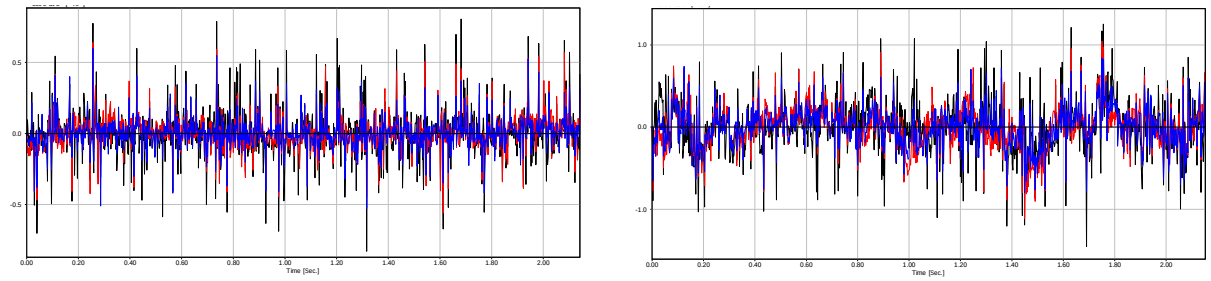

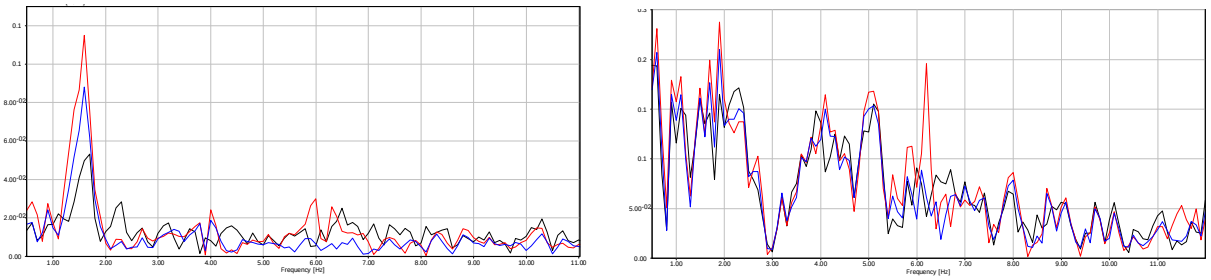

Right, 60 cm Right, 30 cm

Figure 5. Accelerations in time and frequent domain in the third case of loading

Right cutting of 60 cm gives next values:
- Sterss accession of 30-40 N/mm^2 the the begining and 10-25 N/mm^2 later,
- Acceleration in time domain 0.75G maximum,
- Low frequencies to 10 Hz of steel construction,
- Amplitude of the characteristic frequences to 0.13 m/s^2.

Right cutting of 30 cm gives next values:
- Sterss accession of 25-30 N/mm^2 the the begining and 10-20 N/mm^2 later,
- Acceleration in time domain 1.2G maximum,
- Amplitude of the characteristic frequences to 0.25 m/s^2.

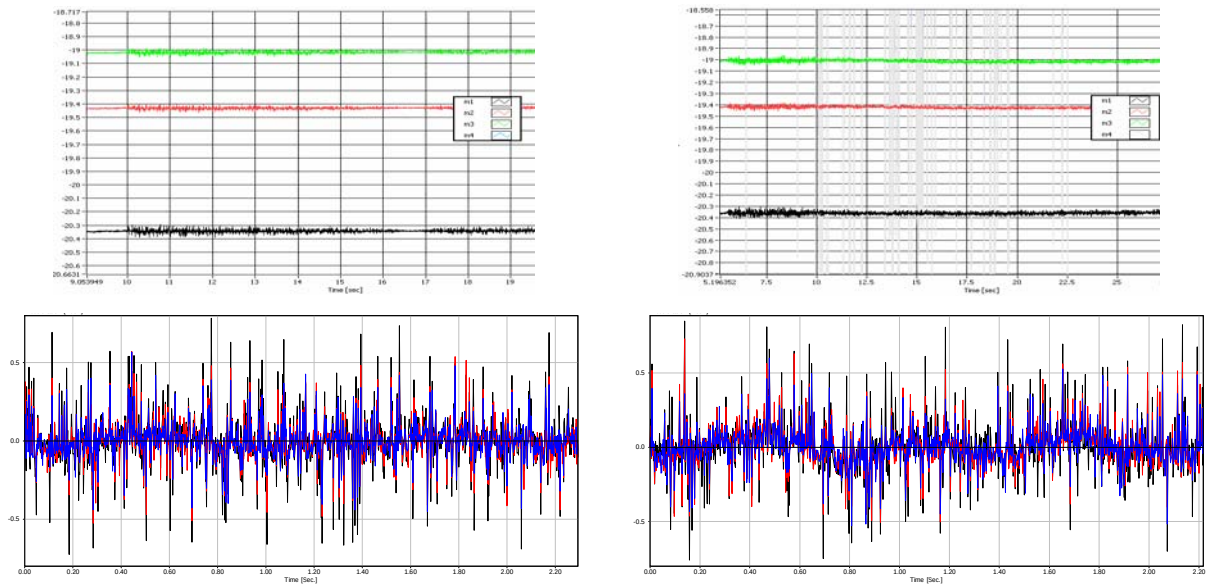

Left, 80 cm Right, 40 cm

Figure 6. Stress and accelerations in time domain in the fourth case

Obtained results are presented in next table.

Table 1. Results in the fourth case of loading

	Sterss accession	Acceleration	Amplitude	Frequencies of steel structure
Left, 80 cm	35-45 N/mm^2 10-25 N/mm^2	0.7G	0.03 m/s^2	to 10 Hz
Right, 40 cm	35-45 N/mm^2 10-25 N/mm^2	0.7G	0.085 m/s^2	to 10 Hz

3. Numerical model of the rotor-excavator steel structure

Dynamic behaviour diagnostics of the operating wheel cantilever beam was done using program package KOMIPS. Shown below are major oscillation forms of the operating wheel for two outermost cantilever positions (A and B).

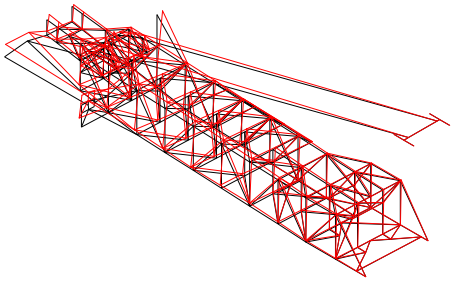

Position A: f_{01} = 0.8 Hz, f_{02} = 1.3 Hz

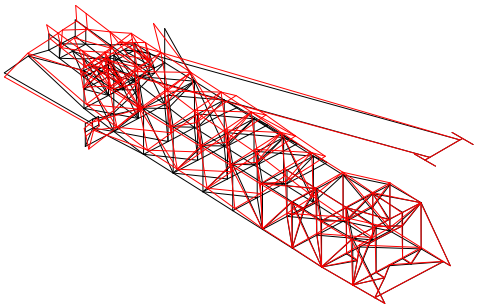

Position A: f_{03} = 2.3 Hz, f_{04} = 3.3 Hz

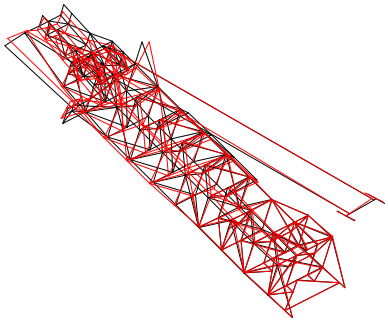

Position B: f_{01} = 0.8 Hz, f_{02} = 1.6 Hz

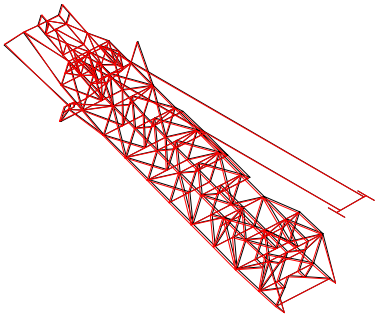

Position B: f_{03} = 2.7 Hz, f_{04} = 3.4 Hz

Figure 7. Main oscillating forms of operating wheel cantilever in positions A and B

The main diagnostic element is defined by the unloading range (number of buckets × operating wheel revolutions). The unloading number must correlate to eigen-value oscillations of the operating wheel cantilever beam. From the cantilever dynamics point of view,

the number of unloads should be within (1.6÷2.3 Hz) × 60 sec = 96÷138, i.e. for a 23 bucket wheel, the revolutions should be 4.17 to 6 min^{-1}.

4. The conclusion

Diagnostic of the behaviour of the steel structure of the rotor excavator SchRs630 was based on the numerical model and the experimental tests. Obtained results show:

- load-measurings were done in dynamic-load state of the rotor excavator,
- higher stress accessions were propper to higher cut-highes and steps,
- measuring results were satisfied and in limitid values,
- experimental results validated numerical model.

Acknowledgement. This work is a contribution to the Ministry of Science and Technological Development of Serbia funded project TR 35040 and TR 35011.

REFERENCES

[1] T. Maneski, V. Milošević-Mitić, Numerical and experimental diagnostic of structural strength, Structural integrity and life, 10 (1) (2010) 3-10.
[2] G.M. Zloković, T. Maneski, M. Nestorović, Group theoretical formulation of quadrilateral and hexahedral isoparametric finite elements, COMPUTERS & STRUCTURES, 82 (11-12) (2004) 883-899.
[3] N. Trišović, T. Maneski, D. Kozak, Developed procedure for dynamic reanalysis of structures, Strojarstvo - Journal for Theory and Application in Mechanical Engineering, 52 (2) (2010) 147-158.
[4] P. Jovančić, D. Ignjatović, T. Maneski, P., Diagnosis of behaviour for support steel structure at a bucket wheel excavators, Handbook Machine design (editor S. Kuzmanović), Faculty of technical sciences University of Novi Sad (2008) pp.383-388.
[5] P. Jovančić, D. Ignjatović, T. Maneski, Analysis of loading steel structure of bucket wheel excavator by stress condition measuring, Proc. 26th Danubia-Adria Symposium on Advances in Experimental Mechanics, September 23 – 26. 2009, Leoben, Austria (2009) p.87-88.

SOME APPLICATIONS AND CONSTRAINTS OF THE FEM WITHIN THE MODAL ANALYSIS OF THE STRUCTURES

Lj. Markovic [1], D. Ruzic [2], H. Hertha-Haverkamp [3], C. Kardelky [4]

[1] Tensor GmbH
Nordbahnhofstraße 16, D-70191 Stuttgart, Germany
e-mail: lmarkovic@tensor-gmbh.de
[2] Faculty of Mechanical Engineering,
The University of Belgrade, Kraljice Marije 16, 11120 Belgrade 35, Serbia
e-mail: druzic@mas.bg.ac.rs
[3] Hochschule Reutlingen
Alteburgstraße 150, D-72762 Reutlingen, Germany
e-mail: Hans.Hertha-Haverkamp@Reutlingen-University.de
[4] Hochschule Pforzheim
Tiefenbronner Straße 65, D-75175 Pforzheim, Germany
e-mail: christian.kardelky@hs-pforzheim.de

Abstract. The contributions to the dynamic analysis of machine parts or of a group of machines as well as the algorithmic concept are given. Particular attention is paid to the modal analysis. The FEM is a very efficient method for obtaining a very quick Feed-Back – the response of the system if the input parameters of the system are given in advance. But as very often the protection of the data (e.g. the engine parameters in motor vehicle industry) is at a very high level one will meet just the inverse problem – to determine the load vector starting from the known dynamic response. It is well known that the resonant frequency field represents the particular importance for the calculations. As the experimental measurements are usually very expensive and as the rule, in the case of the dynamic analysis, they are performed only once, the relevant mathematical or FEM models are of very high importance. On the basis of theoretical knowledge of the problems from one side and of the practical experience from the other, the authors propose an algorithm for the application of the vibration analysis, where the calculation of one exhaust pipe is given as an example. The interaction between experimental measurements and the calculation is shown. The MAC-analysis, one of usually applied methods in the structural dynamics for the comparison of calculated and measured eigen-vectors, is used for the explanation of that interaction. The influence of the MAC-Matrix on the sensitive analysis as well as on the calculation of the substructure is explained.

1. Introduction`

The modal analysis although by its nature expensive one is one of the most important methods in the numerical analysis of mechanical systems. Together with the development of new hardware having more outstanding performances, from one side, and with trends of avoiding expensive experiments, from the other, the modal analysis becomes more and more important in the numerical analysis. Although the vibration analysis is performed in the finite time domain, a great part of responsibility is transferred from the measurements to the calculations. That is quite understandable because it is too expensive to perform a new experiment if only some geometrical parameters (e.g. profile thickness) or the material are changed. The simultaneous intentions of avoiding expensive experiments and of obtaining quick results often yield to some contradictions between the time and the available

resources. The efficiency of one FEM program depends on its structure and on the quantity of available processors that are needed for its performing. The intention of the paper that follows is to prove that when the modal analysis is in question the universal FEM program satisfying all requirements does not exist, and to point to some methods for solving the problems that are met in practice. Some specific industrial requirements that one FEM program can not always and completely satisfy are often faced and that is why some additional tools for solving real problems are needed.

2. Basic equations

In the domain of modal analysis the starting point is the system of differential equations

$$M\,\ddot{q} + D\,\dot{q} + K\,q = F(t)\,, \tag{1}$$

Where:

M – Mass matix,

D – Damping matrix,

K – Stiffness matrix,

$F(t)$ – Load vector,

$q = q(t)$ - Displacement vector – the dynamic response of the system to given loads.

For one discrete mechanical system, *q* represents the displacement field in nodal points. It is not necessary to know the displacement field in all nodal points as the output but it is enough to know only the system response in the points in which the measurements were performed. These points, i.e. their coordinates, are taken from the measurements and corresponding nodal points are found in the FEM model. These points are suitably chosen in the mechanical system in order to obtain significant information about the spectral and modal behavior of the system.

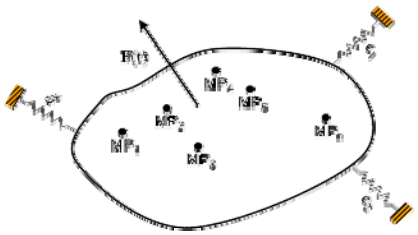

Fig. 1.Generalized mechanical model for the analysis

If there are *n* points (Fig. 1) then the response at the *kth* point MP_k will be denoted by $\mathbf{q}_k$ and corresponding components by u^k,v^k,w^k or

$$q_M^k = \begin{pmatrix} u^k \\ v^k \\ w^k \end{pmatrix}, \tag{2}$$

The total displacement vector is given by

$$q_M = \begin{pmatrix} q_M^1 \\ q_M^2 \\ q_M^3 \\ . \\ . \\ q_M^n \end{pmatrix}, \tag{3}$$

or, through the corresponding components, by

$$q_M^T = \left(u^1.v^1.w^1.I.u^2.v^2.w^2.I.....u^n.v^n.w^n\right) \tag{4}$$

From the mathematical point of view, there exists such an equivalent system that gives the identical displacement, or there exists a system of differential equations

$$M_{eq} \cdot \ddot{q} + D_{eq} \cdot \dot{q} + K_{eq} \cdot q = F_{eq}(t) \tag{5}$$

Where:

M_{eq} – Mass matrix,

D_{eq} – Damping matrix,

K_{eq} – Stiffness matrix,

$F_{eq}(t)$ – Load vector,

for the equivalent system that has to be determined.
The importance of the formulation of the equivalent model will be noticed later.

3. Modal analysis

The authors present the algorithm in the schematic form in order to show what a modal analysis applied to the calculation of one mechanical system is supposed to look like.
The standard input consists of the geometry of the model, where material data and boundary conditions are defined in advance and where also the springs with their axial and torsional stiffnsses (Fig.1) are introduced.

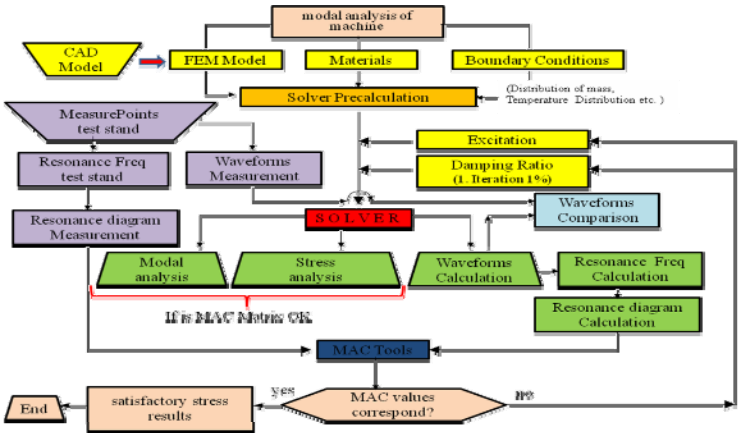

Fig. 2. The proposed algorithm for the modal analysis

The precalculation is performed before the main calculation in order to ensure high and satisfactory accuracy of the solution. For example, the exact distribution of mass that corresponds to the physical model is prerequisite for the good result within the main calculation.

Strictly speaking, it is also possible to make a model that does not correspond to the physical model from the point of view of mass distribution or from the point of view of some other criteria and it is possible that such a model will give good results, but only for the previously defined parameters. Any change concerning the geometric or material characteristics in the FEM model, as already mentioned, does not follow any more real responses of the system caused by the changes in the physical model. That is why the MAC analysis, explained later, is of particular importance.

The responses of the system in each particular measure point, and in each direction, are obtained from the measurements as it is shown in Fig. 3 for one measurement.

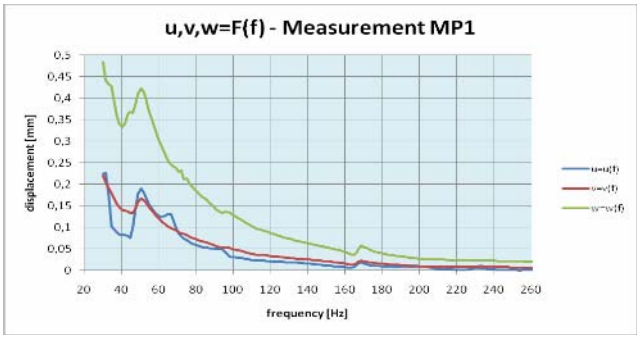

Fig. 3. Measurement results at the measure point 1 (MP_1)

The same kind of data is obtained for all other measure points.

The data (6) concerning the engine are included into the input data.

$$F_x = F_x(\Omega)$$
$$F_y = F_y(\Omega) \quad (6)$$
$$F_z = F_z(\Omega)$$

with corresponding phase differences

$$\varphi_{Fx} = \varphi_{Fx}(\Omega)$$
$$\varphi_{Fy} = \varphi_{Fy}(\Omega) \quad (7)$$
$$\varphi_{Fz} = \varphi_{Fz}(\Omega)$$

The same is valid for the moment as the phase impulse

$$M_x = M_x(\Omega)$$
$$M_y = M_y(\Omega) \quad (8)$$
$$M_z = M_z(\Omega)$$

with corresponding phase differences

$$\varphi_{Mx} = \varphi_{Mx}(\Omega)$$
$$\varphi_{My} = \varphi_{My}(\Omega) \quad (9)$$
$$\varphi_{Mz} = \varphi_{Mz}(\Omega)$$

Next problem that is imposed is damping as a natural phenomenon. As the damping matrix is not given explicitly, modal coordinates must be introduced. In general case the damping matrix is not diagonal and it does not need to be symmetrical. That is caused by the complexity of the procedure where the reactions or dissipative forces are acting in such a way that the loss of the mechanical energy is appearing. And usually there is no reliable information concerning the values of the amplitudes in resonant region.

As an iterative procedure is in question it has been thought out to introduce a modal damping having the value of 1% in the very beginning of the calculations.

It is understandable that after the first calculation with the first iteration the accuracy of the results can be in question. Assuming that the results of the measurements and the FEM model are correct, it can happen that the calculated resonant frequencies are not too far from the measured ones. In the first approximation the calculated resonant frequencies usually differ (they are lower or higher) from those that are measured.

One possible approach is the direct comparison of the dynamical responses in each measure point and the difference measurement-calculation can immediately be noticed on the local level as it is shown in Figs. 4.a, b, c.

Another possibility for realizing the difference consists in the use of diagram for the whole mechanical system as shown in Fig. 5. After the iterative procedure the damping function is obtained as shown in Fig.5. It is a stepwise one because the damping is modal, and from the other side a linear dynamic is in question.

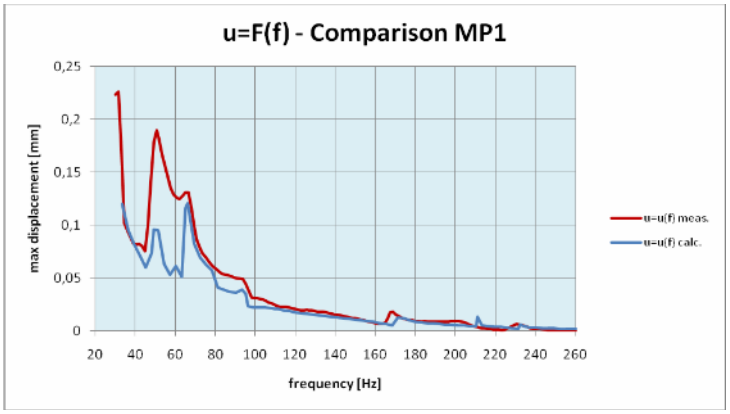

Fig. 4,a. Comparative analysis of dynamical response in x-direction

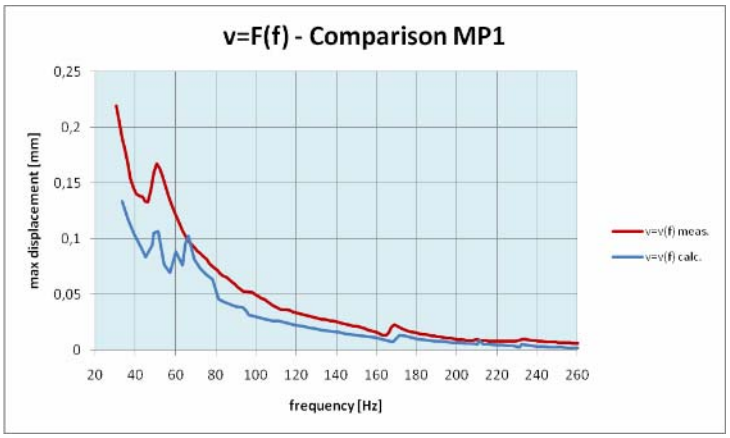

Fig. 4,b. Comparative analysis of dynamical response in y-direction

4. MAC-Matrix (Modal Assurance Criterion)

Anyhow, one of very efficient methods today for the determination of the differences from the measured values is so called MAC-Matrix (Modal Assurance Criterion).
A MAC-matrix element is defined as a normalized scalar product of the measured and calculated eigen-vectors.

$$MAC(i,j) = \frac{(v_{calc}^{(i)T} * v_{meas}^{(j)})^2}{(v_{calc}^{(i)T} * v_{calc}^{(i)})(v_{meas}^{(j)T} * v_{meas}^{(j)})} \qquad (10)$$

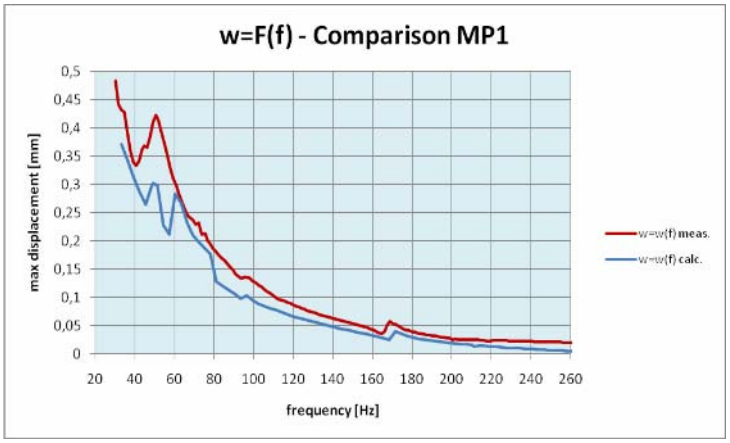

Fig. 4,c. Comparative analysis of dynamical response in z-direction

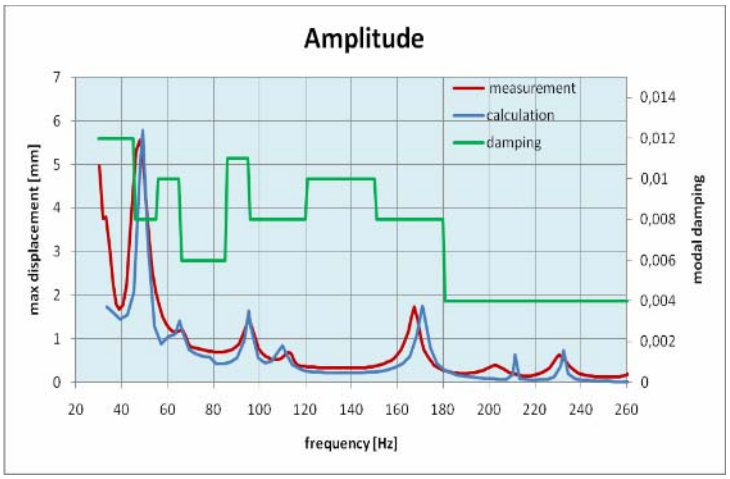

Fig. 5. Comparative diagram of the total mechanical system

The MAC element represents the square of the cosine of the angle between these two vectors,

$$MAC(i,j) = cos^2 < (v_{calc}^{(i)}, v_{meas}^{j}) \qquad (11)$$

It is obvious from (11) that the best matching of two vectors happens if the angle is zero, and in the ideal case the element will have the value equal one. It is understandable why the MAC matrix is introduced in the form (10) as a measure of coincidence of measurements and calculations.

The MAC analysis is not only the starting point and the basis that is used for obtaining the correct stress field in the model. It is prerequisite for the further analysis and some examples will be given.
1) Let us take an example from the practise where starting only from the dynamical response obtained by measuring, it is necessary to find the stress field without defined given loads (such an example can particularly be found in automotive industry due to their protection of the data). In this case the most appropriate way is to define the equivalemt system according to (10), and it leads to the same stationary system response. The shortest description of the problem could be in this case to find the loads that lead to the wanted stress field.
2) As another problem the optimization of a structure, particularly the sensitive analysis can be cited. The equivalent systems are introduced in this case not from the reasons described in 1) but in order to save the calculation time. Here, some simpler elements are used: e.g. instead of shell elements, the bar type and spring type elements. In order to achieve the behavior of the new system as approximate to the real system as possible, it is necessary to check matching of the system. It means that the MAC analysis must be performed.

Conclusions

As it has been mentioned the MAC analysis is a necessary condition or even prerequisite for the expansion of any analysis from the point of view of the comparison of the results. And, as it has been showed in examples 1) and 2) the MAC is used not only when the measurements are in question but also when two calculation models are investigated. That is why the MAC method is in the central position in modal analysis when it is necessary to compare the results (Fig.2). The problem becomes even more interesting if taking into account the fact that the FEM programs do not contain the possibilities for an analytical approach to this method, but it is based on the skill of the engineer.

Acknowledgement. The first author Lj.M. is grateful to his supervisor during the work on Master and Doctoral thesis Professor D. Ruzic for long cooperation lasting for years, and the fourth author C.K. is dedicating the paper to Univ.-Prof. Dr.-Ing. habil. D. Gross, TU Darmstadt, on the occasion of his 70th birthday.

References

[1] Gasch R, Knothe K (1987) *Strukturdynamik; Band 1, Diskrete Systeme*, Springer-Verlag, Berlin.
[2] Gasch R, Knothe K (1989) *Strukturdynamik; Band 2, Kontinua und ihre Diskretisierung*, Springer-Verlag.
[3] Schube F (2005) Numerische Simulation der Beanspruchung von Abgassystemen durch Fahrbahnunebenheiten, *MTZ, Vieweg Verlag*, **11,** pp. 860-865.
[4] Dresig H, Holzweißig F (2004) *Maschinendynamik*; Springer-Verlag, Berlin.
[5] Link M (2002) *Finite Elemente in der Statik und Dynamik*, Teubner Verlag.
[6] Willumeit, H.-P. (1998) *Modelle und Modellierungsverfahren in der Fahrzeugdynamik*, Teubner Verlag.
[7] Timoshenko S D, Young D H, Weaver W (1974) *Vibration Problems in Engineering*. 4th ed, Wiley, New York.
[8] Brcic V (1980) *Dynamic of Structures* (in Serbian), Gradjevinska Knjiga, Beograd.

MICROMECHANICAL APPROACH TO INTEGRITY ASSESSMENT OF SURFACE DAMAGED PIPES

B. Medjo[1,a], M. Rakin[1], M. Arsić[2], Ž. Šarkoćević[3], A. Sedmak[4]

[1] Faculty of Technology and Metallurgy,
University of Belgrade, Karnegijeva 4, 11120 Belgrade, Serbia
[2] Institute for Testing of Materials - IMS,
Bulevar vojvode Mišića 43, 11000 Belgrade, Serbia
[3] High Technical School of Professional Studies
Nušićeva 6, 38227 Zvečan, Serbia
[4] Faculty of Mechanical Engineering,
University of Belgrade, Kraljice Marije 16, 11120 Belgrade, Serbia
[a] e-mail: bmedjo@tmf.bg.ac.rs

Abstract. During the service life, casing steel pipes for oil and gas drilling rigs are subjected to a corrosive atmosphere, along with high pressures and elevated temperatures. Hence, they are very susceptible to corrosion damages, often preceded by errors in design, manufacturing or mounting. The influence of corrosion defects to pipeline integrity is investigated by pressure test of a pipe with circular notches, machined in order to simulate actual defects. Micromechanical approach is applied to predict the damage development, and failure criterion is considered fulfilled when damage parameter reaches its critical value in the bottom of a notch. Several analytical expressions and numerical criterion based on von Mises stress value are used for estimation of the critical pressure in damaged pipeline, and solutions are compared with the predictions of micromechanical complete Gurson model.

1. Introduction

Pipelines are the most economical and safest way for oil and gas exploitation and transport. Decrease in strength caused by the corrosion defects is very often encountered in these structures; it can endanger the work safety and even lead to catastrophic failures. Casing steel pipes used in the oil drilling rigs are subjected to a corrosive atmosphere, with coupled effects of high pressures and elevated temperatures during the service life. Hence, they are very susceptible to material degradation, often preceded by errors in design, construction, manufacturing, mounting and exploitation.

The reliability of the oil and gas drilling rig systems is very important for continuous exploitation, as well as for environment protection. Many procedures for estimation of remaining strength of the pipes with corroded (local thin) areas have been developed, [1-8]. One of the solutions for assessment of corrosion defect influence to the pipe integrity is ASME B31G code [1]. Several other procedures are also derived from it, such as [2] (in the remainder of the text - modified ASME B31G) or RSTRENG [3]. Det Norske Veritas (DNV) published recommended practices [4] for determining corroded pipelines remaining strength under internal pressure and axial loading. FITNET procedures [5] also contain a module for estimating the remaining strength of pipelines with local corrosion damages.

Choi et al. [6] derived limit load solutions based on results of experimental and numerical analyses. Adib-Ramezani et al. [7] proposed integrity assessment of the pipes with defects under internal pressure based on a modification of SINTAP (Structural integrity assessment procedure) [9].

In this paper, a local criterion for maximum pressure in damaged casing pipe for drilling rigs, manufactured from API J55 steel, is discussed. Pressure test is conducted on a pipe segment capped at both ends. Corrosion defects were simulated by machining the circular notches, and the pipe was subjected to hydrostatic pressure to determine the spreading of plasticity in damaged areas. Local approach to fracture is applied to assess the failure criterion for damaged pipe, and the results are compared with existing solutions from the literature and a finite element stress-based criterion.

2. Experimental

2.1 Material

API J55 steel is used for fabricating the examined seam casing pipe; yield strength 380 MPa, tensile strength 562 Mpa (more data about the material is given in [10]). Tensile properties are determined on round tensile (RT) specimens taken from the examined casing pipe. Figure 1 shows the strain state on the surface of the specimen obtained by stereometric measurement system Gom/Aramis [11] with two cameras and the software for data processing. This system enables determination of strain field on the surface of a structure, and a comparison with finite element solution is also given in Figure 1 (neck formation is marked by circles). Figure 2 shows the dependence of force on elongation; elongation is obtained by stereometric measurement.

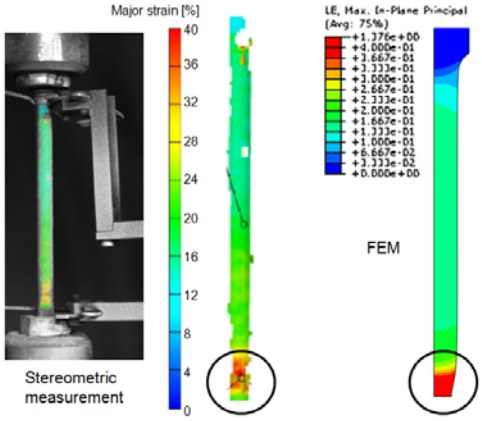

Figure 1. Strain fields for RT specimen obtained by stereometric measurement system and finite element method

Having in mind that damage is modelled in this work using a micromechanical model, microstructural observation is conducted on samples cut from the pipe. This examination indicated presence of oxides, silicates and complex oxide inclusions. Two micro-

photographs with larger clusters/groups of inclusions are given in Figure 3. Microstructural parameters (Table 1) are determined by quantitative microstructural analysis.

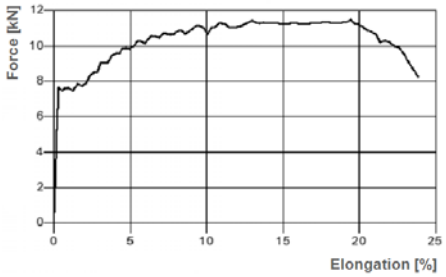

Figure 2. Load – elongation curve

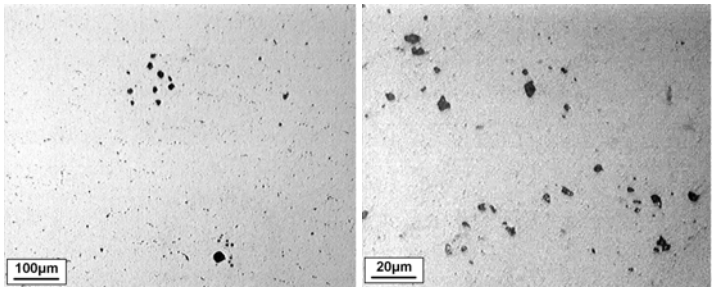

Figure 3. Micro-photographs of inclusions.

Table 1. Microstructural parameters.

Material	f [%]	λ [µm]
API J55 steel	2.7648	69.39

2.2 Pipe pressure testing

Pressure test is conducted on a part of the casing pipe capped at both ends, with nominal dimensions: diameter ϕ139.7 mm, wall thickness 6.98 mm. Corrosion defects are simulated by machining circular notches at the outer surface of the pipe (Figures 4 and 5).

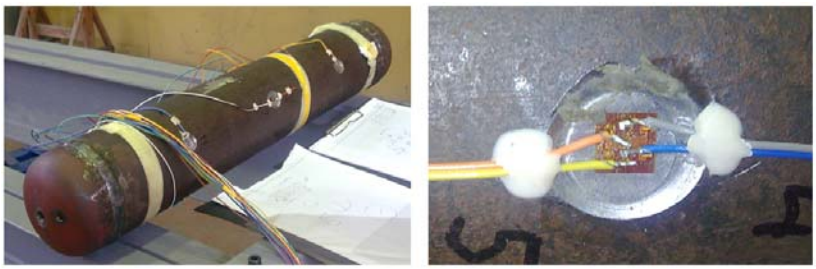

Figure 4. Pipe prepared for pressure testing with strain gauges attached at the machined defects.

Different levels of material degradation (local thin areas) are represented by varying the depth of the notches *a* (Figure 5): 5.25 mm for 75%, 3.5 mm for 50% and 1.75 mm for 25%. Strain gauges were placed at the bottom of each notch, measuring strains in circumferential (hoop) and longitudinal (axial) pipe direction.

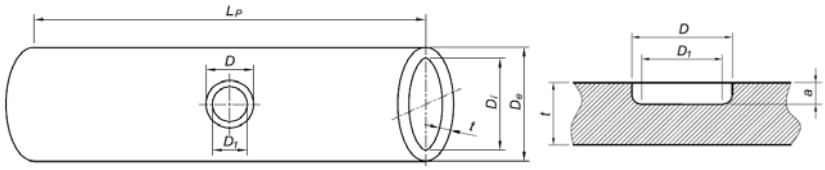

Figure 5. The pipe with a defect - main dimensions.

3. Numerical analysis

Numerical analysis of the behaviour of the pipe under internal pressure is conducted using the finite element (FE) software package Abaqus [12]. FE meshes consist of 20-node reduced integration elements, Figures 6 and 7. Gurson yield criterion [13] is used to model the material behaviour, which will be discussed in the remainder of the text. Due to the symmetry, one quarter of the pipe is modelled, with appropriate symmetry boundary conditions defined at the model boundaries. Loading is defined by prescribing the pressure at the inner surface and axial loading at one side of the FE model for simulating the effect of the dished end. The strains are measured (in the longitudinal and circumferential direction) in the middle of each defect, and in numerical analysis these values are determined in FE nearest to that location (marked in Figure 7). In addition to the circular defects corresponding to machined ones, defects with larger length are also analysed using FEM, to establish the relation between this length and load carrying capacity of the pipe.

The details of several meshes with different defect length are shown in Figure 7. Having in mind that prediction of ductile fracture initiation using local approach to fracture often exhibits mesh dependency, several modifications of the FE mesh are made for each geometry. All the changes are made in the defect ligament, because high stress and strain values are localized in this area.

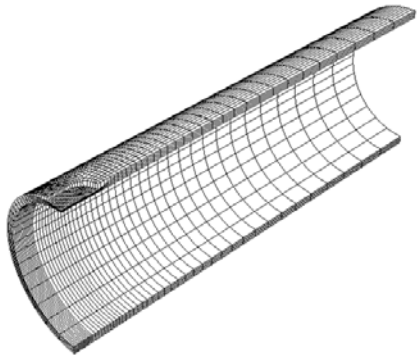

Figure 6. Finite element meshes.

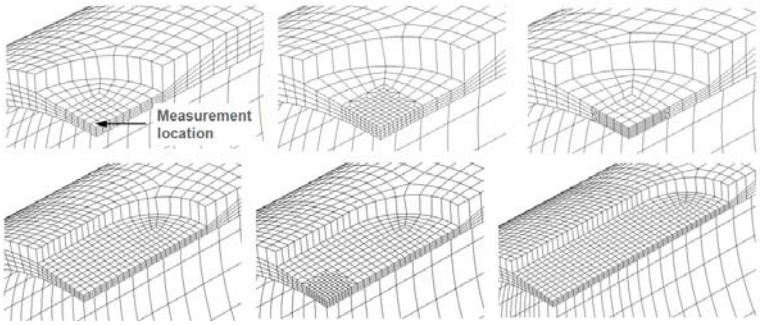

Figure 7. Finite element meshes of the defects

The results of the numerical analysis predict significantly larger strains in circumferential direction in comparison with longitudinal direction (up to 10 times), which is also measured during the experiment; results for depths 75 and 50% of the pipe wall thickness are shown in Figure 8.

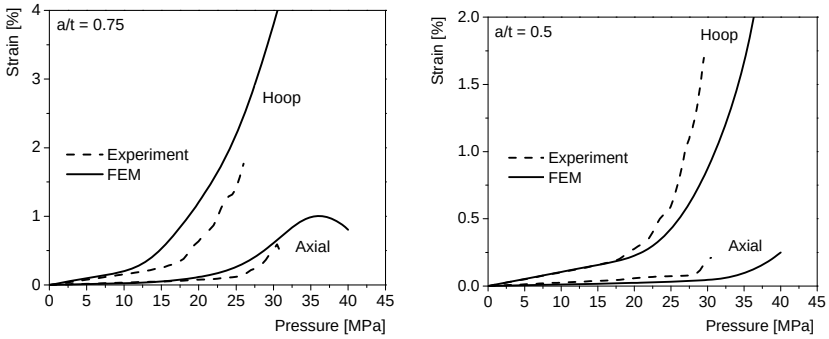

Figure 8. Comparison of strain values obtained experimentally and numerically, for defects with depth 75% (a) and 50% (b) of the pipe wall thickness.

4. Micromechanical modelling

A significant accumulation of stress and plastic strain emerges in the bottom of a defect, which leads to development of ductile damage in this area. Gurson yield criterion (with damage parameter porosity or void volume fraction) is used for damage quantification in this work. The expression for plastic potential [13 - 15] is:

$$\phi = \frac{3S_{ij}S_{ij}}{2\sigma^2} + 2q_1 f^* \cosh\left(\frac{3q_2\sigma_m}{2\sigma}\right) - \left[1 + \left(q_1 f^*\right)^2\right] = 0 \qquad (1)$$

where σ denotes the flow stress of the material matrix, σ_m is the mean stress and S_{ij} is the stress deviator. Constitutive parameters q_1 and q_2 were introduced by Tvergaard [14] to improve the predictions of the Gurson model and f^* is the damage function [15]:

$$f^* = \begin{cases} f & \text{for } f \le f_c \\ f_c + K(f - f_c) & \text{for } f > f_c \end{cases} \tag{2}$$

where f_c is the critical value of f, at the moment when the void coalescence begins.

In the initial stage of ductile fracture of steel, the voids nucleate mostly around non-metallic inclusions. Hence the initial porosity f_0 is here assumed to be equal to the volume fraction of non-metallic inclusions f_v, Table 2. During the increase of loading, two processes contribute to the increase of void volume fraction; growth of the existing voids and nucleation of new ones:

$$\dot{f} = \dot{f}_{nucleation} + \dot{f}_{growth} = A\dot{\varepsilon}^p_{eq} + (1-f)\dot{\varepsilon}^p_{ii} \tag{3}$$

where A is the void nucleation rate, $\dot{\varepsilon}^p_{eq}$ is equivalent plastic strain rate and $\dot{\varepsilon}^p_{eq}$ is the plastic part of the strain rate tensor.

Zhang et al [16] applied the Thomason's void coalescence criterion (based on the plastic limit load [17]) to the GTN model, obtaining the Complete Gurson Model - CGM. The criterion for the beginning of the void coalescence is:

$$\frac{\sigma_1}{\sigma} > \left(\alpha\left(\frac{1}{r}-1\right)+\frac{\beta}{\sqrt{r}}\right)\left(1-\pi r^2\right), \qquad r = \sqrt[3]{\frac{3f}{4\pi}e^{\varepsilon_1+\varepsilon_2+\varepsilon_3}} \Bigg/ \left(\frac{\sqrt{e^{\varepsilon_2+\varepsilon_3}}}{2}\right), \tag{4}$$

where σ_1 is maximum principal stress, ε_1, ε_2, ε_3 are principal strains, r is void space ratio, α and β are constants fitted by Thomason ($\alpha = 0.1$ and $\beta = 1.2$); Zhang et al [16] use a linear dependence of α on hardening exponent n, which is applied in the CGM.

Unlike the GTN model, the critical void volume fraction f_c does not have to be an input for calculation in CGM, but a variable that is calculated during the analysis. This value, corresponding to ductile fracture initiation, is taken as the pipe failure criterion in this work; CGM is applied through Abaqus UMAT subroutine created by Zhang, based on [16]. The value of f is monitored in the element nearest to the middle of the defect. When it reaches the critical value f_c, the pipe failure is predicted and the corresponding maximum pressure is determined.

Figure 9 shows distribution of damage parameter (porosity f) at the moment when local failure criterion is reached, and it can be seen that high values of f are localised in the middle of the defect.

In the literature [18 - 20], GTN model has been previously used for analysis of load carrying capacity of pipes with crack-like flaws. The present work aims at extending this approach to pipes containing blunt surface defects, like those caused by local corrosion. Local approach to fracture was previously applied for similar purpose in [21], but the procedure included so-called uncoupled modelling - calculating the damage parameter during post-processing procedure, without its influence on the yield criterion.

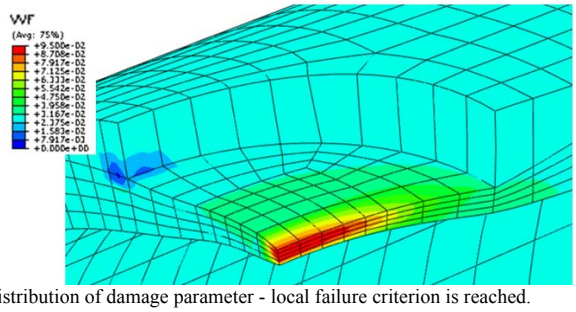

Figure 9. Distribution of damage parameter - local failure criterion is reached.

5. Failure criteria comparison

In addition to the micromechanical criterion, several solutions from literature are applied for calculation of the maximum pressure of the analysed pipe: ASME B31G code [1], modified ASME B31G [2, 3] and the solution of Choi et al. [6] (in the remainder of the paper - Choi's solution/equation). Corresponding expressions are given in Table 2.

Table 2. Expressions used for calculation of maximum pressure

ASME B31G		
$L \le \sqrt{20 \cdot D_e t}$	$p_{max} = 1.1 \cdot \sigma_Y \frac{2t}{D_e}\left[\frac{1-\frac{2a}{3t}}{1-\frac{2a}{3t}\cdot\frac{1}{M}}\right]$	$M = \sqrt{1+0.8\frac{L^2}{D_e t}}$
$L > \sqrt{20 \cdot D_e t}$	$p_{max} = 1.1 \cdot \sigma_Y T \frac{2t}{D_e}\left(1-\frac{a}{t}\right)$	$M = \infty$
Modified ASME B31G		
$L \le \sqrt{50 \cdot D_e t}$	$p_{max} = \left(1.1 \cdot \sigma_Y + 69 \cdot 10^6\right)\frac{2t}{D_e}\left(\frac{1-0.85\frac{a}{t}}{1-0.85\frac{a}{t}\cdot\frac{1}{M}}\right)$	$M = \sqrt{1+0.6275\frac{L^2}{D_e \cdot t}-0.003375\left(\frac{L^2}{D_e t}\right)^2}$
$L > \sqrt{50 \cdot D_e t}$		$M = 3.3+0.032\frac{L^2}{D_e t}$
Choi's solution		
$L < 6\sqrt{Rt}$	$p_{max} = 0.9 \cdot \sigma_m \frac{2t}{D_i}\left[C_2\left(\frac{L}{\sqrt{Rt}}\right)^2 + C_1\left(\frac{L}{\sqrt{Rt}}\right)+C_0\right]$	$C_2 = 0.1163\left(\frac{a}{t}\right)^2 - 0.1053\left(\frac{a}{t}\right)+0.0292$ $C_1 = -0.6913\left(\frac{a}{t}\right)^2 + 0.4548\left(\frac{a}{t}\right)-0.1447$ $C_0 = 0.06\left(\frac{a}{t}\right)^2 - 0.1035\left(\frac{a}{t}\right)+1.0$
$L \ge 6\sqrt{Rt}$	$p_{max} = \sigma_m \frac{2t}{D_i}\left[C_1\left(\frac{L}{\sqrt{Rt}}\right)+C_0\right]$	$C_1 = 0.0071\left(\frac{a}{t}\right)-0.0126$ $C_0 = -0.9847\left(\frac{a}{t}\right)+1.1101$

In Table 2, a and L are defect depth and length, M is geometry correction factor, while C_j (j = 0..2) are coefficients in Choi's equation. Geometry of the pipe is defined in Figure 5; D_e and D_i represent the external and internal diameter of the pipe ($D_i = D_e - 2t$), while mean pipe radius is $R = (D_e + D_i)/4$.

Figure 10 shows the dependence of maximum pressure in a damaged pipeline on defect length for damage level 75%, obtained using expressions from Table 2, FE stress-based solution and CGM solution. FE stress-based failure criterion is considered to be fulfilled when von Mises stress value reaches the reference stress through the entire ligament; reference stress is chosen at 85 % of the ultimate tensile strength, as moderately conservative solution [22]. Two points for CGM at a damage length represent the limit values obtained using different element size (Figure 7) and formulation, as well as different load increments.

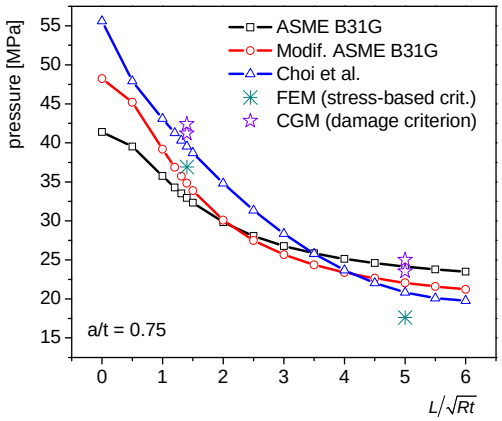

Figure 10. Comparison of the maximum pressure for defects with depth 75% of the pipe wall thickness.

Local approach (model based on the Gurson yield criterion) can predict the trend of decrease in maximum pressure with increase of defect length and depth. Having in mind that it is strain-based and that it includes damage development in material, it is physically suitable for the materials often used for pipe manufacturing. Namely, such materials exhibit ductile behaviour in the working conditions (except for those operating at low temperatures) and their failure is usually accompanied with plastic deformations. Local approach also prevents another problem with standard stress-based criteria, which is variable coefficient multiplying the ultimate tensile strength for determination of failure criterion [7]. This coefficient, often designated as η, can have values from 0.8 to 1.0, depending on the material (its stress-strain curve, etc.) and geometry of the pipe/defect. As mentioned previously, in the Figure 10 this value is 0.85.

6. Conclusions

The results presented and discussed in this paper concerning the local failure criterion for assessment of the remaining strength of damaged pipes manufactured from API J55 steel can be summarised as follows:

- Ductile fracture initiation can be used as the failure criterion for examined structures, especially bearing in mind the exploitation conditions and materials used for their manufacturing.
- Unlike other numerical criteria for pipe integrity assessment, mainly stress-based, micromechanical modelling includes analysis of damage that inevitably emerges prior to failure. Also, plastic deformation development, characteristic for ductile fracture, is taken into account this way, which is important because it influences the damage initiation and development.
- An advantage of the local approach is lack of a need for estimation of the reference stress - in the literature varying between 80 and 100 % of the ultimate tensile strength.
- The influence of FE mesh on the applied micromechanical criterion for pipe failure exists, but it is not significant.

Acknowledgement. The authors acknowledge the support from the Serbian Ministry of Science under the projects OI 174004 and TR 35002. The authors would also like to thank Z.L. Zhang for the CGM user subroutine and I. Cvijović-Alagić for help in microstructural analysis.

References

[1] American Society of Mechanical Engineers (1991) *ASME B31G: Manual for Determining the Remaining Strength of Corroded Pipelines*, New York.
[2] Kiefner J, Vieth P (1989) *A modified Criterion for Evaluating the Strength of Corroded Pipe - Final Report on Project PR 3-805 to the Pipeline Supervisory Committee of the American Gas Association*, Ohio: Battelle.
[3] Kiefner J, Vieth P (1990) Evaluating Pipe 1: New Method Corrects Criterion for Evaluating Corroded Pipe, *Oil & Gas Journal*, **88**, pp. 56-59.
[4] Det Norske Veritas (2004) *DNV RP-F101: Corroded Pipelines - Recommended Practice*, Hovik.
[5] FITNET: European Fitness-for-Service Network, http://www.eurofitnet.org
[6] Choi J B, Goo B K, Kim J C, Kim Y J, Kim W S (2003) Development of Limit Load Solutions for Corroded Gas Pipelines, *International Journal of Pressure Vessels and Piping*, **80**, pp. 121-128.
[7] Adib-Ramezani H, Jeong J, Pluvinage G (2006) Structural Integrity Evaluation of X52 Gas Pipes Subjected to External Corrosion Defects Using the SINTAP Procedure, *International Journal of Pressure Vessels and Piping*, **83**, pp. 420-432.
[8] Chiodo M, Ruggieri C (2009) Failure Assessments of Corroded Pipelines with Axial Defects Using Stress-Based Criteria: Numerical Studies and Verification Analyses, *International Journal of Pressure Vessels and Piping*, **86**, pp 164-176.
[9] *SINTAP: Structural Integrity Assessment Procedure - Final Report EU project BE95-1462* (1999) Brussels
[10] Šarkoćević Ž, Arsić M, Medjo B, Kozak D, Rakin M, Burzić Z, Sedmak A (2009) Damage Level Estimate of API J55 Steel for Welded Seam Casing Pipes, *Strojarstvo: Journal for Theory and Application of Mechanical Engineering*, **51**, pp. 303-311.
[11] Aramis GOM GmbH, www.gom.com
[12] Abaqus FEM software package, www.simulia.com
[13] Gurson A L (1977) Continuum Theory of Ductile Rupture by Void Nucleation and Growth: Part I - Yield Criteria and Flow Rules for Porous Ductile Media, *Journal of Engineering Materials and Technology ASME*, **99**, pp. 2-15.

[14] Tvergaard V (1981) Influence of Voids on Shear Band Instabilities under Plane Strain Conditions, *International Journal of Fracture*, **17**, pp 389-407.
[15] Tvergaard V, Needleman A (1984) Analysis of the Cup-Cone Fracture in a Round Tensile Bar, *Acta Metallurgica*, **32**, pp 157-169.
[16] Zhang Z L, Thaulow C, Odegard J (2000) A Complete Gurson Model Approach for Ductile Fracture, *Engineering Fracture Mechanics*, **67**, pp. 155-168.
[17] Thomason P F (1990) *Ductile Fracture of Metals*, Pergamon Press, Oxford.
[18] Bezensek B, Miyazaki K (2009) Alignment Criteria for Through-Wall Flaws in Plates and Pipes, *Proceedings of the 2009 ASME Pressure Vessels and Piping Division Conference*, Prague, published on CD.
[19] Dotta F, Ruggieri C (2004) Structural Integrity Assessments of High Pressure Pipelines with Axial Flaws Using a Micromechanics Model, *International Journal of Pressure Vessels and Piping*, **81**, pp. 761-770.
[20] Saxena S, Ramakrishnan N, Chouhan J S (2010) Establishing Methodology to Predict Fracture Behaviour of Piping Components by Numerically Predicting Specimen Fracture Data Using Tensile Specimen Test, *Engineering Fracture Mechanics*, **77**, pp. 1058-1072.
[21] Oh C K, Kim Y J, Baek J H, Kim Y P, Kim W S (2007) A Phenomenological Model of Ductile Fracture for API X65 Steel, *International Journal of Pressure Vessels and Piping*, **84**, pp. 512-525.
[22] Arsić M, Rakin M, Šarkoćević Ž, Medjo B, Burzić Z, Sedmak A (2011) Remaining Strength of Damaged API J55 Steel Casing Pipes, *submitted to International Journal of Pressure Vessels and Piping*

DETERMINATION OF OPTIMUM DIMENSION OF VARIABLE SHAPE LATTICE-COLUMNS FOR BUCKLING

Radomir Mijailović

[1] Faculty of Transport and Traffic Engineering
The University of Belgrade, Vojvode Stepe 305, 11000 Belgrade, Serbia
e-mail: radomirm@beotel.rs

Abstract. Determining the optimal construction dimensions represents one of the major tasks in the process of construction. Their determination importantly influences the reduction of construction overall costs. By this fact, the construction solution becomes competitive on the market. Numerous authors have dealt with the construction optimization using models of different approximation levels. Different types of constructions can be subject to optimization. Constraint functions were also different depending on the construction's operation characteristics. The optimization of the lattice column against buckling was performed in paper [1]. As one of the further research objectives in the previous paper it has been recommended to analyze new models about the optimization of lattice constructions for buckling. This paper's objective is to obtain functions that determine realistic optimal parameters of the variable shape lattice-columns. These functions should be straightforward for practical implementation. The adopted model should facilitate to the constructor to obtain the results allowing him to choose from the profiles available on the market. Total mass of the columns has been selected as the objective function. Criterions of general buckling of the lattice column, local buckling of the chord and local buckling of the bracing diagonal are used as the constraint functions. Numerical examples are performed by usage of the obtained theoretical solutions.

Keywords: optimization, lattice, variable shape, column, buckling.

1. Introduction

Determining the optimal construction dimensions represents one of the major tasks in the process of construction. Their determination importantly influences the reduction of construction overall costs. By this fact, the construction solution becomes competitive on the market. The analysis of the cost structure of a metal construction, carried out by Farkas [5], has shown that the price is primarily influenced by the price of the material (30-73)%, while the other costs are lower: manufacture (16-22)%, assembling (5-20)%, transportation (3-7)%, design (2-3)%. The selection of optimal shape and optimum parameters of metal construction reduce the consumption of the material and its costs [1, 5, 8, 12, 18]. Numerous authors have dealt with the construction optimization using models of different approximation levels. Different types of constructions can be subject to optimization. Constraint functions were also different depending on the construction's operation characteristics. The problem of construction optimization, using different methods, objective and constraint functions, was studied by several authors [1...18].

Authors [12] determined optimal parameters of trapezoid cross section of tower crane bracing boom. The established model included practical data that the overall dimensions of boom cross-section are unvarying along the boom. Based on the analysis that was carried out, the recommendations are given regarding the application of trapezoid, triangular and rectangular cross-sections of the bracing constructions are given.

As one of the further research objectives in the paper [12] it has been recommended to analyze the influence of buckling on optimal dimensions of bracing constructions. This problem was resolved in the paper [13]. Bracing column has been selected as a representative construction where the problem of buckling is often present. This paper's objective is to obtain functions that determine realistic optimal parameters of the selected construction (height of the parallel chords, cross-sectional areas of the chord and bracing and area moments of inertia of the chord and bracing). The model included assumption that the overall dimensions of construction cross-section are unvarying along the construction.

As one of the further research objectives in the paper [13] it has been recommended to analyze new models about the optimization of lattice constructions for buckling. This paper's objective is to obtain functions that determine realistic optimal parameters of the variable shape lattice-columns. These functions should be straightforward for practical implementation. The adopted model should facilitate to the constructor to obtain the results allowing him to choose from the profiles available on the market.

2. Defining of the optimization task

Bracing constructions have important applications in practice, especially in case of constructions with larger overall dimensions, where larger carrying capacity and minimal weight are required.

The cross section of bracing construction (Fig. 1) consists of chords (pos. 1) and bracing (pos. 2a, 2b, 3). The chords are usually made of pipes with circular, square or rectangular cross-section. Bracing are welded to the chords.

Bracing are composed of the diagonals (pos. 2) and struts (pos. 3). Struts (pos. 3) perpendicular to chords are loaded by axial force that has smaller values than diagonal (pos. 2) axial force. Optimal struts cross-sectional area could be smaller than the optimal diagonal cross-sectional area. The struts' (pos. 3) task is to decrease the buckling length of the chords. Cross-sectional areas of bracing (pos. 2 and 3) are manufactured from profiles witch equal cross-sectional area and area moment of inertia in practice.

In this paper, the area moment of inertia and cross-section areas are analyzed in view of correlation for various profiles (cross-sections) usually found in practice. Results of the analysis show that the best results can be obtained for the following functional dependence [13]:

$$I_y = \psi \cdot A^2 \;\rightarrow\; I_{y1} = \psi_1 \cdot A_1^2,\; I_{y2} = \psi_2 \cdot A_2^2 . \tag{1}$$

The numerical values of the coefficients ψ_1 and ψ_2 can be found in paper [13].

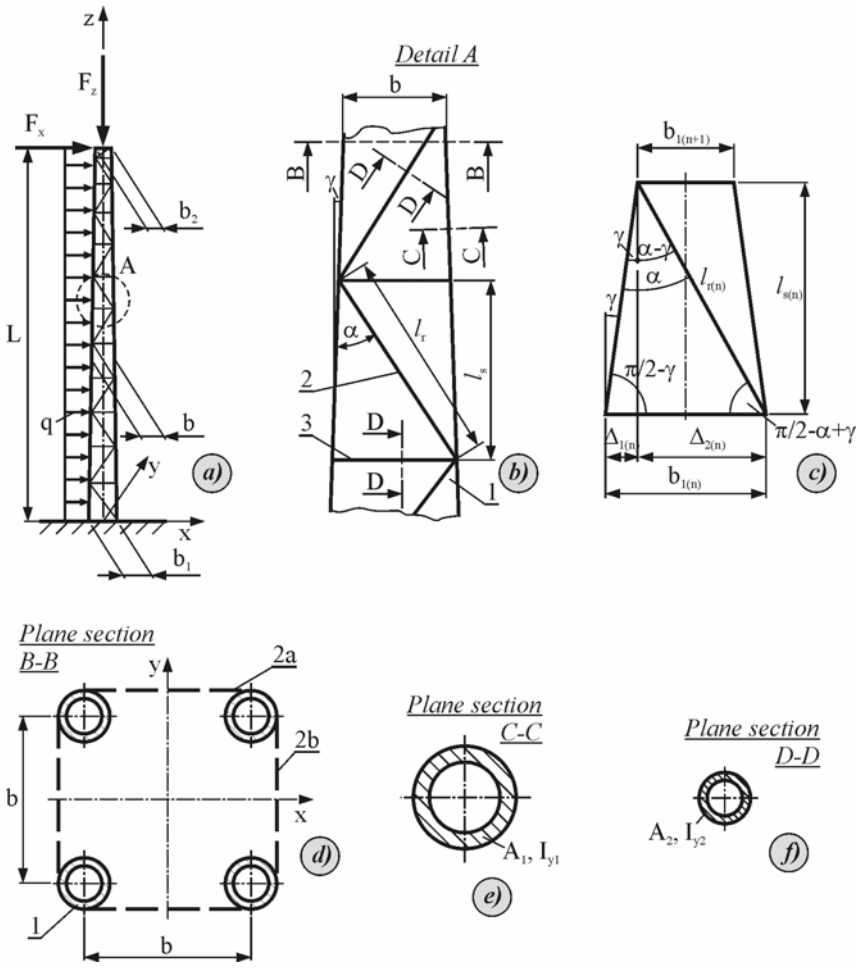

Fig. 1. Bracing column
b – height of the parallel chords (b_1 – bottom of the construction, b_2 – top of the construction); A_1 – cross-sectional area of one chord; I_{y1} – area moment of inertia of one chord; A_2 – cross-sectional area of one bracing; I_{y2} – area moment of inertia of one bracing

In the paper will be define next optimum dimensions of square cross-section in bracing column (Fig. 1): b_1, b_2, A_1 and A_2.

3. Objective function

As it was mentioned before, the price of the material, hence, material consumption has the main influence in the overall price of metal construction. Hence, minimization of total mass of the construction has been selected as the objective function:

$$F \equiv m = \rho \cdot V \,. \tag{2}$$

where
– ρ – is density of the material,
– V – volume of the bracing construction.

Volume of the bracing construction is equal to the sum of chords volume (V_p), volume of bracing (V_r) and volume of other elements (V_o):

$$V = V_p + V_r + V_o \,. \tag{3}$$

The volume of the chords is determined by the following expression:

$$V_p = 4 \cdot A_1 \cdot \frac{L}{\cos\gamma} \,. \tag{4}$$

Applying the small-angle approximation

$$\cos\gamma \approx 1 \,;\ \sin\gamma \approx tg\gamma \approx \gamma \,, \tag{5}$$

the volume of the chords (4) can be rewritten in the form:

$$V_p = 4 \cdot A_1 \cdot L \,. \tag{6}$$

The volume of the bracing is in the form:

$$V_r = 4 \cdot A_2 \cdot \sum_{i=1}^{n_s} b_{1(i)} + l_{r(i)} \,. \tag{7}$$

where
– l_r – length of diagonal (Fig. 1b),
– l_s – length of segments (Fig. 1b),
– n_s – number of segments.

The angle γ may be found by the following expression:

$$tg\gamma = \frac{\frac{b_1 - b_2}{2}}{L} = \frac{b_1 - b_2}{2 \cdot L} \xrightarrow{(5)} \gamma = \frac{b_1 - b_2}{2 \cdot L} \,. \tag{8}$$

Height of the parallel chords on the bottom of segment ″n″ ($b_{1(n)}$ – Fig. 1c) is determined by next expression:

$$b_{1(n)} = \Delta_{1(n)} + \Delta_{2(n)} \,, \tag{9}$$

where

$$\Delta_{1(n)} = \frac{l_{s(n)}}{tg(\frac{\pi}{2} - \gamma)}. \tag{10}$$

$$\Delta_{2(n)} = \frac{l_{s(n)}}{tg[\frac{\pi}{2} - (\alpha - \gamma)]}. \tag{11}$$

Applying the small-angle approximation (5) equations (10) and (11) can be rewritten in the form

$$\Delta_{1(n)} = \gamma \cdot l_{s(n)}, \tag{12}$$

$$\Delta_{2(n)} = l_{s(n)} \cdot \frac{tg\alpha - \gamma}{1 + \gamma \cdot tg\alpha}, \tag{13}$$

and equation (9) can be rewritten in the form:

$$b_{1(n)} = l_{s(n)} \cdot \frac{tg\alpha}{1 + \gamma \cdot tg\alpha}. \tag{14}$$

By using a previous equation length of segment $''n''$ (Fig. 1b, 1c) can be written in form of:

$$l_{s(n)} = b_{1(n)} \cdot \frac{1 + \gamma \cdot tg\alpha}{tg\alpha}. \tag{15}$$

Length of diagonal of segment $''n''$ can be defined by trigonometry too:

$$l_{r(n)} = \frac{l_{s(n)}}{\cos(\alpha - \gamma)} \xrightarrow{(5,15)} l_{r(n)} = \frac{b_{1(n)}}{\cos\alpha + \gamma \cdot \sin\alpha} \cdot \frac{1 + \gamma \cdot tg\alpha}{tg\alpha}. \tag{16}$$

Height of the parallel chords on the top of segment $''n''$ is equal to height of the parallel chords on the bottom of segment $''n{+}1''$ ($b_{1(n+1)}$ – Fig. 1c). The $b_{1(n+1)}$ is determined by next expressions:

$$b_{1(n+1)} = b_{1(n)} - 2 \cdot \Delta_{1(n)} = b_{1(n)} \cdot (1 - \frac{2 \cdot \gamma}{tg\alpha}), \tag{17}$$

$$b_{1(n+1)} = b_1 \cdot (1 - \frac{2 \cdot \gamma}{tg\alpha})^n. \tag{18}$$

By application of the expression (18) the expressions (15) and (16) become in their final forms:

$$l_{s(n)} = b_1 \cdot (1 - \frac{2 \cdot \gamma}{tg\alpha})^{n-1} \cdot \frac{1 + \gamma \cdot tg\alpha}{tg\alpha}, \tag{19}$$

$$l_{r(n)} = \frac{b_1}{\cos\alpha + \gamma \cdot \sin\alpha} \cdot (1 - \frac{2 \cdot \gamma}{tg\alpha})^{n-1} \cdot \frac{1 + \gamma \cdot tg\alpha}{tg\alpha} . \quad (20)$$

Height of the parallel chords on the top of construction (Fig. 1a) by using of expression (8) can be written in form of:

$$b_2 = b_1 - 2 \cdot L \cdot \gamma . \quad (21)$$

Number of segments (n_s) determined by using the geometrical conditions that the height of the parallel chords on the top of construction (b_2) is equal to the height of the parallel chords on the top of the last segment ($b_{1(n+1)}$)

$$b_2 = b_{1(ns+1)} . \quad (22)$$

Substitution of (18) and (21) into (22) yields:

$$n_s = \frac{\ln(\frac{b_1 - 2 \cdot L \cdot \gamma}{b_1})}{\ln(1 - \frac{2 \cdot \gamma}{tg\alpha})} . \quad (23)$$

The volume of the bracing (7) by using of expressions (18) and (20) can be written in its final form:

$$V_r = 4 \cdot A_2 \cdot b_1 \cdot (1 + \frac{1}{\cos\alpha + \gamma \cdot \sin\alpha} \cdot \frac{1 + \gamma \cdot tg\alpha}{tg\alpha}) \cdot \sum_{i=1}^{n_s} (1 - \frac{2 \cdot \gamma}{tg\alpha})^{i-1} . \quad (24)$$

The volume of other elements is determined by following expression:

$$V_o = k_1 \cdot (V_p + V_r) . \quad (25)$$

The variation of coefficient value k_1 is minimal in observed cases, so they can be assumed constant [5, 12, 18].

By application of the expressions (6), (24) and (25), the volume of the bracing construction (3) obtains its final form:

$$V = 4 \cdot (1 + k_1) \cdot [A_1 \cdot L + A_2 \cdot b_1 \cdot (1 + \frac{1}{\cos\alpha + \gamma \cdot \sin\alpha} \cdot \frac{1 + \gamma \cdot tg\alpha}{tg\alpha}) \cdot \sum_{i=1}^{n_s} (1 - \frac{2 \cdot \gamma}{tg\alpha})^{i-1}] . \quad (26)$$

4. Constraint functions

Criterions of buckling are used as the constraint function:
– general buckling of the bracing column,
– local buckling of the chord,
– local buckling of the bracing diagonal.

The constraint function of general buckling of the bracing column is given by expression [13, 14]:

$$\varphi_1 = \frac{1}{\chi_{1,j}} \cdot \frac{N_1}{4 \cdot A_1} + \frac{M_{y,1}}{W_{y,uk}} - f_d \le 0 . \tag{27}$$

Axial force is determined by next expression:

$$N_1 = F_z \cdot \cos\gamma \xrightarrow{(5)} N_1 \approx F_z . \tag{28}$$

Moments of flexion for axes y is in given by expression:

$$M_y = F_x \cdot L + \frac{q \cdot L^2}{2} . \tag{29}$$

Moment of inertia and resistance moment on the bottom of the bracing column are in given by expressions:

$$I_{y,uk} = A_1 \cdot b_1^2 , \tag{30}$$

$$W_{y,uk} = 2 \cdot A_1 \cdot b_1 . \tag{31}$$

Limiting stress can be determined by follow expression:

$$f_d = \frac{f_y}{\gamma_m} , \tag{32}$$

where
– f_y – yield stress,
– γ_m – material safety factor.

The reduction factor χ for the buckling curves (A, B, C, D) is in given by expression [13]:

$$\chi_{i,j} = \frac{1}{u_{i,j} + v_{i,j} \cdot \bar{\lambda}_i^2} . \tag{33}$$

where
– i – criteria of buckling (for this case i=1,2,3)
– j – buckling curves (j=A, B, C, D)
– $u_A = 0.93430613$, $v_A = 0.66790141$,
– $u_B = 0.95183782$, $v_B = 0.79943067$,
– $u_C = 0.96585452$, $v_C = 0.93542113$,
– $u_D = 0.981721$, $v_D = 1.1634394$.

The reduction factor $\chi_{1,j}$ for the general buckling of the bracing column using the equation (33) can be rewritten as follows:

$$\chi_{1,j} = \frac{1}{u_{1,j} + v_{1,j} \cdot \bar{\lambda}_1^2}. \tag{34}$$

Least radius of gyration is in the form:

$$i_1 = \sqrt{\frac{I_{y,uk}}{4 \cdot A_1}} \xrightarrow{(30)} i_1 = \frac{b_1}{2}. \tag{35}$$

Ideal slenderness ratio can be defined by the expression [13]:

$$\lambda_{1i} = \sqrt{\lambda_1^2 + 8 \cdot K \cdot \frac{A_1}{A_2}}. \tag{36}$$

The parameter K is a function of the angle α (Fig. 1b). Values of the parameter K can be found in papers [9, 14].

Slenderness ratio can be determinate by the equation:

$$\lambda_1 = \frac{\beta \cdot L}{i_1}. \tag{37}$$

Column effective length factor (β) depends on the conditions of end support of the column and ratio of the moments of inertia on the top and bottom of the bracing column:

$$\beta = \beta_1 \cdot \beta_2. \tag{38}$$

The factor (β_1) depends on the conditions of end support of the column. A bracing column is modeled as cantilever. In this case factor β_1 is:

$$\beta_1 = 2. \tag{39}$$

The factor (β_2) is a function of ratio of the moments of inertia on the top and bottom of the bracing column:

$$\beta_2 = f\left(\frac{I_{y,uk,2}}{I_{y,uk,1}}\right) \xrightarrow{(30)} \beta_2 = f\left(\frac{b_2^2}{b_1^2}\right). \tag{40}$$

The factor (β_2) was approximated based on catalogue data [14] by correlation analysis:

$$\beta_2 = w_1 + w_2 \cdot \left(\frac{b_2}{b_1}\right)^{w_3}, \tag{41}$$

where

– $w_1 = -3.505845$, $w_2 = 4.502242$, $w_3 = -0.11794$,

– $k = 0.9999$ – correlation coefficient.

Substitution of (39) and (41) into (38) yields column effective length factor:

$$\beta = 2 \cdot [w_1 + w_2 \cdot (\frac{b_2}{b_1})^{w_3}] . \quad (42)$$

Slenderness ratio can be determined by substitution of (35) and (42) into (37):

$$\lambda_1 = \frac{4 \cdot L}{b_1} \cdot [w_1 + w_2 \cdot (\frac{b_2}{b_1})^{w_3}] . \quad (43)$$

The relative slenderness ratio is determined by next expression:

$$\bar{\lambda}_1 = \frac{\lambda_{1i}}{\lambda_v} . \quad (44)$$

Slenderness ratio with the yield stress is in given by expression:

$$\lambda_v = \pi \cdot \sqrt{\frac{E}{f_y}} . \quad (45)$$

where E denotes the modulus of elasticity.

The relative slenderness ratio (44) by using of expression (36), (43) can be written in form of:

$$\bar{\lambda}_1 = \frac{2}{\lambda_v} \sqrt{2 \cdot \{\frac{2 \cdot L^2}{b_1^2} \cdot [w_1^2 + 2 \cdot w_1 \cdot w_2 \cdot (\frac{b_2}{b_1})^{w_3} + w_2^2 \cdot (\frac{b_2}{b_1})^{2 \cdot w_3}] + K \cdot \frac{A_1}{A_2}\}} . \quad (46)$$

By applying expressions (28), (31), (34) and (46) the constraint function of general buckling of the bracing column (27) obtains its final form:

$$\varphi_1 = \frac{F_z}{4 \cdot A_1} \cdot \{u_{1,j} + \frac{8 \cdot v_{1,j}}{\lambda_v^2} \cdot \{\frac{2 \cdot L^2}{b_1^2} \cdot [w_1^2 + 2 \cdot w_1 \cdot w_2 \cdot \left(\frac{b_2}{b_1}\right)^{w_3} + w_2^2 \cdot \left(\frac{b_2}{b_1}\right)^{2 \cdot w_3}] + K \cdot \frac{A_1}{A_2}\}\} + \frac{M_y}{2 \cdot A_1 \cdot b_1} - f_d \le 0 . \quad (47)$$

The constraint function of local buckling of the chord is in given by expression:

$$\varphi_2 = \frac{1}{\chi_{2,j}} \cdot \frac{N_2}{A_1} - f_d \le 0 . \quad (48)$$

Axial force, supposed to act on the cross-section center of the chord, is in given by expression:

$$N_2 = \frac{F_z}{4} + \frac{M_y}{2 \cdot b} = \frac{F_z \cdot b + 2 \cdot M_y}{4 \cdot b} , \quad (49)$$

The reduction factor $\chi_{2,j}$ for the local buckling of the chord using the equation (33) can be written by the following equation:

$$\chi_{2,j} = \frac{1}{u_{1,j} + v_{1,j} \cdot \bar{\lambda}_2^2} . \tag{50}$$

Least radius of gyration is in the form:

$$i_2 = \sqrt{\frac{I_{y1}}{A_1}} \xrightarrow{(1)} i_2 = \sqrt{\psi_1 \cdot A_1} . \tag{51}$$

The slenderness ratio for a fixed ends beam and effective buckling length of chords $0.9 \cdot l_s$ [15] can be written in form of:

$$\lambda_2 = \frac{0.9 \cdot l_{s(1)}}{i_2} \xrightarrow{(52)} \lambda_2 = \frac{0.9 \cdot l_{s(1)}}{\sqrt{\psi_1 \cdot A_1}} . \tag{52}$$

The relative slenderness ratio is determined by next expression:

$$\bar{\lambda}_2 = \frac{\lambda_2}{\lambda_v} \xrightarrow{(53)} \bar{\lambda}_2 = \frac{1}{\lambda_v} \cdot \frac{0.9 \cdot l_{s(1)}}{\sqrt{\psi_1 \cdot A_1}} . \tag{53}$$

By application of the expressions (19) and (53) the reduction factor $\chi_{2,j}$ (50) finally becomes:

$$\frac{1}{\chi_{2,j}} = u_{1,j} + \frac{v_{1,j}}{\lambda_v^2} \cdot \frac{0.81 \cdot b_1^2}{\psi_1 \cdot A_1} \cdot \frac{(1 + \gamma \cdot tg\alpha)^2}{(tg\alpha)^2} . \tag{54}$$

Substitution of expressions (49) and (54) into Eq. (48) yields:

$$\varphi_2 = \frac{F_z \cdot b + 2 \cdot M_y}{4 \cdot b \cdot A_1} \cdot [u_{1,j} + \frac{v_{1,j}}{\lambda_v^2} \cdot \frac{0.81 \cdot b_1^2}{\psi_1 \cdot A_1} \cdot \frac{(1 + \gamma \cdot tg\alpha)^2}{(tg\alpha)^2}] - f_d \le 0 . \tag{55}$$

The constraint function of local buckling of the bracing diagonal is in given by expression:

$$\varphi_3 = \frac{1}{\chi_{3,j}} \cdot \frac{F_d}{A_2} - f_d \le 0 . \tag{56}$$

Axial force supposed to act on the cross-section center of the bracing diagonal is given by expression:

$$F_d = \frac{F_x + q \cdot L}{2 \cdot \sin(\alpha - \gamma)} \xrightarrow{(5)} F_d = \frac{F_x + q \cdot L}{2 \cdot (\sin\alpha - \gamma \cdot \cos\alpha)} . \tag{57}$$

The reduction factor for the local buckling of the bracing diagonal using the equation (33) can be written in the following form:

$$\chi_{3,j} = \frac{1}{u_{3,j} + v_{3,j} \cdot \bar{\lambda}_3^2} . \tag{58}$$

Least radius of gyration is in given by expression:

$$i_3 = \sqrt{\frac{I_{y2}}{A_2}} \xrightarrow{(1)} i_3 = \sqrt{\psi_2 \cdot A_2}\,. \tag{59}$$

The slenderness ratio for a fixed ends beam and effective buckling length of bracings $0.75 \cdot l_r$ [15] is determined by next expression:

$$\lambda_3 = \frac{0.75 \cdot l_{r(1)}}{i_3} \xrightarrow{(16,66)} \lambda_3 = \frac{0.75 \cdot b_1 \cdot (1 + \gamma \cdot tg\alpha)}{\sqrt{\psi_2 \cdot A_2} \cdot tg\alpha \cdot (\cos\alpha + \gamma \cdot \sin\alpha)}\,. \tag{60}$$

The relative slenderness ratio is determined by next expression:

$$\bar{\lambda}_3 = \frac{\lambda_3}{\lambda_v}\,. \tag{61}$$

Substitution of expressions (60) and (61) into Eq. (58) yields:

$$\frac{1}{\chi_{3,j}} = u_{3,j} + \frac{0.5625 \cdot v_{3,j} \cdot b_1^2 \cdot (1 + \gamma \cdot tg\alpha)^2}{\lambda_v^2 \cdot \psi_2 \cdot A_2 \cdot (tg\alpha)^2 \cdot (\cos\alpha + \gamma \cdot \sin\alpha)^2}\,. \tag{62}$$

By application of the expressions (57) and (62) the constraint function of local buckling of the bracing diagonal (56) becomes finally:

$$\begin{aligned} \varphi_3 &= \frac{F_x + q \cdot L}{2 \cdot A_2 \cdot (\sin\alpha - \gamma \cdot \cos\alpha)} \cdot \\ &\cdot [u_{3,j} + \frac{0.5625 \cdot v_{3,j} \cdot b_1^2 \cdot (1 + \gamma \cdot tg\alpha)^2}{\lambda_v^2 \cdot \psi_2 \cdot A_2 \cdot (tg\alpha)^2 \cdot (\cos\alpha + \gamma \cdot \sin\alpha)^2}] - f_d \le 0. \end{aligned} \tag{63}$$

I concluded that analytical solution of minimization of the objective function (26) could not be determined for model with previous constraint functions (47), (55) and (63). For this reason, the optimal parameters should be numerically determined.

5. Numerical Example and Analysis of Results

The verification of theoretical results is carried out on a numerical example for a lattice column with the following data: k_1=0.05, L=30 m, α=45^O, f_y=235 N/mm^2, ψ=1.504 (circular cross section).

The graphs of optimum parameters in the function of transverse force (F_x) for the lattice-columns with the overall dimensions of construction cross-section are unvarying along the construction were taken from paper [13].

By analyzing graphs (Fig. 2a) it can be concluded that the optimal height of the parallel chords on the bottom of construction (b_1(II)) for unvarying shape lattice-columns is greater than the optimal height of the parallel chords for variable shape (b_1(I)). Based on the analysis of Fig. 2 it may concluded that the optimal heights of the parallel chords on the

bottom and the top of construction have the same values in case of smaller values of the transverse force (F_x).

On the other hand, optimal cross-sectional area of one chord (A_1(I)) for variable shape lattice-columns is greater than the optimal cross-sectional area of one chord (A_1(II)) for unvarying shape.

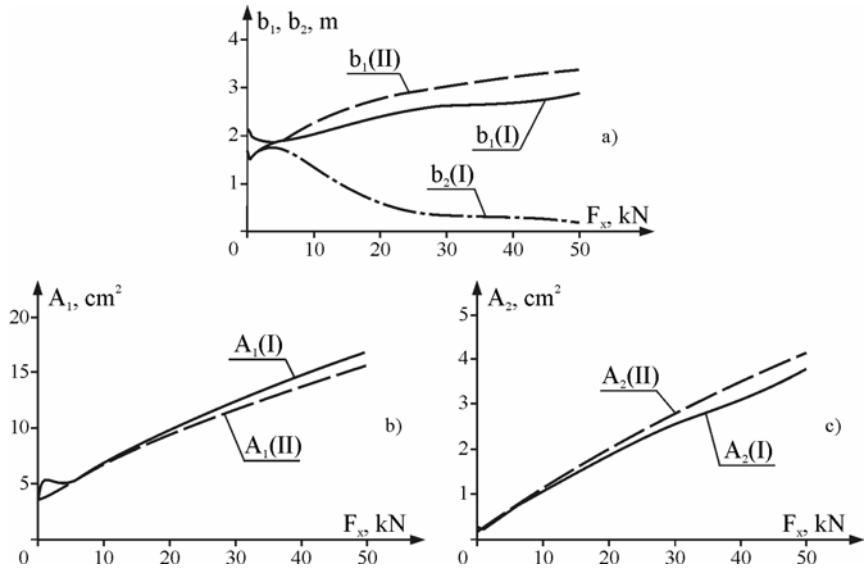

Fig. 2. Change of optimum parameters in the function of transverse force (F_x) for variable (I) and unvarying (II) shape lattice-columns

6. Conclusion

The optimization of the bracing column against buckling was performed in this paper. The analysis was carried out based on buckling criterions: general buckling of the lattice column, local buckling of the chord and local buckling of the bracing diagonal. This paper's objective is to determine optimal parameters of the variable shape lattice-columns. The optimal parameters were numerically determined. Obtained results are compared with the results that published in paper where goal was to determine optimal parameters of the unvarying shape lattice-columns.

Acknowledgement. The research work was supported by the Ministry of Science and Technological Development of the Republic of Serbia (Grant No. 36010).

References

[1] Andjelić N., Milošević-Mitić V., (2007), An approach to the optimization of thin-walled cantilever open section beams, Theoretical and Applied Mechanics, Vol.34, No.4, pp. 323-340, Belgrade
[2] Atanacković T., (1987), Teorija stabilnosti elastičnih štapova, FTN Novi Sad
[3] Banichuk N. V., Ragnedda F. and Serra M., (2004), Optimum shapes of bar cross-sections, Structural Multidisciplinary Optimization 23, 222–232
[4] Eurocode 3, (1992), Design of steel structures, CEN European Committee for Standardization, Brussels
[5] Farkas J., (1984), Optimum design of metal structures, Akademiai KIADO, Budapest
[6] Farkas J., Jármai K., (1997), Analysis and optimum design of metal structures, Rotterdam, Balkema
[7] Farkas J., (2005), Structural optimization as a harmony of design, fabrication and economy, Structural Multidisciplinary Optimization 30, 66–75
[8] Jarmai K., Farkas J., Optimum cost design of welded box beams with longitudinal stiffeners using advanced backtrack method, Structural Multidisciplinary Optimization (2001) 21: 52-59
[9] Гохберг М.М., (1988), Справочник по кранам, Машиностроение, Ленинград
[10] Kastratović G., Mijailović R., (2009), Optimum dimensions of trapezoid cross-section in lattice structures, 2nd International Congress of Serbian Society of Mechanics (IConSSM 2009), Palić (Subotica), Serbia, pp. C-01:1-10
[11] Lanfeng Yu, (2008), Calculation method and control value of static stiffness of tower crane, Journal of Mechanical Science and Technology 22, pp. 829–834
[12] Mijailovic R., Kastratovic G., (2009), Cross-section optimization of tower crane lattice boom, Meccanica 44: 599–611
[13] Mijailović R., (2010), Optimum design of lattice-columns for buckling, Structural and Multidisciplinary Optimization, Volume 42, Number 6, pp. 897–906
[14] Petković Z., Ostrić D., (1996), Metalne konstrukcije u mašinogradnji, Institut za mehanizaciju Mašinskog fakulteta Univerziteta u Beogradu, Belgrade
[15] Rondal J., Wurker K.G., Dutta D., Wardenier J., Yeomans N., (1992), Structural Stability of Hollow Sections, Verlag TUV Rheinland, Koln, Germany
[16] Selmic R., Cvetkovic P., (1993), Determination of optimum dimension of lattice structure cross-sections, Facta Universitatis 3, 365–372
[17] Selmic R., Cvetkovic P., Mijailiovic R., Kastratovic G., (2006), Optimum Dimensions of triangular cross-section in lattice structures, Meccanica 41: 391–406
[18] Selmic R., Cvetkovic R., Mijailovic R., (2006), Optimization of cross-section in structures, monograph, The Faculty of Transport and Traffic Engineering, Belgrade

Radomir Mijailović works as an associate professor at the Faculty of Transport and Traffic Engineering in Belgrade, Serbia, where he earned his Ph.D. He is the author/co-author of more than 50 research papers. Research interests: dynamic modeling and optimization of cranes and vehicles, energy efficiency, end-of-life vehicle.

MATHEMATICAL MODELING OF FUNCTIONS DEPENDENCE OF FORCE – DEFORMATION IN A COLLISION OF VEHICLES

Radomir Mijailović

Faculty of Transport and Traffic Engineering
The University of Belgrade, Vojvode Stepe 305, 11000 Belgrade, Serbia
e-mail: radomirm@beotel.rs

Abstract. Graph of dependence of force upon deformation is a commonly used graph in the field of the vehicle safety. The error present in determination of the modeling of preceding dependence has a considerable influence on the outcome results of the collision analysis. By comparative analysis of literature once can notice that the case of described previous dependences with two linear curves is often used (one for compression process and one for restitution process). By correlation analysis of experimental curves, we concluded that the previous approximation does not describe graph of dependence of force upon deformation with satisfactory way. This paper's objective is mathematical modeling of functions dependence of force – deformation in a collision of vehicles. The compression process was approximated with piecewise linear functions with one and more than one regions. The restitution process may be approximated with linear functions. The quality of the coherence between experimental curves and mathematical functions is quantified by residual sum of squares.

Keywords: vehicle, crash, force, deflection, residual sum of squares.

1. Introduction

Determining the adequate functions dependence of force upon deformation of vehicles must to represent one of the major tasks in the analysis of impact of vehicles [1]. Their determination influence importantly on reduction of error in the output result of the analysis of impact process.

There are a few approaches in literature for defining the functions dependence of force – deformation of collisions vehicles. Usually mechanical-mathematical model presume that the curve dependence of force upon deformation can be described with two linear curves (one curve for compression process and one curve for restitution process) [2]. In this case force can be described in form of multiplication of deformation and appropriate stiffness. The difficulty lays in determining the stiffness during the processes of compression and restitution of vehicles. The approximate expression for the processes of compression may be found in the literature [3, 4], where is used vehicle mass (m_v), impact velocity (v_0) and its maximal deformation (Δ_{max}):

$$c = \frac{m_v \cdot v_0^2}{\Delta_{\max}^2}. \tag{1}$$

To my knowledge the analytical expression for strictly determination of stiffness during the restitution processes is not yet available. Usually in practical defining the previous stiffness is through usage of coefficient of restitution. What is the problem? Usually mechanical-mathematical models presume cognition of numeric values of coefficient of restitution. In practice, it is common that numerical value of coefficient of restitution is determined on basis of experience. The error present in determination of the value of coefficient of restitution has a considerable influence on the outcome results of the collision analysis and determination of stiffness during the processes of restitution.

The force deformation curves for the vehicle models can also be approximated as piecewise linear with three regions: before buckling has started, after buckling has started and when the occupant compartment starts to deform [5].

Elmarakbi and Zu [6] presume that the curve dependence of compression force upon deformation can be described using piecewise linear functions but with two regions.

Usually authors presume that the force has zero value at the moment when the appropriate deformation has zero value. However, there are other approaches to determining the functions dependence of force upon deformation of vehicles. McCoy and Lankarani [7] presume that the force have value greater than zero at the initial moment of vehicle's crush when the deformation has zero value.

The experimental data for the crash tests may be found in literature. Most of the tests were made at about 60 km/h [8, 9]. It also can be found papers [10, 11, 12] which presented the experimental data for the same vehicle at different impact velocity.

Based on currently published papers may be noticed necessity for defining new functions dependence of force upon deformation of vehicles.

This paper's objective is to obtain new function that represent realistic behavior of vehicle during the impact. This function should be simple enough for practical implementation. We presume that the curve dependence of compression force upon deformation can be described using piecewise linear functions with three regions. Curves dependences for process of restitutions are approximated using linear functions with one and more than one regions. The stiffness during the process of restitution is expressed as function dependence of maximum vehicle deformation. Purpose of the model is reduction of error in the output results of the analysis of vehicle impact process.

2. The function dependence of force upon deformation

The function dependence of force upon deformation is determined by the following expression:

$$F = \begin{cases} F_k & for \quad \dot{\Delta} \geq 0 \\ F_r & for \quad \dot{\Delta} \leq 0 \end{cases}. \tag{2}$$

2.1. The function dependence of compression force upon deformation

In this paper the function dependence of compression force upon deformation of vehicles is analyzed in view of correlation for piecewise linear functions with one and more than one regions (*n* regions) (Fig. 1).

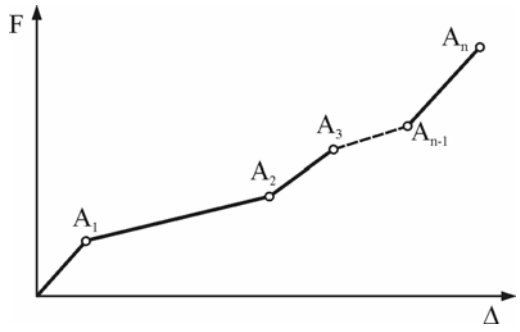

Fig. 1. Dependence of compression force upon deformation

Function of dependence of compression force upon deformation is given by expression:

$$F_{k,n} = \begin{cases} c_1 \cdot \Delta & for \quad 0 \le \Delta \le \Delta_{A_1} \\ c_1 \cdot \Delta_{A_1} + c_2 \cdot (\Delta - \Delta_{A_1}) & for \quad \Delta_{A_1} \le \Delta \le \Delta_{A_2} \\ c_1 \cdot \Delta_{A_1} + c_2 \cdot (\Delta_{A_2} - \Delta_{A_1}) + c_3 \cdot (\Delta - \Delta_{A_2}) & for \quad \Delta_{A_2} \le \Delta \le \Delta_{A_3} \\ \ldots & \ldots \\ c_1 \cdot \Delta_{A_1} + c_2 \cdot (\Delta_{A_2} - \Delta_{A_1}) + \ldots + c_n \cdot (\Delta - \Delta_{A_{n-1}}) & for \quad \Delta_{A_{n-1}} \le \Delta \le \Delta_{A_n}, \end{cases} \tag{3}$$

where

- F_k – compression force,
- Δ – deformation of vehicle,
- Δ_n – maximum value of deformations during process of compression (experimental data),
- c_i – coefficients of proportionality during process of compression (region "*i*").

Coefficient of proportionality (c_1 for n=1) in literature is known as the coefficients of stiffness. Therefore, in the following text we will use notion stiffness for c_i.

It is necessary to define following unknown parameters c_i and $\Delta_{A,i}$ (i=1 ... n-1).

Experiment is necessary in order to mathematical modeling of functions dependence of force upon deformation. In that sense experiment consists of impact of vehicles into an absolutely rigid barrier. To gain a better output results experiment must be repeated for different values of impact velocity [5, 10, 11, 12].

The quality of the coherence between experimental curves and mathematical functions is quantified by residual sum of squares. Why was chosen just residual sum of squares? The function of dependence of compression force upon deformation done by the minimization

of a residual sum of squares also has minimum error using it in determination work during compression process. A minimal error in determining the work also results in a minimal error in determining coefficient of restitution.

Residual sum of squares (RSS) measures the deviations of experimental from their predicted values:

$$RSS = \sum_{i=1}^{nk} (F_{k,i} - F_{k,\exp,i})^2 , \tag{4}$$

where $F_{k,exp,i}$ is the i^{th} experimental value of the variable to be predicted, and $F_{k,i}$ is the predicted value of $F_{k,exp,i}$.

The determination of unknown parameters was performed by the minimization of a residual sum of squares. We concluded that the analytical solution of minimization of the function (4) can't be determined for $n \geq 1$ (3) by application of some optimization methods [13]. Therefore, the unknown parameters (c_i, $\Delta_{A,i}$) should be numerically determined.

2.2. The function dependence of restitution force upon deformation

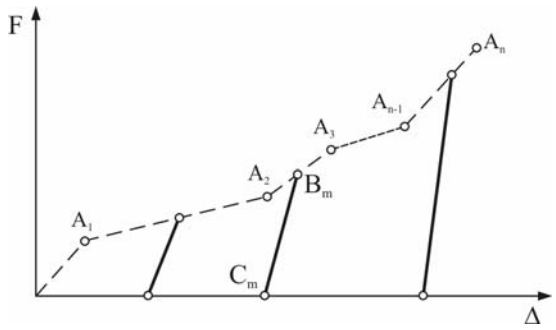

Fig. 2. Dependence of restitution forces upon deformation (dash line – compression force; solid line – restitution forces)

The restitution process is significantly shorter than compression process.

By the author using more complex functions wouldn't significantly reduce the error, but on the other hand would be more complicated. Therefore, the restitution process was approximated with linear curve (Fig. 2). Slopes of restitution lines are a function of maximum value of deformation during process of compression (Δ_{Bm}).

Functions of dependence of restitution force upon deformation are given by expression:

$$F_{r,m} = F_k(\Delta_{B_m}) - b_m \cdot (\Delta_{B_m} - \Delta) , \tag{5}$$

where

- $F_{r,m}$ – restitution force,
- Δ_{Bm} – maximum value of deformations during process of compression,

– b_m – stiffness (coefficients of proportionality) during process of restitution for Δ_{Bm}.

Stiffness (b_m) can be determined from the conditions: during restitution process work determined by experimental data ($A_{r,m,exp}$) is equal to work determines using approximate functions (5) ($A_{r,m,appr}$):

$$A_{r,m,\exp} = A_{r,m,appr} \,. \tag{6}$$

Numerical value of work $A_{r,m,exp}$ can be determined by using experimental data for the same vehicle characteristics and for different values of impact velocities. The analysis output data are two numerical values: Δ_{Bm} and $A_{r,m,exp}$.

Numerical value of work $A_{r,m,appr}$ is given in following form:

$$A_{r,m,appr} = \int_{\Delta_{B_m}}^{\Delta_{C_m}} F_{r,m}\, d\Delta \,. \tag{7}$$

Deformation of vehicle in the instant of separation (Δ_{Cm}) may be determined from the condition:

$$F_{r,m}(\Delta_{C_m}) = 0 \,. \tag{8}$$

The deformation Δ_{Cm} can be determined by substitution of (5) into (8):

$$\Delta_{C_m} = \Delta_{B_m} - \frac{F_k(\Delta_{B_m})}{b_m} \,. \tag{9}$$

Finally, stiffness b_m can be determined by applying equations (5), (6), (7) and (9):

$$b_m = -\frac{[F_k(\Delta_{B_m})]^2}{2 \cdot A_{r,m,\exp}} \,. \tag{10}$$

The stiffness b_m depends on the deformation Δ_{Cm} (10). The final step of modeling may be correlation analysis between b_m and Δ_{Cm}.

3. Numerical example and the analysis of results

The analysis of unknown parameters was performed using experimental data given in paper [11] where the results obtained through experimental analysis for Ford Escort. The experimental data from previous paper was derived using the case of direct central impact of vehicles into an absolutely rigid barrier.

Quality comparison between two piecewise linear functions with subsequent number of regions (i.e. n and n+1) may be presented by comparing their RSS relative discrepancy:

$$\delta RSS_{n=i \wedge n=i+1} = \left| \frac{RSS_{i+1} - RSS_i}{RSS_{i+1}} \right| \cdot 100,\% \,, \tag{11}$$

$$\delta RSS_{n=1\wedge n=2} = 122.1\%\,,\ \delta RSS_{n=2\wedge n=3} = 3.7\%\,,\ \delta RSS_{n=3\wedge n=4} = 0.1\% \quad (12)$$

The relative discrepancies for $n\geq 4$ tend to zero.

The same calculation was used for comparing two functions with $n=1$ where stiffness obtained using equations (1) and (4):

$$\delta RSS_{n=1(Eq.1\wedge Eq.4)} = \left| \frac{RSS_{(Eq.1)} - RSS_{(Eq.4)}}{RSS_{(Eq.1)}} \right| \cdot 100,\%\,, \quad (13)$$

$$\delta RSS_{n=1(Eq.1\wedge Eq.4)} = 11.4\%\,. \quad (14)$$

The approximate expression for the compression stiffness (1) is often used in practice. By analysis of equations (12) and (14) it can be concluded that this expression hasn't satisfactory results.

Therefore, we propose to use piecewise linear functions dependence of compression force upon deformation with three regions.

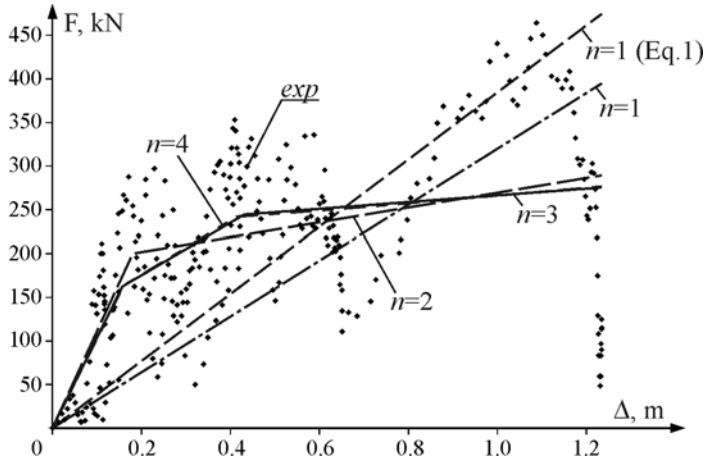

Fig. 3. Dependence of compression force upon deformation for Ford Escort (exp – experimental data, n=1...4 – approximations (Eq. 3)

Functions of dependence of compression force upon deformation (3) with n regions (n=1...4) and experimental data are presented in a Figure 3. By visual analysis of Figure 3 it can be also concluded that expression (3) for n=1 and n=2 doesn't have satisfactory results.

Compression stiffness (c_i) and deformation ($\Delta_{A,i}$) for linear functions dependence of compression force upon deformation with three regions have following values:

$$\begin{aligned} a_1 &= 1034\,kN/m,\ \Delta_{A_1} = 0.16\,m, \\ a_2 &= 299\,kN/m,\ \Delta_{A_2} = 0.43\,m, \\ a_3 &= 38\,kN/m,\ \Delta_{A_1} = 1.23\,m. \end{aligned} \quad (15)$$

The stiffness b_m using equation (10) have following values:

$$\begin{aligned} b_1 &= 45729\,kN/m,\ \Delta_{B_1} = 0.12\,m, \\ b_2 &= 55199\,kN/m,\ \Delta_{B_2} = 0.42\,m, \\ b_3 &= 49853\,kN/m,\ \Delta_{B_3} = 0.65\,m, \\ b_4 &= 624049\,kN/m,\ \Delta_{B_4} = 1.23\,m. \end{aligned} \tag{16}$$

The stiffness b_m were approximated using the previous results (16) by correlation analysis:

$$b = 5255440 + 100783750 \cdot \Delta_B^{7,733}. \tag{17}$$

v_0, km/h	k	k_{exp}
13	0.149	0.162
38	0.088	0.085
52	0.070	0.071
83	0.012	0.015

Table 1.

The purpose of the model presented in this paper is reduction of error in the output results of analysis of vehicle impact process. Therefore, coefficient of restitution of impact of vehicles into an absolutely rigid barrier is calculated using the model presented in this paper (k). The results were presented in the Table 1. The coefficient of restitution calculated using appropriate experimental data (k_{exp}) was also presented in Table 1. The absolute error of coefficient of restitution has value in the range from 0.001 to 0.013.

4. Conclusions

The error presented in determination of the function dependence of force upon deformation has a considerable influence on the outcome results of the collision analysis. In this paper is suggested mathematical model of functions dependence of force upon deformation. The compression process was approximated with piecewise linear functions with three regions. The restitution process may be approximated with linear curve. This model can be used for analysis real traffic accident.

The PC-Crash software is a common commercial tool for reconstructing road accidents [14]. It uses a number of important parameters for vehicle model. Most of them are given by default, within the software, and the results of the accident reconstruction are very sensible to their variations. The coefficient of restitution is one of them, used as the input data, and usually taken arbitrary. The model is developed in this paper which provides such analysis of impact process in which the coefficient of restitution becomes the result, and not input data.

Further investigations may be directed towards establishing an analytical model for analysis of three dimensional vehicles collisions with the coefficient of restitution as the end result. Such analysis of collision processes would contribute to the analysis of traffic accidents.

Acknowledgement. The research work was supported by the Ministry of Science and Technological Development of the Republic of Serbia (Grant No. 36010).

References

[1] Harmati I.A., Rovid A., Varlaki P., Application of LPV Type Force Model in Vehicle Crash Dynamics, Proceedings of the 9th WSEAS International Conference on Applications of computer engineering, 2010.
[2] Pawlus W., Karimi H.R., Robbersmyr K.G., Mathematical modeling of a vehicle crash test based on elasto-plastic unloading scenarios of spring-mass models, The International Journal of Advanced Manufacturing Technology, in press
[3] Janković A, Simić D, Vehicle safety, monograph, DSP-mecatronic, Kragujevac, 1996.
[4] Nusholtz, G.S., Xu L., Shi Y., Domenico L.D., Vehicle mass, stiffness and their relationship, 19th ESV, Paper number 05-0413, 2005.
[5] Van der Zweep C.D., Jenefeldt F., Thomson R., Van der Zweep C.D., Jenefeldt F., Thomson R., 2002. Improvement of vehicle crash compatibility through the development of crash test procedure, Project number – GRD2-2001-50083, 1998-2002., Project number – GRD2-2001-50083, 1998-2002.
[6] Elmarakbi A., Zu J., Mathematical modelling of a vehicle crash with emphasis on the dynamic response analysis of extendable cubic nonlinear dampers using the incremental harmonic balance method, Proc. IMechE Vol. 221 Part D: J. Automobile Engineering, pp. 143 – 156, 2007
[7] McCoy M.L., Lankarani H.M., Determination of the crush stiffness coefficients of a typical aftermarket frontal protective guard used in light trucks and vans with comparisons between guard stiffness and frontal vehicle crush coefficients, Proceedings of the Institution of Mechanical Engineers, Part D: Journal of Automobile Engineering, Vol. 220, 2006, pp. 1073 – 1084
[8] www.nhtsa.dot.gov
[9] Huibers J., de Beer E., Curent front stiffness of European vehicles with regard to compatibility, International Technical Conference on the Enhanced Safety of Vehicles (ESV), Amsterdam, The Netherlands, June 4 - 7, 2001.
[10] Kerkhoff JF, Husher SE, Varat MS, Busenga AM, Hamilton K, An investigation into vehicle Frontal impact stiffness, BEV and repeated testing for reconstruction, Society of Automotive Engineers International Congress, Detroit, Michigan, 1993, SAE Paper 930899
[11] Steffan H., Geigl B. C., Moser A., Hoschopf H., Comparison of 10 to 100 km/h rigid barrier impacts, Paper No. 98-S3-P-12
[12] Varat M. S., Husher S. E., Vehicle impact response analysis through the use of acceleration data, SAE Tech. Paper 2000-01-0850, 2000.
[13] Selmic R., Cvetkovic R., Mijailovic R., (2006), Optimization of cross-section in structures, monograph, The Faculty of Transport and Traffic Engineering, Belgrade
[14] Depriester JP, Perrin C, Serre T, Chalandon S., Comparision of several methods for real pedestrian accident, 2006, http://www.mathlab.mtu.edu/~struther/Drop/Modeling/05-0333-O.pdf

Radomir Mijailović works as an associate professor at the Faculty of Transport and Traffic Engineering in Belgrade, Serbia, where he earned his Ph.D. He is the author/co-author of more than 50 research papers. Research interests: dynamic modeling and optimization of cranes and vehicles, energy efficiency, end-of-life vehicle.

BENDING OF A THIN PLATE SUBJECTED TO STRONG UNIFORM MAGNETIC FIELD

V. Milošević-Mitić, T. Maneski, N. Anđelić

Faculty of Mechanical Engineering,

University of Belgrade, Kraljice Marije 16, 11120 Belgrade 35

e-mail: vmilosevic@mas.bg.ac.rs

Abstract. The problem of an elastic plate, originally unmagnetized, in a uniform magnetic field is considered in the paper. The magnetic forces are of two kinds: the force of the magnetic field on conducting currents in the material, induced by its motion in the static field and the force between the magnetic field and the magnetized material (independent of the motion).The general equations are linearized by assuming linear constitutive equations and that all electromagnetic variables in the deformed body may be divided into two parts: a rigid body state and a perturbation state. Maxwell's stress is calculated and involved in differential equation related to bending. Obtained equation is solved in analytical form using the integral-transformation technique (Double Fourier finite-sine transformation and Laplace transformation). Discussion of the obtained solution is done using Kirchhoff's hypothesis.

1. Introduction

The theory of electro-magneto-thermoelasticity investigates the interaction between the straian and the electromagnetic field in a solid elastic body. A propagation of an elastic field in presence of magnetic field was considered by L. Knopoff (1955), J.W. Dunkin i A.C. Eringen (1963). F.W. Brown (1966) developed a rigorous phenomenological theory for ferromagnetic materials on the basis of the large deformation theory and the clasical theory of feromagnetisam. H.F. Tiersten (1964) developed an analogous theory based on a microscopic model. Since the general nonlinear theory is complicated, Y.W. Pao and C.S. Yeh [1] derived a set of linear equations and boundary conditions for soft feromagnetic elastic materials. They applied linear theory to investigate magnetoelastic buckling of an isotropic plate. The same problem was treated on the other way by F.C. Moon i Y.H. Pao [2]. Basic general information about the theory of magneto-thermoelasticity was presented in monographs by H. Parkus [3]. A great contribution of a research in this scientific field was given by W. Nowacki, S.A. Ambarcumian [4], M. Krakowski [5]. From 1975 on Michigan Technological University (N.S. Christopherson, M.O. Peach, J.M. Dalrymple, L.G. Viegelahn [6]), a set of experiments were done to reconsider theoretical results. Because of a disagreement in analytical and experimental results methods of numerical analyses were involved in consideration (K. Miya, T. Takagi, Y. Ando (1980), X. Tian and Y. Shen [7]). Sharma and Pal investigated the propagation of magnetic-thermoelastic plane

wave in homogeneous isotropic conducting plate under uniform static magnetic field [8]. The problem with high-frequncy electromagnetic waves was presented in [9] and the problem with low-frequency electromagnetic field was descused in [10].

2. Basic equations

Electro-magneto-thermoelastic problem considered in the paper shows one type of interaction between electromagnetic and strain field in a solid plate. It is assumed that the plate material is elastic and isotropic, possessing a good electric conductivity. Many nickel-iron alloys used for building the magnetic circuits of motors, generators, inductors, transformers are of this type.

As a result of time changing electromagnetic field conducting currents appear in electric conductors. This problem is mathematically described by the system of Maxwell's equations with the relations for slowly moving media and modified Ohm's low [6]:

$$rot\vec{H} = \vec{J} + \frac{\partial \vec{D}}{\partial t}, \qquad rot\vec{K} = -\frac{\partial \vec{B}}{\partial t},$$

$$div\vec{D} = 0, \quad div\vec{B} = 0, \tag{1}$$

$$\vec{D} = \varepsilon_0\left(\vec{K} + \dot{\vec{u}} \times \vec{B}\right), \qquad \vec{B} = \mu\left(\vec{H} - \dot{\vec{u}} \times \vec{D}\right),$$

$$\vec{J} = \sigma\left(\vec{K} + \dot{\vec{u}} \times \vec{B}\right),$$

where the following notation is applied: H – intensity of the magnetic field, K – intensity of the electric field, B – magnetic flux density (magnetic induction), D – electric induction, J – current density, u – deflection, μ_0 – permeability of vacuum, σ – electric conductivity, ε_0 – dielectric constant of vacuum, t – time.

In the consideration of the plate vibrations, we shall take the assumption that the longitudinal vibrations are independent of transversal vibrations. Transversal vibrations can be obtained by using the following differential equation [11]:

$$D\nabla_1^4 w - \rho h\ddot{w} + \frac{\rho h^3}{12}\ddot{w} = \left(\sigma_{33}^+ - \sigma_{33}^-\right) + \left(T_{33}^+ - T_{33}^-\right) + \frac{h}{2}\frac{\partial}{\partial x_i}\left(\sigma_{i3}^+ + \sigma_{i3}^-\right) +$$

$$+ \frac{h}{2}\frac{\partial}{\partial x_i}\left(T_{i3}^+ + T_{i3}^-\right) + \int_{-\frac{h}{2}}^{\frac{h}{2}}\left(X_{i,i} + f_{i,i}\right)x_3 dx_3 + \int_{-\frac{h}{2}}^{\frac{h}{2}} X_3 dx_3, \qquad (i=1,2), \tag{2}$$

where: D – flexural rigidity of the plate, X – mechanical force, f – Lorenz force. σ_{ij} and T_{ij} denote mechanical and magnetic stress tensors (σ_{ij}^+, T_{ij}^+ are stress components on the upper and σ_{ij}^-, T_{ij}^- on the lower side of the plate), where h is the plate thickness and ∇_1^4 is the four-dimension Laplace operator.

Of course, presented systems of equations has to be accomplished with the appropriate set of boundary and initial conditions.

Presented system of differential equations is complicated to be solved in analytical form. So, at first we have to simplify mathematical model of the discusted problem. In this paper only the problem of the plate subjected to homogenius magnetic field will be presented.

In this case, electromagnetic energy which is converting in thermal energy is very small, so Joules heat can be neglected. Mahwell's equations (1) can be linearysed, too. Deformation field is coupled with the magnetic field.

3. Thin metallic plate in a stationary homogenius magnetic field

Let the thin simply supported plate made of homogenius, isotropic linear magnetic material is subjected transversal to an external uniform homogenius magnetic field induction $\vec{B}_0 = \mu_0 \vec{H}_0$ in air. The magnetic permeability of the plate material is $\mu=\mu_0\mu_r$ and at the beginning the plate is quite non-magnetized (Figure 1).

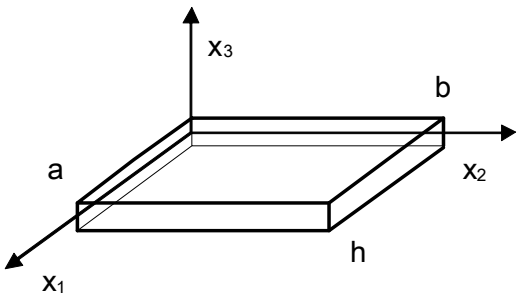

Figure1. Coordinate system and plate dimensions

In that case we have two kinds of forces:

1. forces of interaction between magnetic field and magnetized material, independent of vibrations - motion and

2. forces of the magnetic field and the conducting currents in the plate material, induced by the plate vibrations in the stationary magnetic field.

Electromagnetic field forming in the plate appeares on the action of magnetized material and macroscopic conducting current, as can be presented in next way

$$\vec{H}_p = \vec{H}_{p0} + \vec{h}_p^1 + \vec{h}_p^2 , \tag{3}$$

where $\vec{h}_p^1$ and $\vec{h}_p^2$ are small fluctuations of the magnetic field generated on the presented actions. In the mathematical model their influence on each other can be neglected.

If the thin metallic plate is placed in strong homogeneous magnetic field $H_0=const$. appropriate of the law of the line refraction, in the plate is forming magnetic field intensity H_{p0}. In the moment $t=0$ plate is losing stability place, apropos the plate has initial deformation conditions. It can be presented in the next form

$$w(x_1,x_2,0)=\varphi_0(x_1,x_2),\qquad \left.\frac{\partial w(x_1,x_2,t)}{\partial t}\right|_{t=0}=\varphi_1(x_1,x_2). \tag{4}$$

On the coupling between the electromagnetic field and the deformation field there are small fluctuations of the electric field $\vec{e}$ and the magnetic field in the plate $\vec{h}_p^2$, defined as

$$\vec{H}_p(x_1,x_2,x_3,t)=\vec{H}_{po}+\vec{h}_p^2(x_1,x_2,x_3,t), \tag{5}$$

$$\vec{K}(\vec{x},t)=\vec{e}(\vec{x},t).$$

As the change of the magnetic field under a deformation is small, for ferromagnetic materials can be accepted that the magnetic permeability is nearly constant $\mu \cong const.$. Neglecting of the productions between the values h_{pi}^2, e_i , v_i and the productions of their derivatives, relations (1) have the next form [6]

$$\vec{D}=\varepsilon\left(\vec{e}+\mu\vec{v}\times\vec{H}_{p0}\right),\qquad \vec{B}=\mu\left(\vec{H}_{p0}+\vec{h}_p^2\right),$$

$$\vec{J}=\sigma\left(\vec{e}+\mu\vec{v}\times\vec{H}_{p0}\right), \tag{6}$$

and the Maxwell's equations are

$$rot\vec{h}_p^2=\sigma\left(\vec{e}+\mu\vec{v}\times\vec{H}_{p0}\right)+\varepsilon\left(\dot{\vec{e}}+\mu\dot{\vec{v}}\times\vec{H}_{p0}\right),\qquad rot\vec{e}=-\mu\dot{\vec{h}}_p^2,$$

$$\varepsilon div\vec{e}+\varepsilon\mu div\left(\vec{v}\times\vec{H}_{p0}\right)=0,\qquad div\vec{h}_p^2=0. \tag{7}$$

Lorient's force has a form

$$\vec{f}=J\times B=\mu\left(rot\vec{h}_p^2-\dot{\vec{D}}\right)\times\vec{H}_{p0}. \tag{8}$$

By eliminating value $\vec{e}$ we can form differential equation for the magnetic field [6] as

$$\nabla_1^2\vec{h}_p^2-\sigma\mu\dot{\vec{h}}_p^2-\varepsilon\mu\ddot{\vec{h}}_p^2=\sigma\mu rot\left(\vec{v}\times\vec{H}_{p0}\right)-\varepsilon\mu rot\left(\dot{\vec{v}}\times\vec{H}_{p0}\right). \tag{9}$$

In the case of the quazistationry electromagnetic field we have $\vec{D}=0$, $\dfrac{\partial\vec{D}}{\partial t}=0$, or $\varepsilon\equiv 0$, so presented equations have simplified form

$$\vec{f}=\mu rot\vec{h}_p^2\times\vec{H}_{p0}, \tag{10}$$

$$\left(\nabla_1^2-\sigma\mu\partial_t\right)\vec{h}_p^2=-\sigma\mu rot\left(\dot{\vec{u}}\times\vec{H}_{p0}\right). \tag{11}$$

The whole equation system of this coupled magnetoelastic bending problem is consisted of the equations (11) and (2) together with the appropriate boundary and initial conditions and relation (10).

Let us discus one special case when the magnetic field is transversal to the middle surface of the thin plate. The plate is rectangular with the material density ρ (Figure 1.). Using the

condition of the equality of the perpendicularity components on the magnetic induction on the boundary surfaces, the field forming in the plate is

$$H_{p0} = \frac{\mu_0}{\mu} H_0 , \qquad \vec{H}_{p0} = \left(0,0,-H_{p0}\right). \tag{12}$$

If the plate material has high electric conductivity we can say that

$$\vec{h}_p^2 \cong rot\left(\vec{u} \times \vec{H}_{p0}\right) = \left(w_{,1} H_{p0}\right)\vec{i} + \left(w_{,2} H_{p0}\right)\vec{j} - \left(\nabla_1^2 w x_3 H_{p0}\right)\vec{k} , \tag{13}$$

$$\vec{f} \cong -\left(\mu \nabla_1^2 w_{,1} x_3 H_{p0}^2\right)\vec{i} - \left(\mu \nabla_1^2 w_{,2} x_3 H_{p0}^2\right)\vec{j} . \tag{14}$$

Appropriate deferential equation of the transversal vibrations, using (2), is

$$D\nabla_1^4 w + \rho h \ddot{w} + \frac{\rho h^3}{12}\nabla_1^2 \ddot{w} = \left(T_{33}^+ - T_{33}^-\right) + \int_{-\frac{h}{2}}^{\frac{h}{2}} \left(f_{1,1} + f_{2,2}\right) x_3 dx_3 + \int_{-\frac{h}{2}}^{\frac{h}{2}} X_3 dx_3 . \tag{15}$$

As induced tangential components of the field are small compared to the normal component, appropriate stresses on the upper and the lower side of the plate are formed under the influence of the normal components intensities

$$H_p = H_{p0}\left(1 + x_3 \nabla_1^2 w\right), \qquad H_{0v} = H_0\left(1 + x_3 \nabla_1^2 w\right). \tag{16}$$

Using Maxwell's formula for the stress on the splitted surface of the two magnetics, and the fact that the stress is directing to the medium of the smaller magnetic permeability, we can take next relation

$$T_{33}^+ - T_{33}^- = \left(\mu - \mu_0\right)\frac{\mu_0}{\mu} h H_0^2 \nabla_1^2 w . \tag{17}$$

Equation (15) has the form

$$\left(D + \frac{\mu_0^2}{\mu} H_0^2 \frac{h^3}{12}\right)\nabla_1^4 w - \left(\mu - \mu_0\right)\frac{\mu_0}{\mu} h H_0^2 \nabla_1^2 w + \rho h \ddot{w} - \frac{\rho h^3}{12}\nabla_1^2 \ddot{w} = -\rho g h . \tag{18}$$

Boundary conditions for the simply supported plate are

$$w_{x_1=0,a} = 0 , \qquad \left.\frac{\partial^2 w}{\partial x_1^2}\right|_{x_1=0,a} = 0 , \tag{19}$$

$$w_{x_2=0,b} = 0 , \qquad \left.\frac{\partial^2 w}{\partial x_2^2}\right|_{x_2=0,b} = 0 .$$

System of the equations (18) and (19) with the initial conditions (4) can be solved using integral transform technique – double sine Fourier transformation and the Laplace transformation. Obtained solution has next form

$$w(x_1,x_2,t)=\frac{4}{ab}\sum_{m,n=1,3,5\ldots}^{\infty}\sum w_{mn}(t)\sin\alpha_n x_1\sin\alpha_m x_2\ ,$$

$$w_{mn}(t)=\varphi_{0nm}\cos\omega_{nm}t+\varphi_{1nm}\frac{\sin\omega_{nm}t}{\omega_{nm}}-\frac{4\rho gh}{\alpha_n\alpha_m\left[\rho h+\frac{\rho h^3}{12}\left(\alpha_n^2+\alpha_m^2\right)\right]}\frac{1-\cos\omega_{nm}t}{\omega_{nm}^2}\ ,$$

$$\omega_{nm}^2=\frac{\left(D+\frac{\mu_0^2}{\mu}H_0^2\frac{h^3}{12}\right)\left(\alpha_n^2+\alpha_m^2\right)^2+\left(\mu-\mu_0\right)\frac{\mu_0}{\mu}hH_0^2\left(\alpha_n^2+\alpha_m^2\right)}{\rho h+\frac{\rho h^3}{12}\left(\alpha_n^2+\alpha_m^2\right)}\ ,$$

$$\alpha_n=\frac{n\pi}{a}\ ,\qquad\qquad \alpha_m=\frac{m\pi}{b}\ , \tag{20}$$

$$\varphi_{knm}=\int_0^a\int_0^b\varphi_k(x_1,x_2)\sin\alpha_n x_1\sin\alpha_m x_2\,dx_1dx_2\qquad (k=0,1).$$

4. The conclusion

The analysis of the obtained results can be done using relation for ω_{nm}. In the cases of the paramagnetics and ferromagnetics we have $(\mu-\mu_0)>0$ and the magnetic field is acting in the same direction of the elastic field. It means that the magnetic field is in corelation with the elasic field and they together gravity to return the plate in the equilibrium position. For diamagnetic materials we have $(\mu-\mu_0)<0$ and the magnetic field is acting in opposite direction of the direction of the elastic field.

Using relation (17) and Kirchoff hypothesis, on the base of a sign of $\nabla_1^2 w$, we have to conclude that in the case of the plate clamped on only one side we have opposite situation.

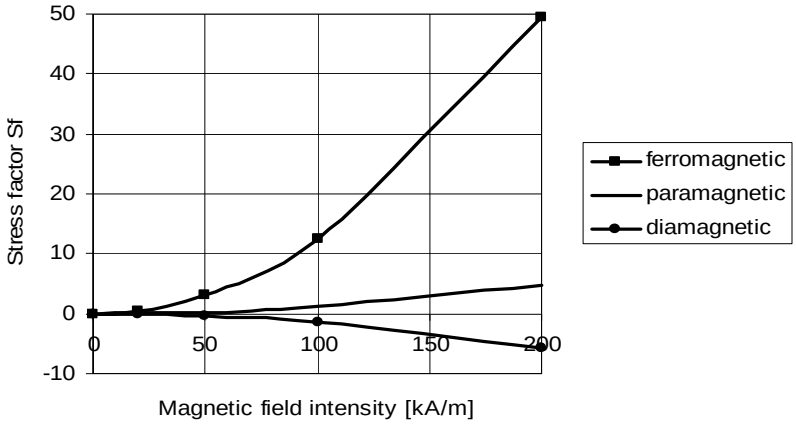

Figure 2. Stress factor as a function of magnetic intensity

On the base on the relation (17) stress factor, defined as

$$S_f = \frac{T_{33}^{+} - T_{33}^{-}}{\nabla_1^2 w}, \tag{21}$$

is presented on diagram from figure 2. As can be noticed, considered problem is interesting only for ferromagnetic plates and very strong magnetic fields.

In the reference [7] the hypothesis of the magnetoelasticity for real conductors were formed and the appropriate theory was developed. On that theory, for the case of the plate placed transversal to magnetic field we have the opposite conclusions. As that theory is not in agreement with Kirchoff hypothesis in the paper [12] modified hypothesis were defined. Than, the correct result can be involved and for a real conductors.

Presented theoretical analysis has the assumption that the plate is subjected to hardly uniform and hardly transversal magnetic field. Obtained theoretical results are valid only for very thin plates. In the case of thick plate we have the boundary effect, and we have to involve in consideration finite element method.

Acknowledgements. This work is a contribution to the Ministry of Science of the Republic of Serbia funded projects TR 35040 and TR 35011.

REFERENCES

[1] PAO Y.H.; YEH C.S.: *A Linear Theory for Soft Ferromagnetic Elastic Solids*, Int. J. Enging. Sci., 11 (1973) 415-436.

[2] MOON F. C.; PAO Y. W.: *Magnetoelastic Buckling of a Thin Plate*, Journal of Applied Mech., 35, Trans. ASME, Ser. E (1968) 53-58.

[3] PARKUS H.: Electromagnetic Interactions in Elastic Solids, Springer-Verlag (1979)

[4] AMBARCUMIAN S.A.; BAGDASARIAN G.E.; BIELUBIEKIAN M.V.: *Magnetoelasticity of Thin Shells and Plates* [in Russian], Nauka, Moscow (1977)

[5] KRAKOWSKI M.: Mathematical Model of Eddy Currents in a Metallic Solid after Applying an External Magnetic Field, Bullet. of the Polish Acad. of Science, 29, No. 5-6, Varsaw (1981) 67-71.

[6] PEACH M.O.; CHRISTOPHERSON N.S.; DALRYMPLE J.M.; VIEGELAHN G. L.: *Magnetoelastic Buckling: Why Theory and Experiment Disagree*, Experimental Mech., 28, No 1 (1988) 65-69.

[7] TIAN X.; SHEN Y.: Generalized magneto-thermoelasticity solved by FEM in time domain, Springer, Comput. Methods (2006) 1621-1627.

[8] SHARMA J.N.; PAL M.: Rayleigh-Lamb waves in magneto-thermoelastic homogeneous isotropic plate, Int. J. of Eng. Sci. 42 (2004) 137-155.

[9] Miloševic-Mitić V, Kozak D, Maneski T, Anđelić N, Gaćeša B, Stojkov M, Dynamic nonlinear temperature field in a ferromagnetic plate induced by high frequency electromagnetic waves*, Strojarstvo* Vol. 52, No. 2 (2010) 115-124

[10] Milošević-Mitić V, Maneski T, Temperature Loading of a Thin Metallic Plate Subjected Transversal to Law-Frequency Electromagnetic Field, *FME TRANSACTIONS*, Vol 38, No. 2 (2010) 95-101

[11] MILOŠEVIĆ-MITIĆ V. Magneto-thermo-elastic bending of thin plates; *Monogr., Zadužbina Andrejević*, Belgrade (1999)

[12] Rudnicki M, A Modified Hypothesis of magnetoelasticity of Plates, Bull. of the Polish Academy of Sciences, Vol. 32, no 3-4, (1984) 101-112

SOME QUADRATURE RULES FOR FINITE ELEMENT METHOD AND BOUNDARY ELEMENT METHOD

G.V. Milovanović[1], T. Igić[2], N. Tončev[2]

[1] Faculty of Computer Sciences, Megatrend University, Bulevar Umetnosti 29, 11070 Novi Beograd, Serbia
e-mail: gvm@megatrend.edu.rs
[2] Faculty of Civil Engineering and Architecture, University of Niš, A. Medvedeva 14, 18000 Niš, Serbia
e-mail: tomislav.igic@gaf.ni.ac.rs

Abstract. The boundary element method (BEM) and the f nite element method (FEM) are very popular in many computational applications in engineering. These methods very often require the numerical evaluation of one dimensional or multiple integrals with singular or near singular integrands. Such problems appear in many subjects of mechanics (fracture mechanics, damage mechanics, etc.), as well as in other technical f elds. In this paper we give some improvements of quadrature rules for FEM and BEM. Beside of general notions on Gaussian quadratures, we give a construction of weighted Gaussian quadratures for integrals with logarithmic and/or algebraic singularities. Also, we consider generalized quadratures of high degree of precision for Müntz systems. Numerical examples are included.

1. Introduction

The boundary element method (BEM) and the f nite element method (FEM) are very popular in many computational applications in engineering, for example, in fracture mechanics, damage mechanics, electromagnetic diffraction, etc. Very often in such applications we need accurate numerical evaluation of one dimensional or multiple integrals with singular kernels and/or singular basis functions. Two kinds of singularities are typical: algebraic and logarithmic. Müntz and Müntz-logarithmic polynomials are typical functions with such properties. Also, an accurate evaluation of nearly singular one and multidimensional integrals is very important. For some additional details see, for example, [1], [9], [7], [8], [10], [11], [17], [18].

In this paper we propose a method for constructing the weighted Gaussian quadrature rules for integrals with algebraic and/or logarithmic singularities. This method gives Gaussian quadratures with a maximal algebraic degree of precision. Also, we mention another approach which enables us to obtain Gaussian quadratures for Müntz systems (for details see Milovanović [13] and Milovanović and Cvetković [15]).

Beside of general notions on quadratures of high algebraic degree of precision, we consider a stable and eff cient construction of the weighted Gaussian quadratures for integrals of functions with end-point singularities. Such a construction is based on an application of the `Mathematica` package `OrthogonalPolynomials`, recently developed by Cvetković and Milovanović [2]. Numerical examples are included.

2. Quadrature Formulas for Integrals With Logarithmic Weight Functions

In numerical implementation of the BEM (see [9, Chapters 4 & 5]), quadrature formulas play a very important role, especially for higher order elements. For calculating integrals of the corresponding influence coefficients (for off-diagonal elements and diagonal elements), quadratures of Gaussian type are very appropriate. For sufficiently smooth functions on a finite interval $[a,b]$ a linear transformation to the standard interval $[-1,1]$ can be used and then an application of Gauss-Legendre quadrature formula provides numerical integration with a satisfactory accuracy. However, for integrals with a logaritmic singularity and/or some kind of algebraic singularities the convergence of the corresponding quadrature process is very slow, so that certain weighted quadratures are recommended. In such cases, the weight functions of the corresponding weighted Gaussian quadratures include these "difficult parts (with singularities)" of the integrand. In this section, we consider a few cases of such quadratures on the standard interval $[0,1]$. However, we first give some general notions on Gaussian quadratures.

2.1. General notions of Gaussian quadratures

Let $\mathscr{P}_m$ be a set of all algebraic polynomials of degree at most m. We consider the n-point weighted quadrature formula

$$\int_a^b f(x)w(x)\,dx = \sum_{k=1}^{n} A_k f(x_k) + R_n(f), \tag{1}$$

where the weight function $w(x)$ is such one that all its moments $\mu_k = \int_a^b x^k w(x)\,dx < +\infty$, $k = 0,1,\ldots$, and $\mu_0 > 0$. Quadrature rule (1) is known as *interpolatory* if it is exact for all polynomials of degree at least $n-1$, i.e., if the remainder term $R_n(f) = 0$ for each $f \in \mathscr{P}_{n-1}$.

However, if the nodes x_k and the weights A_k in (1) are selected so that $R_n(f) = 0$ for each $f \in \mathscr{P}_{2n-1}$, the rule (1) is the *Gaussian* quadrature formula. In that case, the nodes x_k are zeros of the monic orthogonal polynomial $\pi_n(w;x)$ and the corresponding weights A_k (Christoffel numbers) can be expressed by the so-called Christoffel function $\lambda_n(w;x)$ (cf. [12, Chapters 2 & 5]) in the form $A_k = \lambda_n(w;x_k) > 0$, $k = 1,\ldots,n$. Positivity of Christoffel numbers is very important for the convergence of the quadrature formulas. In the special case $w(x) = 1$ on $[-1,1]$, the nodes x_k are zeros of the Legendre polynomial $P_n(x)$. It was originally discovered by Gauss in 1814, of course, without theory of orthogonality.

As we know [12, Chapters 2], the (monic) polynomials $\pi_n(w;x)$ orthogonal with respect to the weight function $w(x)$ on $[a,b]$ satisfy the three-term recurrence equation

$$\begin{aligned} &\pi_{k+1}(t) = (t-\alpha_k)\pi_k(t) - \beta_k\pi_{k-1}(t), \qquad k = 0,1,2,\ldots, \\ &\pi_0(t) = 0, \;\; \pi_{-1}(t) = 0, \end{aligned} \tag{2}$$

where $(\alpha_k) = (\alpha_k(w))$ and $(\beta_k) = (\beta_k(w))$ are sequences of recursion coefficients. The coefficient β_0 which is multiplied by $\pi_{-1}(x) = 0$ in the recurrence relation (2) may be arbitrary, but it is convenient to define it by $\beta_0 = \mu_0 = \int_a^b w(x)\,dx$.

For generating Gaussian quadrature rules there are numerical methods, which are computationally much better than a computation of nodes by using Newton's method and then a direct application of the classical Christoffel's expressions for the weights (see e.g. Davis

and Rabinowitz [3]). The characterization of the Gaussian quadratures via an eigenvalue problem for the Jacobi matrix

$$J_n(w) = \begin{bmatrix} \alpha_0 & \sqrt{\beta_1} & & & \mathrm{O} \\ \sqrt{\beta_1} & \alpha_1 & \sqrt{\beta_2} & & \\ & \sqrt{\beta_2} & \alpha_2 & \ddots & \\ & & \ddots & \ddots & \sqrt{\beta_{n-1}} \\ \mathrm{O} & & & \sqrt{\beta_{n-1}} & \alpha_{n-1} \end{bmatrix} \tag{3}$$

has become the basis of current methods for generating these quadratures. The most popular of them is one due to Golub and Welsch [6]. Their method is based on determining the eigenvalues and the first components of the eigenvectors of a symmetric tridiagonal Jacobi matrix (3), where α_ν and β_ν, $\nu = 0, 1, \ldots, n-1$, are the coefficients in the three-term recurrence relation (2) for the monic orthogonal polynomials $\pi_\nu(w;\cdot)$. Namely, *the nodes x_k in the Gaussian quadrature rule* (1)*, with respect to the weight function $w(x)$ on $[a,b]$, are the eigenvalues of the n-th order Jacobi matrix* (3)*. The weights A_k are given by*

$$A_k = \beta_0 v_{k,1}^2, \qquad k = 1, \ldots, n,$$

where $\beta_0 = \mu_0 = \int_a^b w(x)\,dx$ and $v_{k,1}$ is the first component of the normalized eigenvector $\mathbf{v}_k$ corresponding to the eigenvalue x_k,

$$J_n(w)\mathbf{v}_k = x_k\mathbf{v}_k, \qquad \mathbf{v}_k^{\mathrm{T}}\mathbf{v}_k = 1, \qquad k = 1, \ldots, n.$$

Simplifying QR algorithm so that only the first components of the eigenvectors are computed, Golub and Welsch [6] gave an efficient procedure for constructing the Gaussian quadrature rules. This procedure was implemented in several programming packages including our package `OrthogonalPolynomials` realized in `Mathematica` [2].

Thus, we need the recursion coefficients α_k and β_k, $k \le N-1$, for the monic polynomials $\pi_\nu(w;\cdot)$, in order to construct the n-point Gauss-Christofell quadrature formula, with respect to the weighte $w(x)$, for each $n \le N$. These coefficients are known explicitly for the classical orthogonal polynomials (see [12, Chapters 2]). In other cases we need an additional numerical construction of recursion coefficients, using the method of moments or the so-called discretized Stieltjes procedure (see [12, § 2.4.8]).

2.2. Gaussian formulas for the weight $w(x) = (1-x)^\alpha x^\beta \log(1/x)$

We consider the n-point quadrature formula

$$\int_0^1 f(x)(1-x)^\alpha x^\beta \log\frac{1}{x}\,dx = \sum_{k=1}^{n} A_k f(x_k) + R_n(f), \tag{4}$$

with parameters $\alpha, \beta > -1$ in the weight function $w(x) = (1-x)^\alpha x^\beta \log(1/x)$. Piessens and Branders [19] considered cases when $\alpha = 0$ and $\beta = 0, \pm 1/2, \pm 1/3, -1/4, -1/5$ (see also Gautschi [4] and [5]). Quadrature parameters for $n \le 8$ was given in Katsikadelis [9, pp. 297–298] in the case $\alpha = \beta = 0$.

Using symbolic integration we find the moments $\mu_k = \mu_k(\alpha,\beta)$ in terms of the gamma function and harmonic numbers,

$$\mu_k(\alpha,\beta) = \int_0^1 x^k w(x)\,dx = \int_0^1 (1-x)^\alpha x^{k+\beta} \log\frac{1}{x}\,dx$$

$$= \frac{\Gamma(\alpha+1)\Gamma(\beta+k+1)}{\Gamma(\alpha+\beta+k+2)}\,[H(\alpha+\beta+k+1)-H(\beta+k)]\,. \qquad (5)$$

For example, for $\alpha=\beta=0$ it reduces to $\mu_k(0,0)=1/(k+1)^2$, $k\geq 0$.

The standard meaning of the k-th harmonic number H_k is the sum of the reciprocals of the first k natural numbers, i.e.,

$$H_k = H(k) = \sum_{\nu=1}^{k} \frac{1}{\nu}\,,$$

and its representation is given by Euler in the form

$$H(k) = \int_0^1 \frac{1-t^k}{1-t}\,dt = \sum_{\nu=1}^{k} (-1)^{\nu-1}\frac{1}{\nu}\binom{k}{\nu}.$$

Taking a fractional argument x between 0 and 1, the harmonic number $H(x)$ is defined by the previous integral, where k is simply replaced by x. Then it can be generated by $H(x)=H(x-1)+x^{-1}$ or

$$H(1-x)-H(x) = \pi\cot(\pi x) - \frac{1}{x} + \frac{1}{1-x}.$$

More generally, for every $x>0$ (integer or not), the harmonic number is determined by

$$H(x) = x\sum_{k=1}^{+\infty}\frac{1}{k(x+k)} = \psi(x+1)+\gamma,$$

where $\psi(x)=\Gamma'(x)/\Gamma(x)$ is the so-called *digamma* function, i.e., the logarithmic derivative of the gamma function $\Gamma(x)$ and $\gamma=0.577215664901532\ldots$ is the Euler-Mascheroni constant.

Using the `Mathematica` package `OrthogonalPolynomials` [2] and the first $2N$ moments μ_k, $k=0,1,\ldots,2N-1$, given by (5), we get the first N coefficients α_k and β_k, $k=0,1,\ldots,N-1$, in the recurrence relation (2). It enables us to obtain quadrature parameters in (4) for any $n\leq N$.

Remark. In order to overcome the severe ill-conditioning in obtaining the recursion coefficients with a satisfactory accuracy, a multi-precision arithmetic can be used. For example, in the simplest case $\alpha=\beta=0$, taking 55-decimal-digit arithmetic we get the first $N=50$ recursion coefficients to about 20 decimal digits.

The following code in the `Mathematica` package `OrthogonalPolynomials` [2] generates recursion coefficients for $k\leq 2N-1=99$ and quadrature parameters (nodes and weights) to 20 decimal digits for $n=10(10)50$:

```
In[1]:= << orthogonalPolynomials`

In[2]:= w[t_, a_, b_] := (1 - t)^a t^b Log[1 / t]

In[3]:= mom = Integrate[t^k w[t, 0, 0], {t, 0, 1}]; moments = Table[mom, {k, 0, 99}];

In[4]:= {alpha, beta} = aChebyshevAlgorithm[moments, WorkingPrecision → 55];

In[5]:= param = Table[aGaussianNodesWeights[n, alpha, beta,
          Precision → 20, WorkingPrecision → 20], {n, 10, 50, 10}];
```

For example, the obtained nodes and weights for $n=10$ are given in the following list:

```
In[6]:= param[[1]]

Out[6]= {{0.009042630962199650 6369, 0.053971266222500629504,
    0.13531182463925077487, 0.24705241628715982422, 0.38021253960933233397,
    0.52379231797184320116, 0.66577520551642459722, 0.79419041601196621736,
    0.89816109121900353817, 0.96884798871863353939},
   {0.12095513195457051499, 0.18636354256407187033, 0.19566087327775998271,
    0.17357714218290692084, 0.13569567299548420167, 0.09364675853811052598 7,
    0.05578727351415874076, 0.02715981089923333 1146,
    0.00951518260284851499 3, 0.00163815763359826 32549}}
```

Example 1. Consider

$$I = \int_0^1 \frac{(1-x)^{-1/2}x^{-1/2}\log(1/x)}{\sqrt{1+x}}\,dx, \tag{6}$$

which value is known (cf. [5])

$$I = \frac{\sqrt{2\pi}}{8}\Gamma\Big(\frac{1}{4}\Big)^2 = 4.11871837492687201436674 0\ldots$$

By the linear transformation $2x-1=t$, this integral reduces to

$$I = \int_{-1}^1 \sqrt{\frac{2}{3+t}}\log\frac{2}{1+t}\frac{dt}{\sqrt{1-t^2}}.$$

An application of the standard Gauss-Legendre quadrature gives a very slow convergence. Realtive errors $r_n(\mathrm{GL})$ for $n = 10(10)100$ are presented in Table 1. Numbers in parentheses denote decimal exponents. Slightly better results can be obtained by using Gauss-Chebyshev quadratures with respect to the weight function $w(t) = (1-t^2)^{-1/2}$. The corresponding relative errors $r_n(\mathrm{GC})$ are also displayed in the same table.

However, we can directly apply the quadrature formula (4) to integral (6). Let

$$Q_n^{(\alpha,\beta)} = \sum_{k=1}^n A_k f(x_k) \quad \text{and} \quad r_n^{(\alpha,\beta)} = |(Q_n^{(\alpha,\beta)} - I)/I|.$$

Taking the quadrature formula with the logarithmic weight $w(x) = \log(1/x)$, the corresponding function in (6) is $f(x) = 1/\sqrt{x(1-x^2)}$. The convergence of this rule is again very slow. Relative errors $r_n^{(0,0)}$ are given in Table 1.

But, if we include also algebraic singularities in the weight, i.e., if we take $w(x) = (1-x)^{-1/2}x^{-1/2}\log(1/x)$ ($\alpha=\beta=-1/2$), the convergence becomes very fast. Gaussian approximations $Q_n^{(-1/2,-1/2)}$ and relative errors are given in the second part of Table 1 for small values of $n \le 10$. Incorrect decimal digits are underlined. As we can see, 17 exact decimal digits are obtained using Gaussian rule with only $n = 10$ digits.

The same method enables us to include also a logarithmic singularity at $x = 0$. Thus, we can consider the weight function

$$w(x) = w^{(\alpha,\beta)}(x) = (1-x)^\alpha x^\beta \log\frac{1}{x(1-x)}, \quad \alpha,\beta > -1.$$

In Fig. 1 we present this weight function for $\alpha = 0$ and three selected values of the parameter β.

Table 1. Relative errors of quadrature sums for $n = 10(10)100$ and Gaussian approximations with respect to logarithmic weight and the corresponding relative errors for $n = 1(1)10$

n	$r_n(\mathrm{GL})$	$r_n(\mathrm{GC})$	$r_n^{(0,0)}$	n	$Q_n^{(-1/2,-1/2)}$	$r_n^{(-1/2,-1/2)}$
10	1.84(−1)	5.29(−2)	1.42(−1)	1	4.0801983843688532	9.35(−3)
20	1.08(−1)	2.64(−2)	8.69(−2)	2	4.1179039770237825	1.98(−4)
30	7.80(−2)	1.76(−2)	6.41(−2)	3	4.1186986430715864	4.79(−6)
40	6.17(−2)	1.32(−2)	5.14(−2)	4	4.1187178694526636	1.23(−7)
50	6.17(−2)	1.06(−2)	4.31(−2)	5	4.1187183615750484	3.24(−9)
60	5.14(−2)	8.81(−3)	3.73(−2)	6	4.1187183745672496	8.73(−11)
70	4.41(−2)	7.55(−3)	3.30(−2)	7	4.1187183749170540	2.38(−12)
80	3.88(−2)	6.61(−3)	2.96(−2)	8	4.1187183749266013	6.57(−14)
90	3.47(−2)	5.87(−3)	2.69(−2)	9	4.1187183749268644	1.83(−15)
100	2.87(−2)	5.29(−3)	2.47(−2)	10	4.1187183749268718	5.10(−17)

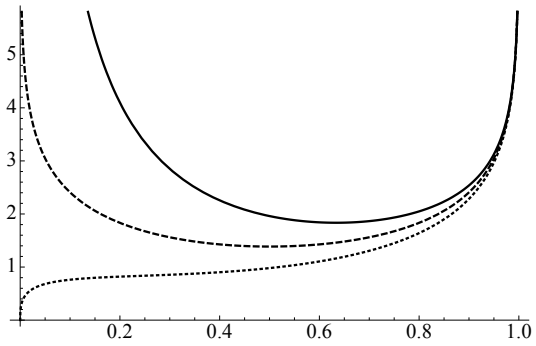

Figure 1. Graphs of the weight functions $w(x)$ for $\alpha = 0$ and $\beta = -1/2$ (solid line), $\beta = 0$ (dashed line) and $\beta = 1/2$ (dotted line).

Similarly as before we f nd the corresponding moments

$$\mu_k(\alpha,\beta) = \int_0^1 (1-x)^\alpha x^{k+\beta} \log\frac{1}{x(1-x)}\,dx$$

$$= \frac{\Gamma(\alpha+1)\Gamma(\beta+k+1)}{\Gamma(\alpha+\beta+k+2)}\,[2H(\alpha+\beta+k+1) - H(\beta+k) - H(\alpha)].$$

Example 2. For $\alpha = -1/4$ and $\beta = -1/2$ compute

$$I_k = \int_{-1}^1 f_k(x) w^{(\alpha,\beta)}(x)\,dx \approx Q_n^{(\alpha,\beta)}(f_k), \qquad k = 1,2,$$

where $f_1(t) = \sin(10\pi x)$ and $f_2(t) = \sin(20\pi x^2)$.

As before, by using the `Mathematica` package `OrthogonalPolynomials` [2] we obtain recursion coeff cients and parameters of the Gaussian rules with respect to the weight $w^{(-1/4,-1/2)}(x)$, and then we apply them to given integrals.

In the f rst case we get results presented in Table 2, including the corresponding relative errors. Incorrect decimal digits are underlined.

Table 2. Gaussian quadrature sums $Q_n^{(-1/4,-1/2)}(f_k)$, with corresponding relative errors $r_n(f_k)$, $k=1,2$

n	$Q_n^{(-1/4,-1/2)}(f_1)$	$r_n(f_1)$	$Q_n^{(-1/4,-1/2)}(f_2)$	$r_n(f_2)$
10	0.5022466846173798	5.53(−2)		
20	0.5316431444014815	3.32(−13)		
30	0.5316431444016578	2.88(−29)	0.446652403036681062 22	6.99(−5)
40			0.4466212016 9680683776	3.43(−11)
50			0.446621201681477912 72	1.14(−19)
60			0.4466212016814779126 7	2.06(−29)

Grapfs of the second function $f_2(x)$ and the integrand $F_2(x) = f_2(x)w^{(-1/4,-1/2)}(x)$ are displayed in Fig. 2. Because of oscillatory integrand we need more nodes in integration and therefore we start with $n = 30$ points. Results are given in the same table.

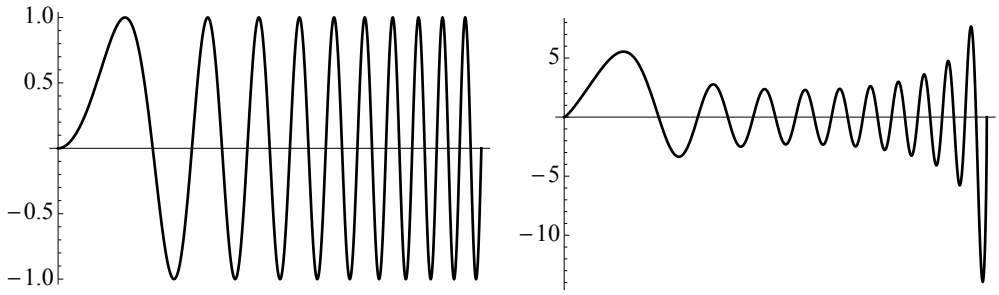

Figure 2. Graphs of functions $f_2(x) = \sin(20\pi x^2)$ (left) and $F_2(x) = f_2(x)w^{(-1/4,-1/2)}(x)$ (right).

3. Some Remarks on Gaussian Quadrature Rules for Müntz Systems

Gaussian integration can be extended in a natural way to non-polynomial functions, taking a system of linearly independent functions

$$\{P_0(x), P_1(x), P_2(x), \ldots\} \qquad (x \in [a,b]), \tag{7}$$

usually chosen to be complete in some suitable space of functions. If $w(x)$ is a given nonnegative weight on $[a,b]$ and the quadrature rule

$$\int_a^b f(x)w(x)\,dx = \sum_{k=1}^{n} A_k f(x_k) + R_n(f) \tag{8}$$

is such that it integrates exactly the first $2n$ functions in (7), we call the rule (8) as *Gaussian with respect to the system* (7). The existence and uniqueness of a Gaussian quadrature rule (8) with respect to the system (7), or shorter a *generalized Gaussian formula*, is always guaranteed if the first $2n$ functions of this system constitute a Chebyshev system on $[a,b]$. Then, all the weights $A_1, \ldots, A_n$ in (8) are positive.

The generalized Gaussian quadratures for Müntz systems goes back to Stieltjes [20] in 1884. Taking $P_k(x) = x^{\lambda_k}$ on $[a,b] = [0,1]$, where $0 \leq \lambda_0 < \lambda_1 < \cdots$, Stieltjes showed the existence of Gaussian formulae.

A numerical algorithm for constructing the generalized Gaussian quadratures was investigated by Ma, Rokhlin and Wandzura [11], but their algorithm is ill conditioned (see [11, Remark 6.2]). In [15], Milovanović and Cvetković presented an alternatively numerical method for constructing the generalized Gaussian quadrature (8) for Müntz polynomials, which is exact for each $f \in M_{2n-1}(\Lambda) = \operatorname{span}\{x^{\lambda_0}, x^{\lambda_1}, \ldots, x^{\lambda_{2n-1}}\}$. The method is rather stable and simpler than the previous one, since it is based on construction and stable computation of orthogonal Müntz systems, previously developed in [13]. The method performs calculations in double precision arithmetics in order to get double precision results. For details see [15]. An application in numerical inversion of the Laplace transform was given in [16].

Some transformation methods for integrals with Müntz polynomials can be found in [14] and [10].

4. Conclusion

In this paper we propose a method for construction weighted Gaussian quadrature rules for integrals with algebraic and/or logarithmic singularities, which appear in many applications of BEM and FEM in computational problems in engineering. Also we give some remarks on generalized Gaussian formulas for Müntz systems.

Acknowledgement. The authors were supported in part by the Serbian Ministry of Education and Science.

References

[1] Brebbia C A and Dominguez J (1998) *Boundary Elements: An Introductory Course*, Second Edition, WIT Press, Boston.

[2] Cvetković A S and Milovanović G V (2004) The Mathematica Package "OrthogonalPolynomials", *Facta Univeritatis Series Mathematics & Informatics*, **19**, pp. 17–36.

[3] Davis P J and Rabinowitz P (1984) *Methods of Numerical Integration* (2nd edn.), Computer Science and Applied Mathematics, Academic Press Inc., Orlando, FL.

[4] Gautschi W (1990) Computational aspects of orthogonal polynomials, *Orthogonal Polynomials (Columbus, OH, 1989)*, P. Nevai (Ed.), pp. 181–216, NATO Adv. Sci. Inst. Ser. C: Math. Phys. Sci., 294, Kluwer, Dordrecht.

[5] Gautschi W (2010) Gauss quadrature routines for two classes of logarithmic weight functions, *Numerical Algorithms*, **55**, pp. 265–277.

[6] Golub G H and Welsch J H (1969) Calculation of Gauss quadrature rules, *Mathematics of Computation*, **23**, pp. 221–230.

[7] Johnston P R and Elliott D (2005) A sinh transformation for evaluating nearly singular boundary element integrals, *International Journal for Numerical Methods in Engineering*, **62**, pp. 564–578.

[8] Johnston B M, Johnston P R, and Elliott D (2007) A sinh transformation for evaluating two-dimensional nearly singular boundary element integrals, *International Journal for Numerical Methods in Engineering*, **69**, pp. 1460–1479.

[9] Katsikadelis J T (2002) *Boundary Elements: Theory and Applications*, Elsevier, Amsterdam.

[10] Lombardi G (2009) Design of quadrature rules for Müntz and Müntz-logarithmic polynomials using monomial transformation, *International Journal for Numerical Methods in Engineering*, **80**, pp. 1687–1717.

[11] Ma J, Rokhlin V, and Wandzura S (1996) Generalized Gaussian quadrature rules for systems of arbitrary functions, *SIAM Journal on Numerical Analysis*, **33**, pp. 971–996.

[12] Mastroianni G and Milovanović G V (2008) *Interpolation Processes – Basic Theory and Applications*, Springer Monographs in Mathematics, Springer – Verlag, Berlin – Heidelberg.
[13] Milovanović G V (1999) Müntz orthogonal polynomials and their numerical evaluation, *Applications and Computation of Orthogonal Polynomials*, W Gautschi, G H Golub, and G Opfer (Eds.), pp. 179–202, ISNM, Vol. 131, Birkhäuser, Basel.
[14] Milovanović G V and Cvetković A S (2002) Numerical integration of functions with logarithmic end point singularity, *Facta Univeritatis Series Mathematics & Informatics*, **17**, pp. 57–74.
[15] Milovanović G V and Cvetković A S (2005) Gaussian type quadrature rules for Müntz systems, *SIAM Journal on Scientific Computing* **27**, pp. 893–913.
[16] Milovanović G V and Cvetković A S (2005) Numerical inversion of the Laplace transform, *Facta Univeritatis Series Electronics & Energetics*, **18**, pp. 515–530.
[17] Milovanović G V and Velicković D M (2001) Quadrature processes for several types of quasi-singular integrals appearing in the electromagnetic f eld problems, *5th Intern. Conf. Applied Electromagnetics PES 2001, Proceedings of Full Papers (Niš, 2001)*, D M Velicković, (Ed.), pp. 117–122, Faculty of Electronic Engineering, Niš.
[18] Oliveira S P, Madureira A L, and Valentin F (2009) Weighted quadrature rules for f nite element methods, *Journal of Computational and Applied Mathematics*, **227**, pp. 93–101.
[19] Piessens R and Branders M (1975) *Tables of Gaussian Quadrature Formulas*, University of Leuven, Leuven.
[20] Stieltjes T J (1884) Sur une généralisation de la théorie des quadratures mécaniques, *Comptes Rendus Mathématique, Académie des Sciences, Paris*, **99**, pp. 850–851.

CRITERIA OF ELASTIC STABILITY FOR PLATE WITH GEOMETRIC DISCONTINUITY

Snežana N. Mitić

Faculty of Mechanical Engineering,
The University of Niš, Aleksandra Medvedeva 14, 18000 Niš
e-mail: snemitic@gmail.com

Abstract. This paper presents stability criteria for rectangular plates subjected to loads along constructive discontinuity and along the two edges. In its mid-plane, the plate is loaded with uniformly distributed forces along two opposing plate edges and along constructive discontinuity. The constructive discontinuity divides the plate into subplates of different thickness. The subplates are isotropic and have a common elastic surface area. The Morris-Levy method has been used to solve the stability problem. Each subplate buckling problem is separately solved and the solutions are brought together by matching the continuity equations. The plate has two opposite edges simply supported while the other two edges can take any combination of free, simply supported and clamped conditions. For different boundary conditions, the buckling solutions comprise of different combinations. For each boundary condition, the correct solution combination depends on the discontinuity load to the edges load ratio. The analysis of stability has been performed according to the basic postulates of the elastic stability theory. Fourth-order type ordinary linear differential equations with constant coefficients are derived from partial differential equations of the elastic surface areas of the buckled subplates. The buckling factor, which depends on the plate geometry, its mechanical properties and loads, is obtained from the derived system of equations.

1. Introduction

The elastic buckling problem of rectangular plates under uniaxial loads acting at opposite edges is the most basic plate buckling problem and its solution is documented in all standard texts on plate buckling [1]. A theoretical analysis of the stability of plates with fields of non-uniform thickness is employed in practical engineering designs. Researchers have investigated various forms of thickness variations of the plate that include: a linear function along one direction [2]; a non-linear function along one direction [3] or in both directions [4]. Piecewise constant step functions in one direction are considered in references [5, 6], and in both directions in references [7]. The paper [8] considered stability criteria for rectangular plates subjected to intermediate and end in-plane loads. The subplates are of uniform thickness. Unlike [8], this paper will focus on subplates with different thickness. Subplates are isotropic and have a common elastic surface area. The resultant buckling problem can then be solved in the exact manner to yield the stability criteria that are functions of the position of the discontinuity and the relative ratio of the loads along discontinuity and edges. The Morris-Levy method has been used to solve the stability problem.

Plates with constructive discontinuity and fields of non-uniform thickness are extensively used in modern structures. By using such plates, it is possible to obtain material saving,

weight reduction, stiffness enhancing, designated strengthening, fundamental vibration frequency increasing, etc.

2. Problem definition

Consider an isotropic, elastic, rectangular thin plate of length *a*, width *b*, different thickness h_1 and h_2, modulus of elasticity *E*, Poisson's ratio ν. The origin of the coordinate system is set at the upper left-hand side corner of the plate, as shown in Fig. 1. The plate is subjected to an end compressive load N_{x_1} at the edge *x*=0, and a geometric discontinuity compressive load N_{x_2} at a location $x = \xi a$, $0 \le \xi \le 1$, from the *y*-axis. The plate is simply supported along two opposite edges that are parallel to the *x* axis. The other two edges can be free, simply supported, or clamped. The problem at hand is to determine the critical buckling loads.

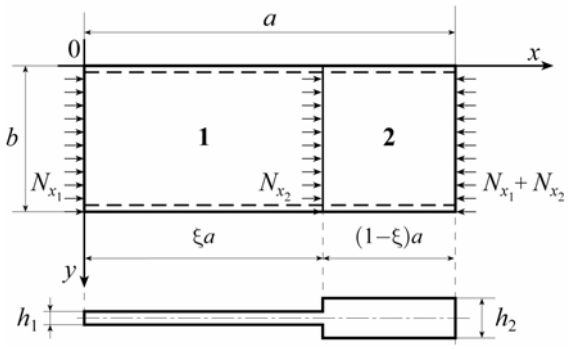

Figure 1. Geometry and coordinate systems for a rectangular plate subjected to loads

The plate can be decomposed into two subplates along the line at $x = \xi a$. The geometric discontinuity divides the plate into subplates of different thickness h_1 and h_2. The subplates are isotropic and have a common elastic surface area. Based on the classical thin plate theory, the governing differential equation for the i^{th} subplates is given by [1]

$$\frac{\partial^4 w_i}{\partial x^4} + 2\frac{\partial^4 w_i}{\partial x^2 \partial y^2} + \frac{\partial^4 w_i}{\partial y^4} = -\frac{N_i}{D_i}\frac{\partial^2 w_i}{\partial x^2}, \tag{1}$$

$$N_i = \begin{cases} N_{x_1}, & i = 1 \\ N_{x_1} + N_{x_2}, & i = 2 \end{cases}, \tag{2}$$

in which the subscript i =1,2 refers to the i^{th} subplate; $w_i(x,y)$ is transverse displacement; *x* and *y* are Cartesian coordinates; N_i is plane compressive load associated with the i^{th} subplate; D_i is flexural rigidity of the subplate **1** and **2** given by: .

$$D_1 = \frac{E h_1^3}{12\left(1-\nu^2\right)}, \tag{3}$$

$$D_2 = \frac{E h_2^3}{12\left(1-\nu^2\right)}. \tag{4}$$

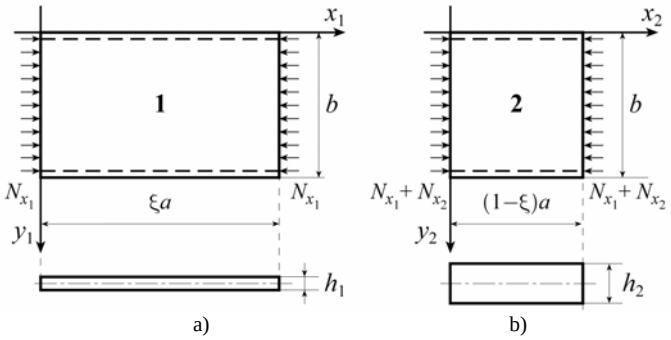

Figure 2. . Geometry and coordinate systems for a rectangular plate subjected to loads. (a) subplate 1; and (b) subplate 2.

3. Analytical modeling for subplate 1

Based on the classical thin plate theory, the governing differential equation for the subplate **1** is given by Eq. (1) for *i*=1 and can be rewritten as

$$\frac{\partial^4 w_1}{\partial x_1^4} + 2\frac{\partial^4 w_1}{\partial x_1^2 \partial y_1^2} + \frac{\partial^4 w_1}{\partial y_1^4} = -\frac{N_{x_1}}{D_1}\frac{\partial^2 w_1}{\partial x_1^2}. \tag{5}$$

Using the following transformations:

$$\overline{w}_1 = \frac{w_1}{b}, \quad \overline{x}_1 = \frac{x_1}{\xi a}, \quad \overline{y}_1 = \frac{y_1}{b}, \quad \theta = \frac{a}{b}, \tag{6}$$

the differential Eq. (5) of the deflection surface can be written in the following form:

$$\frac{\partial^4 \overline{w}_1}{\partial \overline{x}_1^4} + 2\xi^2\theta^2\frac{\partial^4 \overline{w}_1}{\partial \overline{x}_1^2 \partial \overline{y}_1^2} + \xi^4\theta^4\frac{\partial^4 \overline{w}_1}{\partial \overline{y}_1^4} + K_1\pi^2\xi^2\theta^2\frac{\partial^2 \overline{w}_1}{\partial \overline{x}_1^2} = 0, \tag{7}$$

where K_1 is the buckling factor for subplate and which, for certain materials and load, depends on the dimensions of the plate.

$$K_1 = \frac{N_{x_1}}{D_1}\frac{b^2}{\pi^2}. \tag{8}$$

By using the Levy approach, solution of differential equations for the subplate **1** can be expressed as:

$$\overline{w}_1\left(\overline{x}_1,\overline{y}_1\right)= f_1\left(\overline{x}_1\right)\sin\beta_n\overline{y}_1,\qquad \beta_n = n\pi \tag{9}$$

where n (=1, 2, ...) is the number of half waves of the buckling mode in the y direction and $f_1\left(\overline{x}_1\right)$ is an unknown function to be determined. Eq. (9) satisfies the boundary conditions for two simply supported edges.

The essential and natural boundary conditions for the two simply supported edges at $\overline{y}_1 = 0$ and $\overline{y}_1 = 1$, associated with the subplate **1** are given by

$$\overline{w}_1\left(\overline{x}_1,\overline{y}_1\right)_{\overline{y}_1=0,1} = 0 \tag{10}$$

$$\left[\frac{\partial^2\overline{w}_1\left(\overline{x}_1,\overline{y}_1\right)}{\partial\overline{y}_1^{\,2}}+\frac{\nu}{\xi^2\theta^2}\frac{\partial^2\overline{w}_1\left(\overline{x}_1,\overline{y}_1\right)}{\partial\overline{x}_1^{\,2}}\right]_{\overline{y}_1=0,1} = 0 \tag{11}$$

The transverse displacement given in Eq. (9) satisfies the boundary conditions of the two parallel simply supported edges [Eq. (10) and (11)]. In view of Eq. (9), the partial differential equations may be reduced to fourth-order ordinary differential equations as

$$f_1^{(4)}\left(\overline{x}_1\right)-2\xi^2\theta^2\beta_n^2 f_1''\left(\overline{x}_1\right)+\xi^4\theta^4\beta_n^4 f_1\left(\overline{x}_1\right)+K_1\pi^2\xi^2\theta^2 f_1''\left(\overline{x}_1\right)=0. \tag{12}$$

The buckling of subplate **1** in the direction of the x axis is determined by the functions $f_1\left(\overline{x}_1\right)$ which is represented in the form

$$f_1\left(\overline{x}_1\right)= A_1 e^{\lambda\overline{x}_1} \tag{13}$$

Based on Eq. (13), Eq. (12), the characteristics equation for subplate **1** is derived

$$\lambda^4+\left(K_1\pi^2\xi^2\theta^2-2\xi^2\theta^2\beta_n^2\right)\lambda^2+\xi^4\theta^4\beta_n^4=0. \tag{14}$$

Introduce a label $\gamma_1 = K_1\pi^2\xi^2\theta^2$, equation (14) becomes:

$$\lambda^4+\left(\gamma_1-2\xi^2\theta^2\beta_n^2\right)\lambda^2+\xi^4\theta^4\beta_n^4=0. \tag{15}$$

Depending on the roots of the characteristics equations of the differential equations, there are five general solutions to the above fourth-order differential equations as given below.

3.1. Solution A for the case $\gamma_1<0$

The general solution of the differential equation (7) has the form

$$\overline{w}_1 = \left(C_1\sinh\alpha_1\overline{x}_1+C_2\cosh\alpha_1\overline{x}_1+C_3\sinh\beta_1\overline{x}_1+C_4\cosh\beta_1\overline{x}_1\right)\sin\beta_n\overline{y}_1\,. \tag{16}$$

where α_1 and β_1 are the roots of the characteristics equation (15) for condition $\gamma_1<0$:

$$\lambda_{1,2} = \pm\sqrt{-\tfrac{1}{2}\left(\gamma_1-2\xi^2\theta^2\beta_n^2\right)-\tfrac{1}{2}\sqrt{\gamma_1^2-4\xi^2\theta^2\beta_n^2\gamma_1}}\;=\pm\alpha_1\,, \tag{17}$$

$$\lambda_{3,4} = \pm\sqrt{-\tfrac{1}{2}\left(\gamma_1 - 2\xi^2\theta^2\beta_n^2\right) + \tfrac{1}{2}\sqrt{\gamma_1^2 - 4\xi^2\theta^2\beta_n^2\gamma_1}} = \pm\beta_1 . \tag{18}$$

3.2. Solution B for the case γ_1=0

For $\gamma_1 = 0$ the roots of the characteristics Eq. (15) are:

$$\alpha_1 = \beta_1 = \xi\theta\beta_n . \tag{19}$$

General solution of the differential equation for those roots of characteristics equations is:

$$\bar{w}_1 = \left(C_1 \sinh\alpha_1\bar{x}_1 + C_2\bar{x}_1 \sinh\alpha_1\bar{x}_1 + C_3\cosh\alpha_1\bar{x}_1 + C_4\bar{x}_1\cosh\alpha_1\bar{x}_1\right)\sin\beta_n\bar{y}_1 . \tag{20}$$

3.3. Solution C for the case $0 < \gamma_1 < 4\xi^2\theta^2\beta_n^2$

The roots of the characteristics equation (15) are

$$\lambda_{1,2} = \pm\sqrt{\xi^2\theta^2\beta_n^2 - \frac{\gamma_1}{4}} + i\frac{\sqrt{\gamma_1}}{2}, \tag{21}$$

$$\lambda_{3,4} = \pm\sqrt{\xi^2\theta^2\beta_n^2 - \frac{\gamma_1}{4}} - i\frac{\sqrt{\gamma_1}}{2}, \tag{22}$$

where

$$\alpha_1 = \sqrt{\xi^2\theta^2\beta_n^2 - \frac{\gamma_1}{4}}; \quad \beta_1 = \frac{\sqrt{\gamma_1}}{2} \tag{23}$$

The general solution of the differential equation (7) has the form:

$$\begin{aligned}\bar{w}_1 = \big(&C_1 \sinh\alpha_1\bar{x}_1\cos\beta_1\bar{x}_1 + C_2\cosh\alpha_1\bar{x}_1\cos\beta_1\bar{x}_1 + \\ &+C_3\sinh\alpha_1\bar{x}_1\sin\beta_1\bar{x}_1 + C_4\cosh\alpha_1\bar{x}_1\sin\beta_1\bar{x}_1\big)\sin\beta_n\bar{y}_1\end{aligned} . \tag{24}$$

3.4. Solution D for the case $\gamma_1 = 4\xi^2\theta^2\beta_n^2$

The roots of the characteristics equation (15), for this case are:

$$\alpha_1 = \beta_1 = \xi\theta\beta_n \tag{25}$$

The general solution of the differential equation (7) has the form

$$\bar{w}_1 = \left(C_1\cos\alpha_1\bar{x}_1 + C_2\bar{x}_1\cos\alpha_1\bar{x}_1 + C_3\sin\alpha_1\bar{x}_1 + C_4\bar{x}_1\sin\alpha_1\bar{x}_1\right)\sin\beta_n\bar{y}_1 . \tag{26}$$

3.5. Solution E for the case $\gamma_1 > 4\xi^2\theta^2\beta_n^2$

The roots of the characteristics equation (15), for this case are:

$$\lambda_{1,2} = \pm i\sqrt{\tfrac{1}{2}\left(\gamma_1 - 2\xi^2\theta^2\beta_n^2\right) - \tfrac{1}{2}\sqrt{\gamma_1^2 - 4\xi^2\theta^2\beta_n^2\gamma_1}} = \pm i\alpha_1, \tag{27}$$

$$\lambda_{3,4} = \pm i\sqrt{\tfrac{1}{2}\left(\gamma_1 - 2\xi^2\theta^2\beta_n^2\right) + \tfrac{1}{2}\sqrt{\gamma_1^2 - 4\xi^2\theta^2\beta_n^2\gamma_1}} = \pm i\beta_1. \tag{28}$$

The general solution of the differential equation (7) is

$$\overline{w}_1 = \left(C_1\cos\alpha_1\overline{x}_1 + C_2\sin\alpha_1\overline{x}_1 + C_3\cos\beta_1\overline{x}_1 + C_4\sin\beta_1\overline{x}_1\right)\sin\beta_n\overline{y}_1. \tag{29}$$

The constants C_1, C_2, C_3 and C_4 in Eq. (16), (20), (24), (26) and (29) are determined from the boundary conditions along the edges and the continuity conditions along the geometric discontinuity.

4. Analytical modeling for subplate 2

Based on the classical thin plate theory, the governing differential equation for subplate **2** is given by [1]:

$$\frac{\partial^4 w_2}{\partial x_2^4} + 2\frac{\partial^4 w_2}{\partial x_2^2\partial y_2^2} + \frac{\partial^4 w_2}{\partial y_2^4} = -\frac{N_{x_1} + N_{x_2}}{D_2}\frac{\partial^2 w_2}{\partial x_2^2}, \tag{30}$$

where $w_2\left(x_2, y_2\right)$ is the transverse displacement for subplate **2**.
Using the following transformations:

$$\overline{w}_2 = \frac{w_2}{b}, \quad \overline{x}_2 = \frac{x_2}{\left(1-\xi\right)a}, \quad \overline{y}_2 = \frac{y_2}{b}, \quad \theta = \frac{a}{b}, \tag{31}$$

the differential Eq. (30) of the deflection surface can be written in the following form:

$$\frac{\partial^4\overline{w}_2}{\partial\overline{x}_2{}^4} + 2\left(1-\xi\right)^2\theta^2\frac{\partial^4\overline{w}_2}{\partial\overline{x}_2{}^2\partial\overline{y}_2{}^2} + \left(1-\xi\right)^4\theta^4\frac{\partial^4\overline{w}_2}{\partial\overline{y}_2{}^4} + \pi^2\Psi K_1\left(1+\varepsilon\right)\left(1-\xi\right)^2\theta^2\frac{\partial^2\overline{w}_2}{\partial\overline{x}_2{}^2} = 0, \tag{32}$$

where K_2 is the buckling factor for subplate **2**:

$$K_2 = \frac{\left(N_{x_1} + N_{x_2}\right)}{D_2}\frac{b^2}{\pi^2}, \tag{33}$$

and

$$\Psi = \frac{D_1}{D_2} = \left(\frac{h_1}{h_2}\right)^3; \qquad \varepsilon = \frac{N_{x_2}}{N_{x_1}}. \tag{34}$$

By using the Levy approach, solution for differential equation for the subplate **2** can be expressed as:

$$\bar{w}_2(\bar{x}_2,\bar{y}_2) = f_2(\bar{x}_2)\sin\beta_n\bar{y}_2, \qquad \beta_n = n\pi\,. \tag{35}$$

where n (=1, 2, ...) is the number of half waves of the buckling mode in the y direction and $f_2(\bar{x}_2)$ is an unknown function to be determined. Eq. (35) satisfies the boundary conditions for two simply supported edges.

The essential and natural boundary conditions for the two simply supported edges at $\bar{y}_1 = 0$ and $\bar{y}_1 = 1$, associated with the subplate **2** are given by

$$\bar{w}_2(\bar{x}_2,\bar{y}_2)_{\bar{y}_2=0,1} = 0\,, \tag{36}$$

$$\left[\frac{\partial^2\bar{w}_2(\bar{x}_2,\bar{y}_2)}{\partial\bar{y}_2{}^2} + \frac{\nu}{(1-\xi)^2\theta^2}\frac{\partial^2\bar{w}_2(\bar{x}_2,\bar{y}_2)}{\partial\bar{x}_2{}^2}\right]_{\bar{y}_2=0,1} = 0\,. \tag{37}$$

The transverse displacement given in Eq. (35) satisfies the boundary conditions of the two parallel simply supported edges [Eq. (36) and (37)]. In view of Eq. (35), the partial differential equations in Eq. (32) may be reduced to fourth-order ordinary differential equations as

$$f_2^{(4)}(\bar{x}_2) - 2(1-\xi)^2\theta^2\beta_n^2 f_2''(\bar{x}_2) + (1-\xi)^4\theta^4\beta_n^4 f_2(\bar{x}_2) + \pi^2\Psi K_1(1+\kappa)\xi^2\theta^2 f_2''(\bar{x}_2) = 0. \tag{38}$$

The buckling of subplate **2** in the direction of the x axis is determined by the functions $f_2(\bar{x}_2)$ which is represented in the form

$$f_2(\bar{x}_2) = A_2 e^{\lambda'\bar{x}_2} \tag{39}$$

The characteristics equation for subplate **2** is derived

$$(\lambda')^4 + \left[\pi^2\Psi K_1(1+\Psi)(1-\xi)^2\theta^2 - 2(1-\xi)^2\theta^2\beta_n^2\right](\lambda')^2 + (1-\xi)^4\theta^4\beta_n^4 = 0. \tag{40}$$

Introduce a label

$$\gamma_2 = \pi^2\Psi(1+\varepsilon)(1-\xi)^2\theta^2 K_1 \tag{41}$$

equation (40) becomes

$$(\lambda')^4 + \left[\gamma_2 - 2(1-\xi)^2\theta^2\beta_n^2\right](\lambda')^2 + (1-\xi)^4\theta^4\beta_n^4 = 0. \tag{42}$$

Depending on the roots of the characteristics equations of the differential equations, there are five general solutions to the above fourth-order differential equations as given below.

4.1. Solution A for the case $\gamma_2<0$

The general solution of the differential equation (32) has the form

$$\bar{w}_2 = \left(C_5 \sinh \alpha_2 \bar{x}_2 + C_6 \cosh \alpha_2 \bar{x}_2 + C_7 \sinh \beta_2 \bar{x}_2 + C_8 \cosh \beta_2 \bar{x}_2\right) \sin \beta_n \bar{y}_2 \tag{43}$$

where α_1 and β_1 are the roots of the characteristics equation (42) for the condition $\gamma_1<0$:

$$\lambda'_{1,2} = \pm\sqrt{-\tfrac{1}{2}\left(\gamma_2 - 2\left(1-\xi\right)^2 \theta^2 \beta_n^2\right) - \tfrac{1}{2}\sqrt{\gamma_2^2 - 4\left(1-\xi\right)^2 \theta^2 \beta_n^2 \gamma_2}} = \pm\alpha_2 , \tag{44}$$

$$\lambda'_{3,4} = \pm\sqrt{-\tfrac{1}{2}\left(\gamma_2 - 2\left(1-\xi\right)^2 \theta^2 \beta_n^2\right) + \tfrac{1}{2}\sqrt{\gamma_2^2 - 4\left(1-\xi\right)^2 \theta^2 \beta_n^2 \gamma_2}} = \pm\beta_2 . \tag{45}$$

4.2. Solution B for the case $\gamma_2=0$

For $\gamma_2 = 0$ the roots of the characteristics Eq. (42) are:

$$\beta_1 = \alpha_1 = \left(1-\xi\right)\theta\beta_n . \tag{46}$$

The general solution of the differential equation (32) is

$$\bar{w}_2 = \left(C_5 \sinh \alpha_2 \bar{x}_2 + C_6 \bar{x}_2 \sinh \alpha_2 \bar{x}_2 + C_7 \cosh \alpha_2 \bar{x}_2 + C_8 \bar{x}_2 \cos \alpha_2 \bar{x}_2\right) \sin \beta_n \bar{y}_2 . \tag{47}$$

4.3. Solution C for the case $0 < \gamma_2 < 4\left(1-\xi\right)^2 \theta^2 \beta_n^2$

The roots of the characteristics Eq. (42) are:

$$\lambda'_{1,2} = \pm\sqrt{\left(1-\xi\right)^2 \theta^2 \beta_n^2 - \frac{\gamma_2}{4}} + i\frac{\sqrt{\gamma_2}}{2}, \tag{48}$$

$$\lambda'_{3,4} = \pm\sqrt{\left(1-\xi\right)^2 \theta^2 \beta_n^2 - \frac{\gamma_2}{4}} - i\frac{\sqrt{\gamma_2}}{2}, \tag{49}$$

where

$$\alpha_2 = \sqrt{\left(1-\xi\right)^2 \beta_n^2 - \frac{\gamma_2}{4}} \quad ; \qquad \beta_2 = \frac{\sqrt{\gamma_2}}{2} . \tag{50}$$

The general solution of the differential equation (32) for subplate **2** has the form

$$\begin{aligned} \bar{w}_2 = \big(&C_5 \sinh \alpha_2 \bar{x}_2 \cos \beta_2 \bar{x}_2 + C_6 \cosh \alpha_2 \bar{x}_2 \cos \beta_2 \bar{x}_2 + \\ &+ C_7 \sinh \alpha_2 \bar{x}_2 \sin \beta_2 \bar{x}_2 + C_8 \cosh \alpha_2 \bar{x}_2 \sin \beta_2 \bar{x}_2\big) \sin \beta_n \bar{y}_2 \end{aligned} . \tag{51}$$

4.4. Solution D for the case $\gamma_2 = 4\left(1-\xi\right)^2 \theta^2 \beta_n^2$

The general solution of the differential equation (32) for subplate **2** is:

$$\overline{w}_2 = \left(C_5 \cos \beta_2 \overline{x}_2 + C_6 \overline{x}_2 \cos \alpha_2 \overline{x}_2 + C_7 \sin \alpha_2 \overline{x}_2 + C_8 \overline{x}_2 \sin \alpha_2 \overline{x}_2\right) \sin \beta_n \overline{y}_2 , \tag{52}$$

where

$$\beta_2 = \alpha_2 = \left(1-\xi\right)\theta\beta_n . \tag{53}$$

4.5. Solution E for the case $\gamma_2 > 4\left(1-\xi\right)^2 \theta^2 \beta_n^2$

The roots of the characteristics Eq. (42) are:

$$\lambda_{1,2}^{'} = \pm i \sqrt{\frac{1}{2}\left[\gamma_2 - 2\left(1-\xi\right)^2 \theta^2 \beta_n^2\right] - \frac{1}{2}\sqrt{\gamma_2^2 - 4\left(1-\xi\right)^2 \theta^2 \beta_n^2 \gamma_2}} = \pm i\alpha_2 \tag{54}$$

$$\lambda_{3,4}^{'} = \pm i \sqrt{\frac{1}{2}\left[\gamma_2 - 2\left(1-\xi\right)^2 \theta^2 \beta_n^2\right] + \frac{1}{2}\sqrt{\gamma_2^2 - 4\left(1-\xi\right)^2 \theta^2 \beta_n^2 \gamma_2}} = \pm i\beta_2 \tag{55}$$

The general solution of the differential equation (32) has the form:

$$\overline{w}_2 = \left(C_5 \cos \alpha_2 \overline{x}_2 + C_6 \sin \alpha_2 \overline{x}_2 + C_7 \cos \beta_2 \overline{x}_2 + C_8 \sin \beta_2 \overline{x}_2\right) . \tag{56}$$

The constants C_5, C_6, C_7 and C_8 in Eq. (43), (47), (51), (52) and (56) are determined from the boundary conditions along the edges and the continuity conditions along the geometric discontinuity.

The essential and natural boundary conditions of the plate at the edge $\overline{x}_1 = 0$ for simply supported edge are defined as follows:

$$\overline{w}_1\Big|_{\overline{x}_1=0} = 0, \quad \left[\frac{1}{\xi^2\theta^2}\frac{\partial^2 \overline{w}_1}{\partial \overline{x}_1^{\,2}} + \nu \frac{\partial^2 \overline{w}_1}{\partial \overline{y}_1^{\,2}}\right]_{\overline{x}_1=0} = 0 . \tag{57}$$

For a clamped edge natural boundary conditions are defined as follows:

$$\overline{w}_1\Big|_{\overline{x}_1=0} = 0, \qquad \frac{\partial \overline{w}_1}{\partial \overline{x}_1} = 0 . \tag{58}$$

For a free edge boundary conditions are defined:

$$\left[\frac{1}{\xi^2\theta^2}\frac{\partial^2 \overline{w}_1}{\partial \overline{x}_1^{\,2}} + \nu \frac{\partial^2 \overline{w}_1}{\partial \overline{y}_1^{\,2}}\right]_{\overline{x}_1=0} = 0, \quad \left[\frac{1}{\xi^3\theta^3}\frac{\partial^3 \overline{w}_1}{\partial \overline{x}_1^{\,3}} + \frac{2-\nu}{\xi\theta}\frac{\partial^3 \overline{w}_1}{\partial \overline{x}_1 \partial \overline{y}_1^{\,2}} + \frac{\gamma_1}{\xi^3\theta^3}\frac{\partial \overline{w}_1}{\partial \overline{x}_1}\right]_{\overline{x}_1=0} = 0 . \tag{59}$$

The essential and natural boundary conditions of the plate at the edge $\overline{x}_1 = 0$ for simply supported edge are defined as follows:

$$\overline{w}_2\Big|_{\overline{x}_2=1}=0,\quad \left[\frac{1}{\left(1-\xi\right)^2\theta^2}\frac{\partial^2\overline{w}_2}{\partial\overline{x}_2^2}+\nu\frac{\partial^2\overline{w}_2}{\partial\overline{y}_2^2}\right]_{\overline{x}_2=1}=0\,. \tag{60}$$

For a clamped edge natural boundary conditions are defined as follows:

$$\overline{w}_2\Big|_{\overline{x}_2=1}=0,\quad \left[\frac{\partial\overline{w}_2}{\partial\overline{x}_2}\right]_{\overline{x}_2=1}=0\,. \tag{61}$$

For a free edge boundary conditions are defined:

$$\begin{aligned}&\left[\frac{1}{\left(1-\xi\right)^2\theta^2}\frac{\partial^2\overline{w}_2}{\partial\overline{x}_2{}^2}+\nu\frac{\partial^2\overline{w}_2}{\partial\overline{y}_2{}^2}\right]_{\overline{x}_2=1}=0,\\&\left[\frac{1}{\left(1-\xi\right)^3\theta^3}\frac{\partial^3\overline{w}_2}{\partial\overline{x}_2{}^3}+\frac{2-\nu}{\left(1-\xi\right)^2\theta^2}\frac{\partial^3\overline{w}_2}{\partial\overline{x}_2\partial\overline{y}_2{}^2}+\frac{\gamma_2}{\left(1-\xi\right)^3\theta^3}\frac{\partial\overline{w}_2}{\partial\overline{x}_2}\right]_{\overline{x}_2=1}=0\end{aligned} \tag{62}$$

To ensure displacement continuities and equilibrium conditions at the interface of the two subplates, the following essential and natural conditions must be satisfied:

$$\overline{w}_1\big|_{\overline{x}_1=1}=\overline{w}_2\big|_{\overline{x}_2=0} \tag{63}$$

$$\frac{1}{\xi\theta}\frac{\partial\overline{w}_1}{\partial\overline{x}_1}\bigg|_{\overline{x}_1=1}=\frac{1}{\left(1-\xi\right)\theta}\frac{\partial\overline{w}_2}{\partial\overline{x}_2}\bigg|_{\overline{x}_2=0} \tag{64}$$

$$D_1\left[\frac{1}{\xi^2\theta^2}\frac{\partial^2\overline{w}_1}{\partial\overline{x}_1^2}+\nu_1\frac{\partial^2\overline{w}_1}{\partial\overline{y}_1^2}\right]_{\overline{x}_1=1}=D_2\left[\frac{1}{\left(1-\xi\right)^2\theta^2}\frac{\partial^2\overline{w}_2}{\partial\overline{x}_2^2}+\nu_2\frac{\partial^2\overline{w}_2}{\partial\overline{y}_2^2}\right]_{\overline{x}_2=0} \tag{65}$$

$$\begin{aligned}&D_1\left[\frac{1}{\xi^3\theta^3}\frac{\partial^3\overline{w}_1}{\partial\overline{x}_1^3}+\frac{2-\nu}{\xi\theta}\frac{\partial^3\overline{w}_1}{\partial\overline{x}_1\partial\overline{y}_1^2}+\frac{\gamma_1}{\xi^3\theta^3}\frac{\partial\overline{w}_1}{\partial\overline{x}_1}\right]_{\overline{x}_1=1}=\\&D_2\left[\frac{1}{\left(1-\xi\right)^3\theta^3}\frac{\partial^3\overline{w}_2}{\partial\overline{x}_2^3}+\frac{2-\nu_2}{\left(1-\xi\right)\theta}\frac{\partial^3\overline{w}_2}{\partial\overline{x}_2\partial\overline{y}_2^2}+\frac{\gamma_2}{\left(1-\xi\right)^3\theta^3}\frac{\partial\overline{w}_2}{\partial\overline{x}_2}\right]_{\overline{x}_2=0}\end{aligned} \tag{66}$$

When assembling the subplates to form the whole plate via the implementation of the boundary conditions of the plate along the two edges parallel to the y-axis [Eq. (57)–(62)] and the interface conditions between two subplates [Eq. (63)–(66)], a system of homogenous equations is obtained. For a nontrivial solution, the determinant of system must vanish. Each solution combination for the determinant of system is examined. The valid solution combinations should satisfy the following requirements: the buckling loads satisfy the limits of validity for the solution combinations which they belong to; the buckling load factor is the lowest value among possible solutions; the stability curves are continuous.

5. Numerical results

Exact stability criteria are presented graphically in Figs. 3 to 6 for simply supported (SS), and free (FF) plates, respectively.

5.1. SSSS plate

A simply supported rectangular plate (or simply referred to as an SSSS plate) subjected to geometric discontinuity and end inplane loads is first considered. Fig. 3 presents the typical stability criterion curves for SSSS plates. Fig. 3. shows the buckling factor K_1 in the function of the position ξ of the geometric discontinuity for different loads ratio ε (N_{x_2} =const) and h_2/h_1=1.5, θ=1.

With the increase of coordinate ξ, the value of K_1 decreases. For constant position ξ of the geometric discontinuity, the value of K_1 decreases with the increase of loads ratio (N_{x_2} =const, N_{x_1} decreases).

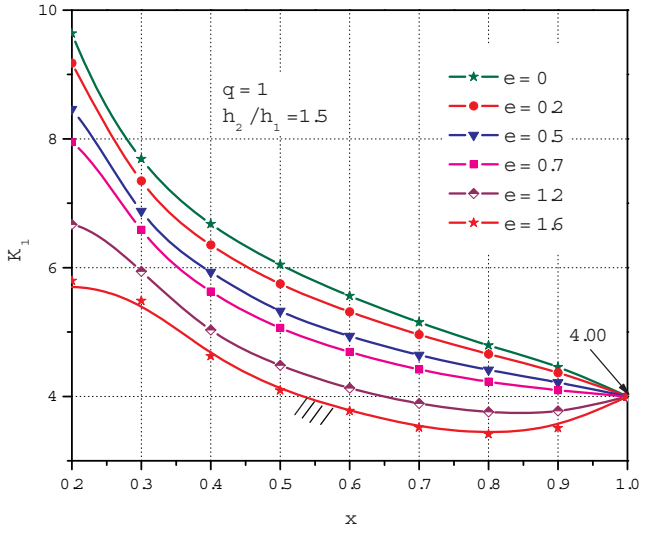

Figure 3. The buckling factor K_1 in the function of the position ξ of the geometric discontinuity for different loads ratio ε for SSSS plate

In Fig. 4. the buckling factor K_2 in the function of loads ratio ε (N_{x_2} =const) for different position ξ of the geometric discontinuity and h_2/h_1=1 is represented. The factor K_2 increases with the increase of loads ratio ε. With the moving of the position of the discontinuity toward higher values, the value of the buckling factor K_2 increases for constant loads ratio ε.

The stability region is bellow the boundary curves.

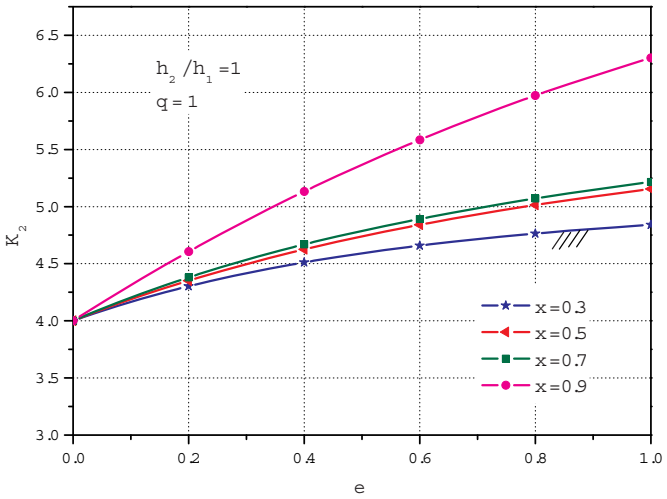

Figure 4. The buckling factor K_2 in the function of loads ratio ε the for different position ξ of the geometric discontinuity for SSSS plate

5.2. FSFS plate

Rectangular plate with the two edges parallel to the x-axis simply supported while the two edges parallel to the y-axis are free (this plate is referred to as a FSFS plate) is consider. The typical stability criterion curve for a FSFS plate. is shown in Fig. 5. Also, Fig. 5. depicts the buckling factor K_1 in the function of the position ξ of the geometric discontinuity for different loads ratio ε. The geometric properties plates are h_2/h_1=1.2 and θ=1. With the moving of the position of the discontinuity toward higher values, the value of the buckling factor K_1 decreases.

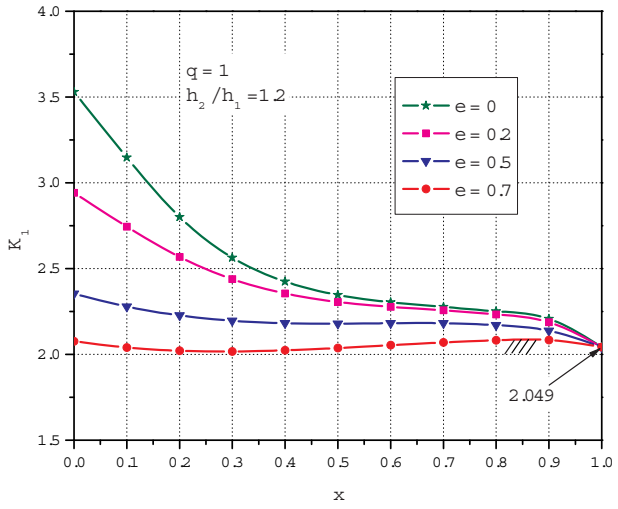

Figure 5. The buckling factor K_1 in the function of the position ξ of the geometric discontinuity for different loads ratio ε for FSFS plate

The buckling factor K_2 in the function of loads ratio ε the for different position ξ of the geometric discontinuity is presented in Fig. 6. Stability region is bellow boundary curves. The value of the buckling factor K_2 increases with the moving of the position of the discontinuity toward higher values.

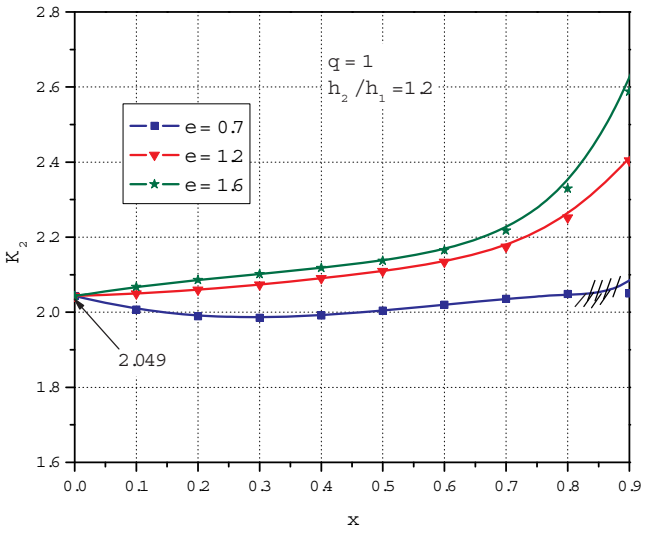

Figure 6. The buckling factor K_2 in the function of loads ratio ε the for different position ξ of the geometric discontinuity for FSFS plate

6. Conclusion

This paper is concerned with the elastic buckling of rectangular plates subjected to both geometric discontinuity and end uniaxial loads. The stability of a rectangular plate with geometric discontinuities has been discussed in the field of elastic stability. The rectangular plates have two simply supported opposite edges, while the other two plate edges can have free, simply supported, or clamped edges. The aforementioned buckling problem is solved by decomposing the plate into two subplates at the location where the geometric discontinuity uniaxial load acts. By applying the Levy method of the boundary conditions and the conditions along the geometric discontinuity, a system of equations has been derived. Based on the obtained solution, numerical analysis has been performed. Stability criteria (the buckling factor) in the function of plate thickness ratio, loads ratio and the position of the geometric discontinuity are obtained. The method gives exact stability criteria; samples of which are presented in a graphical form for plates with various boundary conditions. Some sample buckling results are served as benchmark solutions for researchers who are developing software for plate buckling analysis.

References

[1] Timoshenko P.S. and James G. M. (1961) *Theory of Elastic Stability*, McGraw-Hill, Book Company, Inc.
[2] Wittrick W. H. and Ellen C. H. (1962) Buckling of tapered rectangular plates in compression, *Aeronautical Quarterly* **13**, pp. 308-326..
[3] Malhorta S. K., Ganesan N. and Veluswami M. A. (1987) Vibrations of orthotropicsquare plates having variable thickness (parabolic variation), *Journal of Sound and* v*ibration* **119**, pp. 184-188..
[4] Olhoff N. (1974) Optimal design of vibrating rectangular plates, *International Journal of Solids and Structures* **10**, pp. 93-109.
[5] Guo S. J., Keane A. J. and Moshrefi-Torbati M. (1997) Vibration analysis of stepped thickness plates, *Journal of Sound and* v*ibration* **204**, pp. 645-657.
[6] Eisenberger M. and Alexandrov A. (2000) Stability analysis of stepped thickness plates, Computational Methods for Shell and Spatial Structures, *IASS-IACM* 2000 Athens, Greece: ISASR-NTUA.
[7] Ju F., Lee H. P. and Lee K. H. 1995 Free vibration of plates with stepped variations in thickness on non-homogeneous elastic foundations.*Journal of Sound and* v*ibration* 183, 533-545.
[8] Wang C. M., Chen Y. and Xiang Y. (2004) Stability criteria for rectangular plates subjected to intermediate and end inplane loads, *Thin-Walled Structures* **42,** pp. 119–136

VIBRATIONS AND NOISE AS DESIGN CONSTRAINTS IN MACHINE SYSTEMS DESIGN

M. Ognjanovic, M. Benur

Faculty of Mechanical Engineering,
The University of Belgrade, Kraljice Marije 16, 11120 Belgrade 35
e-mail: mognjanovic@mas.bg.ac.rs

Abstract. Vibrations of machine systems are important indicator of the system quality and of dynamic process which going on inside of the system. In reverse approach for design necessity, vibration indicators can be used as design limits (constraints) in order to choose and harmonized design parameters which can provide high level of technical system quality. As the case study, the robust design approach in the stage of the Embodiment design of power transmission components – gear systems is presented. For this purpose the specific model of gear vibrations is developed which is suitable for applying as the design constraint. The model is based on a great volume of experimental data about gear units vibrations and modal analysis, etc. Theoretical knowledge and models are insufficient yet to provide the necessary data. The article contains presentation of testing methods and data processing oriented to provide data necessary for the application in the suggested approach to power transmission components design. Additionally the article includes analysis of disturbance energy (power) absorption through the mechanical (elastic) structure, attenuation and emission in surroundings. The methodology of vibration and noise reduction is based on design parameters variation with objective to reduce disturbance energy and increase or kip at the same level of reliability and other service quality indicators.

Keywords: vibrations, gears, robust design

1. Introduction

Design for Vibration and Noise is one of separate approaches Design for X – DfX which in the design stage of Embodiment design provides environment for optimal design parameters definition in the first attempt. Robust design is a specific approach aimed to design parameters definition which can provide design solution insensitive at functional requirements variation [1-3]. This design advantages are provided by design constraints which are result of DfX methodology as well as reliability as design constraint, vibration as design constraint, noise as design constraint, cost as design constraint etc. This research presents by itself completing and spreadsheet of design methodology by incorporating the knowledge from various areas of techniques. In order to incorporate vibration and use as design constraint, it is necessary to identify the process of vibration generation in the certain technical system and then use this mechanism in reverse direction as design constraint. As the case study for this opportunity is chosen design parameters definition of the gear drive units. The gear systems present very specific assembly of mechanical components in the sense of vibration and noise generation. This is combination of discrete and continual dynamic system and interaction of design parameters have significant effect at vibration and noise indicators.

2. Vibration and Noise as Design Constraints

Vibration and noise of machine systems, i.e. power transmission components is the result of interaction between disturbances caused by components in motion and design parameters of components. This interaction in gear teeth meshes and bearings are in the form of machine parts collision, sliding, rolling etc [3-6]. In gear pair meshes between the meshed teeth all of these processes exist. A few kinds of teeth impacts arise in the mesh. More important is the addendum impact which is the result of gear pitch difference caused by elastic deformations.

2.1 Gear system restorable free vibrations

Teeth deformations are proportional to teeth load and teeth stiffness. Deformations replace the first point of contact from the right position A, to position A' which is ahead of point A. The contact of teeth pair starts with intensive addendum impact (Fig.1a). Collision speed v_c is proportional to teeth deformation, speed of rotation n and gear design parameters. By analyzing teeth geometry, deformations and speeds, collision speed at the first point of teeth contact is defined and presented in [7 and 8]. Every individual teeth impact produces natural free vibration of the gears (Fig 1b) with natural frequency f_n . By strong inside damping these vibrations attenuate in a short time. The next teeth pair entering the mesh collides again and again. Vibrations become restorable after every teeth impact. For relatively slow gear rotation the measured time function of restorable free vibrations is presented in Fig. 2a. The teeth mesh frequency f corresponds to gear revolutions and to gear teeth number. If the speed of the gear rotation is slow enough, the time between the two teeth impacts $1/f$ is higher than the time necessary for the free vibration attenuation.

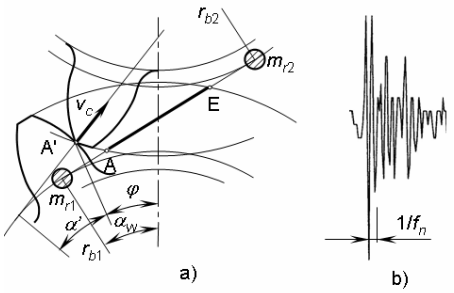

Figure 1. Gear teeth addendum collision (a) and free vibration caused by teeth impact (b)

As the speed of rotation increases the time between the two impacts gets lesser and lesser with the same natural frequency f_n. In the full resonance these two frequencies get equal $f=f_n$. For the case of gear vibration measurement (Fig 2b) (gear teeth number z=32) the resonant speed of gear rotation is 9860 rpm, and resonant teeth mesh frequency is 5258 Hz. Before the main resonance a few sub-resonances arise. This is the result of equality of additional disturbances and natural frequencies. After (behind) the main resonance arises, numerous super-critical resonances arise and total vibration level slightly increase. This is an interesting phenomenon, especially in the gear meshing process. In super-critical mesh

frequency range the absorbed disturbance energy by teeth impact relishes natural free vibrations. Higher speed of rotation produces higher level of absorbed disturbance energy and relished vibration energy has to be of higher level. Also, in super-critical mesh frequency range the modal structure of gear system fluctuates. In some parts of this range energy attenuation is lesser and relished energy by natural vibration is higher. By extensive measurement of gear vibrations with speed of rotation variation [7-8] and with frequency spectrum analysis these processes are identified.

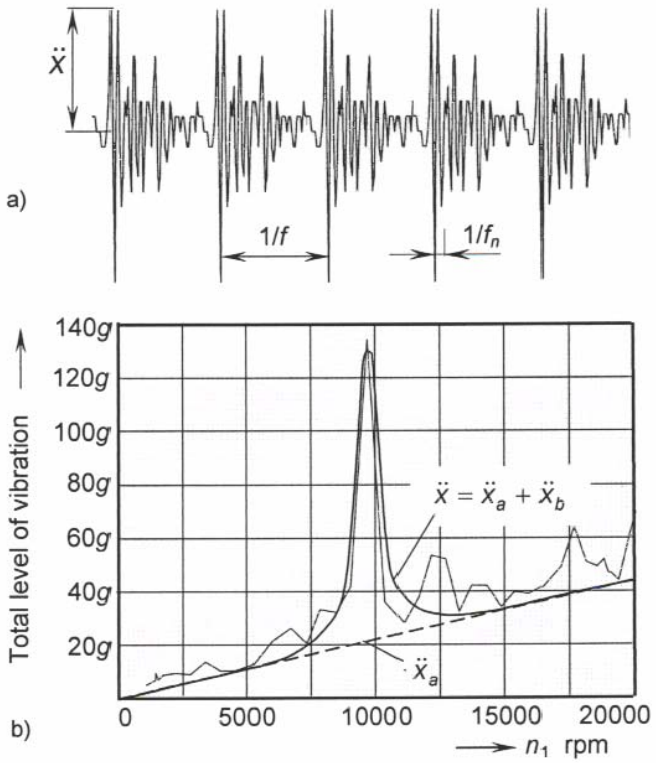

Figure 2. Restorable free vibration of gear pair:
a) the time function, b) result of vibration measurement and modeling

The results of those gear vibration measurement are presented in the form of calculation model [7-8]. The objective of modeling was to prove the hypothesis that gear vibration is a restorable natural one and then to present the vibrations in the form suitable for use as constraints in design parameters definition in gear drive design process. The total level of gear vibration $\ddot{x}$ is divided into two parts, continual $\ddot{x}_a$ and transient $\ddot{x}_b$ (Fig. 2b).

$$\ddot{x} = \ddot{x}_a + \ddot{x}_b = \ddot{x}_a\left(1 + \zeta_T \sin\varphi\right) = A\frac{c_\gamma x_0}{m_e} f \left(1 + \zeta_T \sin\varphi\right) \qquad (1)$$

The gear pair is modeled as a single mass oscillator, where m_e is equivalent mass reduced in collision direction (Fig.1a), c_γ is the mean gear teeth stiffness, x_0 is teeth deformation amplitude in the moment of teeth collision, ζ_T is transfer function between force transferred

to the gear masses and collision force F_c with phase angle φ, A – is coefficient of energy absorption inside the vibration system, and f is the gear teeth mesh frequency. The model presented by equation (1) and by the diagram in Fig.2b is developed using the theory of singular systems. According to this theory, the singular process consists of the two processes, continual and transient. Vibration energy emission is presented as the continual process (*a*) and transient (*b*) which contains resonances (the main, sub-critical and super-critical). Analytical model for continual part is established based on equilibrium between disturbance energy caused by teeth impacts and kinetic energy of restorable free vibrations. A significant part of disturbance energy is attenuated by numerous damping. The ratio between these energies is presented in the form of constant value which is calculated for measured vibrations level. The model for additional (transient) vibration values (*b*) is developed using analytical relations for resonance responses. These formulas include the difference between the teeth mesh (impact) frequency f and natural frequency f_n, dimensionless damping coefficient and phase angle. By variation of damping coefficient the response is calculated to be equal measured vibrations. In Fig.2b the calculated line which approximates the measured one is presented. This line contains the main resonance only. The program for these values calculation can also include sub-critical and super-critical resonances. The developed analytical model gives possibility to present disturbance energy transformation, and to explain the inside processes of gear teeth mesh. Besides, the model gives possibility for design parameters harmonization in order to avoid resonances and reduce gear vibration level, i.e. use gear vibration as design constraints.

2.2 The noise generation caused by gear system vibration

The part of disturbance energy absorbed by teeth repeatable collisions is relished in the form of kinetic energy of the gear system vibrations. The part of this kinetic energy is transformed, via free surfaces, into the noise energy inside the gear system housing. Another part of energy is transmitted through the supports (bearings) to the housing walls. This energy can be emitted from the wall surface in the surroundings in the form of noise waves. Also, the housing inside noise can penetrate through the housing walls into the surroundings. Much more important effect of the gear system vibration is disturbance of gear housing natural vibrations. This vibration can significantly intensify the noise that housing surfaces emit into the surroundings. From this point of view, the housing walls have a triple role: transmitter of vibration energy in surrounding, insulator of inside noise and generator of additional noise by own natural vibrations. Detailed analysis of the gear system housing behavior and its effects are presented in the articles [9-10]. Disturbing of a certain modal shape of elastic deformation with a certain natural frequency f_{ni} is the result of a few conditions, equality of natural and disturbing frequency, the same direction and type of elastic deformation of disturbance elastic waves and modal elastic deformations, low level of dimensionless damping coefficient of those modal elastic deformations (elastic waves). In Fig. 3a and b, numerical anaysis of natural frequencies by FEM, and by modal testing of chosen gearbox housing, is presented. Fig.3c shows response caused by modal hammer impact which contains the great collection of natural frequencies which are disturbed. Four of them f_{n1}… f_{n4} have dominant effect. If inside the housing the running gear system with mesh (teeth impact) frequencies f_1, f_2 and f_3 increase with speed of rotation, those frequencies proportionally increase. Equality of disturbance f_i and natural f_{ni} frequencies produces natural vibrations of housing walls and noise with this frequency.

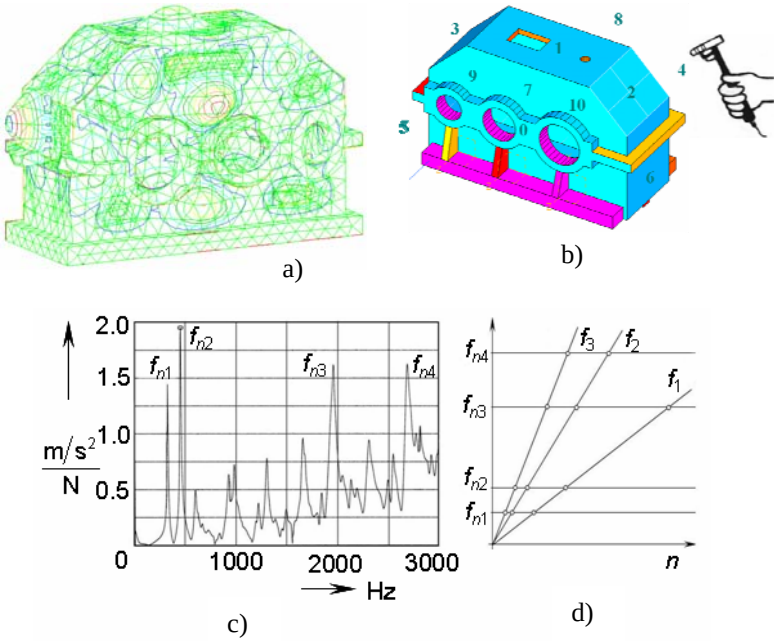

Figure 3. Relation between frequencies of gear system vibration and gear housing natural frequencies

The relation between disturbance and natural frequencies presented in Fig. 3d is a principle one and presents Campell's diagram for this purpose. A real gear system which is settled in the gearbox housing generates vibrations with a much more complex frequency spectrum. Except the presented teeth mesh frequencies f_1, f_2 and f_3 (Fig.3d) natural frequencies of the gear system dominate in those spectrums. Furthermore, gear system vibrations disturb natural vibrations of housing walls. However, all natural vibrations are independent of service conditions (speed of rotation) and are in close relation with design parameters. This is the reason why some of the gear system natural frequencies can permanently disturb some of the housing natural frequencies and produce permanent high level of noise with a certain frequency. It can be changed by some kind of design parameters variation.

2.3 Disturbance power transmission

Disturbance power transmits through the gear unit assembly and can be indicated by outside motion of discrete masses and by inside motion of elastic waves in machine parts [11]. Motion of discrete masses can indicate disturbance power transmission in the form of the next relations as follows.

$$W_c = \frac{K\, x_c}{2} f\ ; \qquad W_v = E_k f = \frac{m_e \dot{x}^2}{2} f\ ; \qquad \zeta_v = \frac{W_v}{W_c}; \qquad \zeta_s = \frac{W_s}{W_v} \tag{2}$$

The teeth collision power W_c is proportional to constant K proportional to teeth collision force (gear design parameters and collision speed) and fluctuation of teeth displacement x_c

and teeth mesh frequency *f*. The gear vibration power W_v is proportional to the rotating equivalent mass m_e, the vibration speed $\dot{x}$ (obtained via equat.1) and the teeth mesh frequency *f*. Disturbance power transfer function from collision power to vibration power is marked by ζ_v and transfer function from vibration power to the sound power is marked by ζ_s. All of them are experimental values which are in this way very simply presented.

The part of absorbed disturbance energy is transmitted through elastic structure of machine part in the form of elastic waves. By reflections from bound surfaces of machine part, the dominant value of that energy attenuates. In the course of attenuation process elastic waves reflect from bound surfaces. Via contact surfaces the part of wave energy is transmitted to the other machine part in the assembly. In Fig.4 the assemblies of the gear, shaft, bearing and support in housing wall are presented. The part of disturbance power absorbed in gear mesh W_g is transmitted to the shaft W_{sh} with the transmission factor $\zeta_{T(g-sh)} = W_{sh}/W_g$. The part of disturbance energy via other gear bound surfaces is transmitted into inside space of transmission unit in the form of inside sound power W_{in} with the transmission factor $\zeta_{T(in)} = W_{in}/W_g$. The rest of disturbance power W_g attenuates inside of the gear elastic structure i.e. attenuated power is $W_{ga}=W_g-W_{sh}-W_{in}$. Disturbance power transmitted to the shaft W_{sh} is partly transmitted via the bearings to the transmission unit housing W_{ho} and also partly to the inside of the housing in the form of inside noise W'_{in}. The rest also attenuates inside of the shaft elastic structure. The factor of disturbance power transmission from the shaft to the housing via the bearings is $\zeta_{T(b)} = W_{ho}/W_{sh}$. Disturbance energy transmitted to the housing W_{ho} can produce a few effects. The first one is further transmission to the outside and inside air in the form of outside noise W_{on} and in the form of inside noise W''_{in}. The second effect of the housing contains the possibility of the great attenuation of energy W_{ho} or possibility of disturbed natural vibrations and significant increase of W_{ho} and emitted noise W_{on} and W''_{in}. Also, disturbing natural (modal) vibrations of the housing modulate frequencies of emitted noise compared to frequencies of machine part vibrations (gears, bearings, shafts, etc). The third effect of housing is the inside noise isolation. Machine parts emit inside noise which is trying to pass through the housing walls into the surroundings. The noise transition ratio of the housing walls is $\zeta_{T(n)} = W'_{on}/\Sigma W_{in}$.

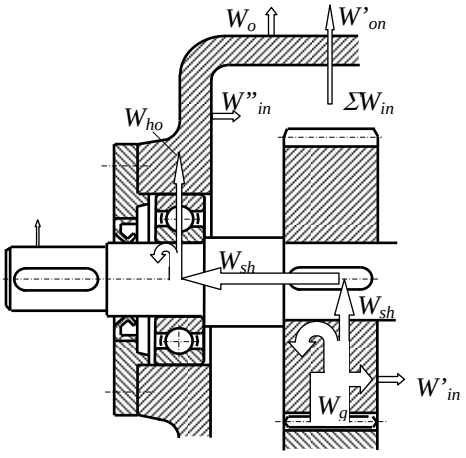

Figure 4. Disturbance energy transmission from the source to the surrounding

3. Design parameters definition constraint by vibration and noise

According to the main axiom of axiomatic approach in design, i.e. the axiom of independency, design parameters definition using reliability, vibration and noise as design constraints are independent. Usage of vibration and noise as design constraints provides the possibility to reduce vibration and noise level by variation of gear design parameters (gear teeth number z, gear module m, teeth offset factor x, teeth helical angle β etc without variation of d and b which are fixed by reliability as design constraint). The reduction of vibration and noise level with the aim to satisfy limited levels is the main task of vibration and noise design constraint. This constraint can be satisfied with a set of design actions and solutions [12-14]. It is not a general design solution which can provide this result. One group of these partial activities has the purpose to harmonize gear parameters in order to avoid equivalence between teeth mesh frequencies with natural frequencies of the gear pear and the housing. The second group of design actions is the gears parameters variation and the shape and dimensions variation of housing with the aim to reduce disturbance power, vibration power and noise power including the corresponding transfer functions (equat.2). The main of these activities oriented to satisfying the limited level of vibration and noise are as follows.

- By variation of gear teeth design parameters z, m, x, β (without variation of gear dimensions) the teeth stiffness and gear pair natural frequencies f_{ni} vary. Also, these variations effectuate the variation of gear teeth mesh frequency f. This is the way to avoid the equilibrium between disturbance and natural frequencies presented in Fig. 3d.
- By variation of gear teeth parameters z, m, x, β (without variation of gear dimensions) and by flank correction possibility is provided for the reduction of disturbances, especially teeth impacts in the gear pair mesh i.e. collision power W_c . It is the direct way to reduce vibration power W_v and sound power W_s (equ. and 2) and satisfy vibration and noise constraint.
- By variation of design parameters of gear system housing (shape, thickness of walls, distribution of ribs, material characteristics, etc.) gives possibility for harmonization of natural (modal) behavior of housing with natural frequencies and teeth mesh frequencies of gear system. This is the way to reduce the value of transfer function ζ_s (equat.1 and 2) as one step more in the noise reduction and satisfying of vibration and noise constraint.
- Isolation is a passive approach to satisfying the constraints by limited level of vibration and noise. The two groups of isolation principles are available. The first is oriented to interrupting the disturbance transmission through the system, i.e. from one to another machine part. For example, to interrupt disturbance transmission from the gear system to the housing via bearings (reduction of transmission factor ζ_s (equat.1 and 2). The second group is the coating of housing surfaces or the application of layered housing walls in order to increase the isolation properties and reduce emission activity of the housing walls, also with the aim to reduce ζ_s and additionally reduce the emitted noise and satisfy the noise constraint.
- Active approach to the noise reduction is also available and possible to apply when the passive solutions are insufficient. This approach implies the electronic control system which measures vibration or noise and produces the same vibrations or noise with the phase displacement which, in the sum, provides full elimination of vibration or noise.

4. Conclusions

The article offers an innovated design process of PT components, especially in the stage of embodiment design using vibration and noise as design constreints. The proposed design process based on robust and axiomatic approach is more effective and provides good solution in the first attempt insensitive to service conditions variation. Vibrations and noise of power transmission components are presented by specific and new models suitable to be the design constraints. Limited level of vibrations and noise have to be satisfied by variation of gear design parameters, bearing parameters and especially gearbox housing design parameters, without dimension variation which is already constrained by reliability. The analysis of vibration and noise generation is the wide area of experimental research, which provides a great support to robust design of PT components.

Acknowledgement

This article is a contribution to the Ministry of Education and Science of Serbia funded project TR 035006.

References

[1] Armen Z, James K, Lusine B (2007) Modeling and analysis of system robustness, *Journal of Engineering Design* **18**, pp 243-263.
[2] Mizuyama H (2005) Statistical robust design of complex system through a sequential approach, *Journal of Engineering Design* **16**, pp 259-276.
[3] Lacey D, Steele C (2006) The use of dimensional analysis to augment design of experiments for optimization and robustification, *Journal of Engineering Design* **17**, pp 55-73
[4] Verdmar L, Andersson A (2003) A method to determine dynamic loads on spur gear teeth and on bearings, *Journal of Sound and Vibration* **267**, pp 1065-1084.
[5] Kim T C, Rook T E, Singh R (2005) Effect of nonlinear impact damping on the frequency response of a torsion system with clearance, *Journal of Sound and Vibration* **281**, pp 995-1021.
[6] He S, Gunda R, Singh R (2007) Inclusion of sliding friction in contact dynamics model for helical gears, *ASME Journal of Mechanical Design* **129**, pp 48-57.
[7] Agemi F, Ognjanovic M (2004) Gear Vibration in Supercritical Mesh-Frequency Range, *FME Transactions* **32**, pp 87-94.
[8] Ognjanovic M, Agemi F (2010) Gear vibrations in supercritical mesh-frequency range caused by teeth impacts, *Strojniski vestnik – Journal of Mechanical Engineering* **56**, pp 653-662
[9] Ciric-Kostic S, Ognjanovic M (2006) Excitation of the Modal Vibrations in Gear Housing Walls, *FME Transactions* **34**, pp 21-28.
[10] Ciric-Kostic S, Ognjanovic M (2007) The Noise of Gear Transmission Units and the Role of Gearbox Walls, *FME Transactions* **35**, pp 105-112.
[11] Pavic G (2005) The role of damping on energy and power in vibrating systems, *Journal of Sound and Vibration* 281, pp 45-71.
[12] Imrek H (2009) Width modification for gears with low contact ratio, *Meccanica* **44**, pp 613-621.
[13] Dron J.P, Rasolofondraible L, Chlementin X, Bolaers F (2010) A Comparative experimental study on the use of three denoising methods for Bearing Defects detection, *Meccanica* **45**, pp 265-277.
[14] Ognjanovic M, Benur M (2011) Experimental research for robust design of power transmission components, *Meccanica*, DOI 10.1007/s11012-010-9331-y

AN ENGINEERING APPROACH TO WELDING SIMULATION USING SIMPLIFIED MATERIAL PROPERTIES

M. Perić[1], D. Stamenković[2]

[1] Bureau of Energetics and Mechanical Engineering Ltd.,
Petrovaradinska 7, 10000 Zagreb, Croatia
e-mail: mato.peric@bestprojekt.hr
[2] Termoelektro Ltd. Uralska 9, Belgrade, 11060, Serbia
e-mail: dragi33@gmail.com

Abstract. The article is about conducting a numerical simulation of a welding process on butt-weld of two pipes. There were two models considered: model A in which thermal and mechanical properties of materials were temperature dependent and model B in which thermal and mechanical properties were taken at room temperature except yield strength. A parallel numerical simulation of welding process was cunducted, using the software packages Abaqus and Ansys. The obtained results of residual stresses for models A and B agree very good.

1. Introduction

Welded joints are inevitable, but at the same time a very reliable technique of joining materials in almost all areas of technology. The parts of structures near the welding zone are exposed to high localized heating and subsequent rapid cooling. It causes plastic deformations and a manifestation of residual stress in the weld. These manifestations are harmful, but inevitable, so that a reliable calculation of residual stress and deformations is very important for achieving the safety design.

With the development of information technology and the application of the finite element method the numerous numerical simulations of the welding process have been performed and a lot of knowledge has also been established [1-9]. It has also been established that the amount of the residual stress is primarily affected by a heat input, material properies, thermal and mechanical boundary conditions, a number of weld pass and structural dimensions.

For a detailed numerical simulation of a welding process it is a necessity to know thermal and mechanical properties depending on temperature. However, for many materials the thermal and mechanical properties are non-existent or hardly available on high temperatures.

Using the structure of two welded plates made of aluminium alloy 5052-H32, Zhu [1] carried out a detailed research of the impact of individual thermal and mechanical

properties on residual stress. Thus he established that along with little mistakes all thermal and mechanical properties can be taken at room temperature except the yield strength which should be temperature dependent.

In this work a parallel numerical simulation of welding process of two steel tubes was conducted using Abaqus code [10] and Ansys code [11] for two models: model A in which thermal and mechanical properties of materials were used, and model B in which mechanical and thermal properties were used at room temperature except yield strength, which is taken depending on temperature.

2. Computional Approach

The simulations performed in this work use sequential thermal-stress solution procedure in which the transient heat transfer analysis is followed by the thermal stress analysis. Temperatures predicted by the heat transfer analysis are used as the loading for thermal stress analysis.

2.1. Thermal model

Differential equation of heat conduction in solid bodies can be expressed by a formula:

$$\frac{\partial}{\partial x}\left(k_x \frac{\partial T}{\partial x}\right)+\frac{\partial}{\partial y}\left(k_y \frac{\partial T}{\partial y}\right)+\frac{\partial}{\partial z}\left(k_z \frac{\partial T}{\partial z}\right)+Q=\rho C \frac{\partial T}{\partial t} \tag{1}$$

where k_x, $k_{y,}$ k_z are thermal conductivity in the x, y and z respectively, T is the current temperature, Q is the heat generation, ρ is the density, C is the specific heat capacity and t is the time. The general solution is obtained by applying the following initial and boundary conditions:

Initial condition:

$$T(x,y,z,0)=T_0(x,y,z) \tag{2}$$

Boundary conditions:

$$\left(k_{\mathrm{x}} \frac{\partial T}{\partial x} N_x + k_y \frac{\partial T}{\partial y} N_y + k_z \frac{\partial T}{\partial z}\right) + q_s + h_c(T-T_\infty) + h_{\mathrm{r}}(T-T_{\mathrm{r}}) = 0 \tag{3}$$

where N_{x}, N_y, N_z are the direction cosine normal to the boundary, h_c, h_{r} are the convection and radiation heat transfer coefficients respectively, q_s is the boundary heat flux and T_{r} is the temperature of radiation heat source and T_∞ are the surrounding

temperature. Radiation heat losses are dominant near the weld, so they can be expressed by a formula:

$$h_{\mathrm{r}} = \sigma\varepsilon F(T^2 + T_{\mathrm{r}}^2)(T + T_{\mathrm{r}}) \tag{4}$$

where $\sigma = 5.67 \times 10^{-8}$ J/(m^{2}K^4) is the Steffan-Boltzman constant, ε is the effective emissivity and F is the configuration factor. Starting from the welding zone a share of radiation heat losses decreases and a share of convection heat loses h_c rises. A total heat input is expressed by:

$$q = \frac{\eta UI}{V_H} \tag{5}$$

Where η is the arc efficiency, I is current, U is voltage a V_H is the weld volume.

2.2. Mechanical model

Equilibrium equations are expressed by formulas:

$$\sigma_{ij,j} + \rho b_i = 0 \tag{6}$$

$$\sigma_{ij} = \sigma_{ji} \tag{7}$$

In equations (6) i (7) σ_{ij} is the stress tensor, ρ is the material density a b_i is the body force. Following thermal-plastic constitutive equations are used in numerical simulations:

$$[d\sigma] = [D^{ep}][d\varepsilon] - [C^{th}]dT \tag{8}$$

$$[d\sigma] = [D^{ep}][d\varepsilon] - [C^{th}]dT \tag{9}$$

where $[D^e]$ is the elastic stiffness matrix, $[D^p]$ is the plastic stiffnes matrix, C^{th} is the thermal stiffness matrix, $[d\varepsilon]$ is the strain increment and dT is the temperature increment.

3. Welding conditions, boundary conditions and material properies

Figure 1 shows computational model of butt weld of two pipes made of SAE 1020 steel. The diameter of each pipe is 324 mm, wall thickness is 3.96 mm and length of each pipe is 200 mm. Constant weld width is presumed to be 3.84 mm along the whole wall thickness. Mechanical and thermal properties are given in Table 1. The material is modelled as an elastic – ideally plastic. Welding parameters chosen for this analysis are as follows:

tungsten inert gas welding, welding current *I=110* A, welding voltage *U=20* V and welding speed *v*=5 mm/s. The following values are assumed: the convective heat transfer h_c=15 W/m^{2}K, the arc efficiency η =70% and the emissivity ε= 0.8. Welding of pipes is modelled in single pass. Heat flux applied by welding is $q = 2.076 \times 10^{10}$ J/m^{3}s. Three-dimensional mesh consisted of 14400 elements. The same mesh is used both for thermal and mechanical analysis. Two numerical simulations of welding process were carried out; model A using thermal and mechanical properties, which are temperature dependent, and model B using thermal and mechanical properties at room temperature; except yield strength, which is taken depending on temperature.

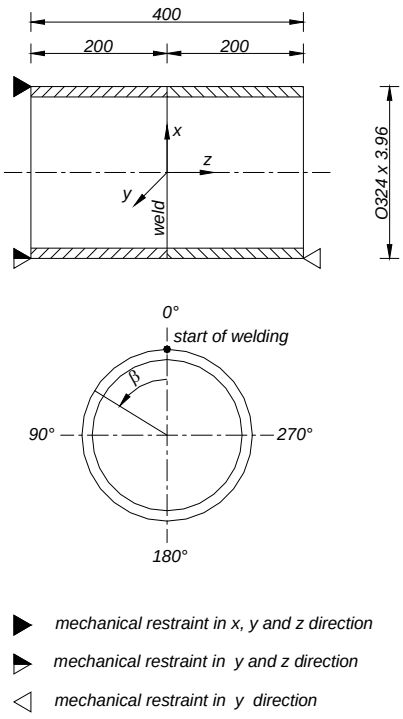

Figure 1. Geometry of butt-welded pipes

Table 1: Thermal and mechanical properties of steel SAE 1020 [2]

Temperature (°C)	**Specific heat (J/Kg°C)**	**Conductivity (W/m°C)**	**Density (kg/m^3)**	**Yield stress (MPa)**	**Thermal expansion coefficient (°C^{-1})**	**Young's modulus (GPa)**	**Poisson's ratio**
0.00	360.0	59.0	7800	105.0	1.100E-5	210.00	0.280
200	650.0	52.5	7792	101.0	1.250E-5	165.00	0.295
400	900.0	43.0	7784	101.0	1.400E-5	115.00	0.300
500	1050.0	37.5	7780	99.0	1.500E-5	85.00	0.305
600	1150.0	35.0	7776	20.0	1.550E-5	45.00	0.310
700	1250.0	32.0	7772	20.0	1.600E-5	20.00	0.310
800	1300.0	31.0	7768	20.0	1.620E-5	20.00	0.310
1000	1300.0	31.0	7760	20.0	1.620E-5	20.00	0.310
1200	1300.0	31.0	7752	20.0	1.620E-5	20.00	0.310
1400	1300.0	31.0	7744	20.0	1.620E-5	20.00	0.310
1600	1300.0	31.0	7736	20.0	1.620E-5	20.00	0.310

4. Results

In Figures 2 and 3 are shown temperature profiles at time100 seconds after start of welding with a central angle β =180°, for models A i B.

Figures 4 and 5 show residual stress fields σ_z in z direction, along the pipe axis on the outer surface of the tube.

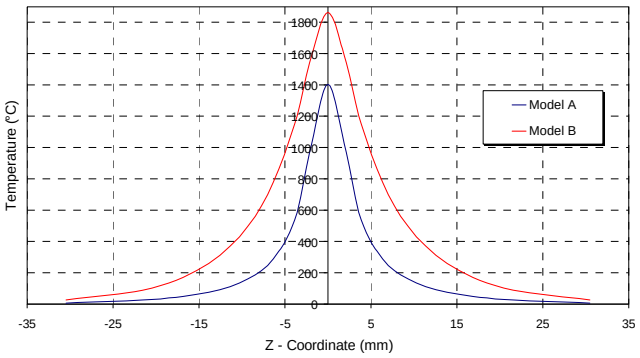

Figure 2. Temperature profiles t = 100 s and β =180°, Abaqus

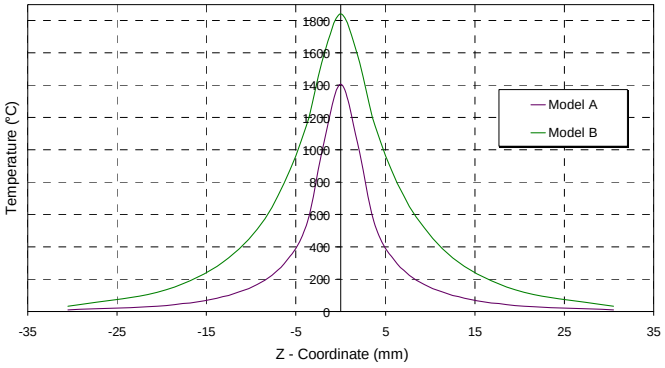

Figure 3. Temperature profiles t = 100 s and β =180°, Ansys

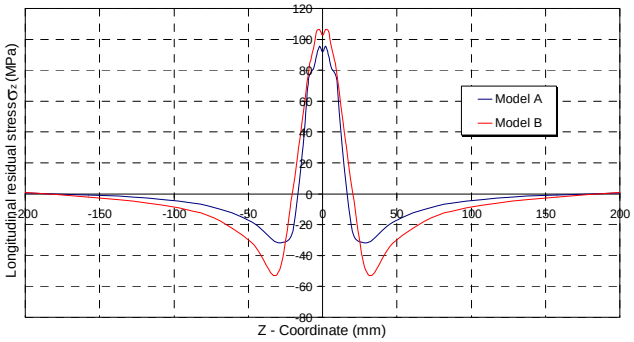

Figure 4. Residual stresses σ_z in z direction along inner surface for β =180°, model A and model B, Abaqus

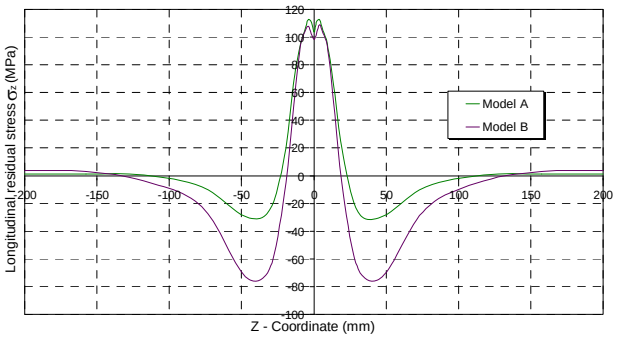

Figure 5. Residual stresses σ_z in z direction along inner surface

for β =180°, model A and model B, Ansys

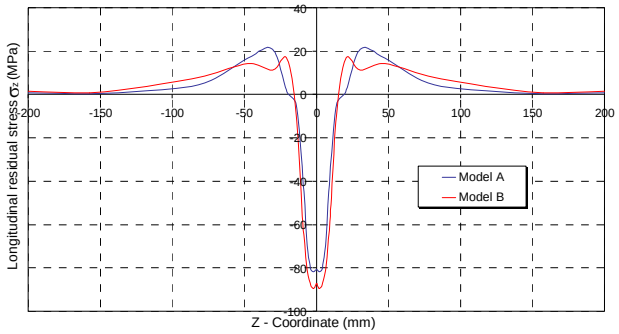

Figure 6. Residual stresses σ_z in z along outer surface for β =180°, Model A and Model B, Abaqus

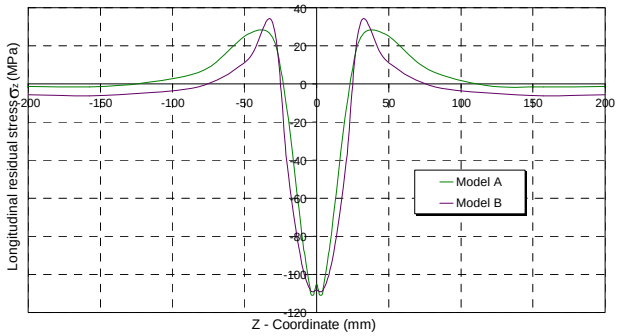

Figure 7. Residual stresses σ_z in z along outer surface for za β =180°, Model A and Model B, Ansys

5. Conclusion and discussion

Based on carried out numerical simulations of welding process for models with temperature dependent thermal properties, model A, and and for models with independent thermal and mechanical properties, model B, except yield strength, which is taken depending on temperature, we can conclude the following:

Temperature fields for the case of numerical simulation of welding process of two steel tubes SAE 1020 in the welding zone, for models A and B, show significant discrepancies (Figures 2 and 3), which was confirmed with the parallel analysis in Abaqus and Ansys.

Residual stresses σ_z in direction of pipe axis, calculated along inner surface, are well matched at models A and B, (Figures 4 and 5). Considerable difference among residual stresses σ_z appear along outer surface (Figures 6 and 7), which was confirmed with the parallel analysis in Abaqus and Ansys as well.

According to the obtained values of residual stresses, we can conclude that the numerical simulation of the welding process is, using thermal and mechanical properties of steel materials at room temperature, except for yield strength which must be taken depending on the temperature, acceptable for a wide range of industries where less accuracy in the results of residual stresses and strain are required. In order to achieve more accurate residual stresses and strain, it is needed to know the thermal properties of materials at high temperatures.

References

[1] Zhu XK, Chao YJ (2002), Effects of temperature-dependent material properties on welding simulation, *Computers and Structures*, **80**, pp. 967-976.
[2] Teng TL, Chang PH. (1998) ,Three-dimensional thermomechanical analysis of circumferentiallly welded thin-waled pipes, *International Journal of Pressure Vessels and Piping*, **75**, pp. 237-247.
[3] Deng D, (2009), FEM prediction of welding residual stress and distortion in carbon steel considering phase transformation effects. *Materials and Design*, **30**, pp. 359-366.
[4] Deng D, Liang W, Murakawa H. (2007), Determination of welding deformation in fillet –welded joint by menas of numerical simulation and comparison with experimental measurements, *Journal of Materials Processing Technology*, **183**, pp. 219-225.
[5] Deng D, Murakawa H., Liang W. (2007), Numerical simulation of welding distortion in large structures. *Computer methods in applied mechanics and engineering*, **196**, pp. 4613-4627.
[6] Lee CH, Chang KH, (2008), Three-dimensional finite element simulation of residual stresses in circumferential welds of steel pipe diameter effects, *Material Science and Engineering*, **487**, pp. 210-218.
[7] Peric M., Tonkovic Z., Karsaj I, (2010), Numerical analysis of residual stresses using a shell/3D modeling technique, *Proceedings of the International Conference on Advances in Welding Science and Technology for Construction, Energy and Transportation AWST-2010*, pp.75-80
[8] Stamenkovic D., Vasovic I.: Finite Element Analysis of Residual Stresses in Butt Welding Two Similar Plates, *Scientific Technical Review*, ISSN 1820-0206, 2009,Vol. LIX, No.1, pp.57-60.
[9] Peric M., Stamenkovic D., Milkovic V.: Comparison of residual stresses in butt-welded plates using software packages abaqus and ansys, *Scientific Technical Review*, ISSN 1820-0206, 2010,Vol.60,No.3-4, pp.22-26
[10] ABAQUS/Standard, User's guide and theoretical manual, Version 6.8, Hibbit, Karlsson & Serensen, Inc. (2008).
[11] Theory Reference for ANSYS and ANSYS Workbench, ANSYS Inc. Release 12.1